Phonon spectra and temperature variation of thermodynamic properties of fcc metals via Finnis-Sinclair type many body potentials: Sutton-Chen and improved Sutton-Chen models

by

Aistis Januszko

B. Sc. (Honours Physics) Department of Physics and Astronomy,

University of Waterloo, Canada

A THESIS SUBMITTED IN PARTIAL FULFILMENT OF

THE REQUIREMENTS FOR THE DEGREE OF

MASTER OF SCIENCE

in

The Faculty of Mathematics and Sciences

Department of Physics

BROCK UNIVERSITY

May 5, 2014

In presenting this thesis in partial fulfillment of the requirements for advanced degree at Brock University, I agree that the Library shall make it freely available for reference and study. I further agree that permission for extensive copying of this thesis for scholarly purposes may be granted by the head of my department or by his or her representatives. It is understood that copying or publication of this thesis for financial gain shall not be allowed without my written permission.

Signature: _____

Department of Physics
Brock University
500 Glenridge Avenue
St. Catharines, Ontario
Canada, L2S 3A1

Date: _____

Abstract

Volume(density)-independent pair-potentials cannot describe metallic cohesion adequately as the presence of the free electron gas renders the total energy strongly dependent on the electron density. The embedded atom method (EAM) addresses this issue by replacing part of the total energy with an explicitly density-dependent term called the embedding function. Finnis and Sinclair proposed a model where the embedding function is taken to be proportional to the square root of the electron density. Models of this type are known as Finnis-Sinclair many body potentials.

In this work we study a particular parametrization of the Finnis-Sinclair type potential, called the "Sutton-Chen" model, and a later version, called the "Quantum Sutton-Chen" model, to study the phonon spectra and the temperature variation thermodynamic properties of fcc metals. Both models give poor results for thermal expansion, which can be traced to rapid softening of transverse phonon frequencies with increasing lattice parameter. We identify the power law decay of the electron density with distance assumed by the model as the main cause of this behaviour and show that an exponentially decaying form of charge density improves the results significantly. Results for Sutton-Chen and our improved version of Sutton-Chen models are compared for four fcc metals: Cu, Ag, Au and Pt. The calculated properties are the phonon spectra, thermal expansion coefficient, isobaric heat capacity, adiabatic and isothermal bulk moduli, atomic root-mean-square displacement and Grüneisen parameter. For the sake of comparison we have also considered two other models where the distance-dependence of the charge density is an exponential multiplied by polynomials. None of these models exhibits the instability against thermal expansion (premature melting) as shown by the Sutton-Chen model.

We also present results obtained via pure pair potential models, in order to identify advantages and disadvantages of methods used to obtain the parameters of these potentials.

Acknowledgements

I would like to thank the Brock University Physics Department for giving me the opportunity to study in such a fulfilling environment. Many thanks to the faculty and staff as well as to friends and colleagues. Most of all I must thank Dr. Bose for his support and patience throughout this process and for his ever-present willingness to answer questions and impart knowledge to those who seek it.

Contents

List of Tables

List of Figures

Chapter 1

Introduction

Pair potentials have been used to study a wide range of properties of metals including bulk, surface and atomic cluster properties. Their computational simplicity and tractability make them well suited to atomistic level computer simulations as well. The general form of such a potential is a sum of two pairwise terms, one repulsive and the other attractive. Many different potentials of this form have been proposed and studied for various metals. This work can be divided into two parts: the first analyzes two pair-potentials in their ability to reproduce various thermodynamic properties of noble metals Cu, Ag and Au.

Going beyond the simple pair-potentials requires the inclusion of many-body interactions. The Sutton and Chen [18] potential is an example of this that was developed through the Embedded-Atom Method (EAM). The second part of this work will look at this and its updated version, the Quantum Sutton-Chen potential, in detail. The EAM represents each atom as being embedded in a host electron density that is the sum of all neighbouring charge densities. This form of potential offers a solution to the major limitations of pair potentials that will be discussed in the next section while retaining much of the mathematical simplicity. Since these EAM potentials have a repulsive branch that is of the same form as that in a pair potential, it is useful to

have some understanding of how different forms of this term affects results. This was the motivation for first studying pair-potentials.

The Sutton-Chen and Quantum Sutton-Chen potentials have been analyzed in various applications. For instance, Liem and Chan have used the Sutton-Chen potential to study adsorption of platinum on graphite walls [19]; Kimura *et al.* have applied their Quantum Sutton-Chen model to predict viscosity in Au-Cu alloys [20] as well as glass formation and crystallization in Cu-Ag and Cu-Ni alloys [21]; Caixing *et al.* have studied the rapid solidification of $Cu_{70}Ni_{30}$ using the Sutton-Chen model in molecular dynamics (MD) simulations [22]; Akbarzadeh *et al.* applied the Quantum Sutton-Chen model to calculate the surface energy of platinum nanoparticles via MD simulations [23].

There are many models other than the Sutton-Chen; Ryu *et al.* have taken another modified EAM potential and altered it to improve results for the melting point and latent heat predictions of Au and Si [24]. Metal alloying was studied by Groh *et al.* using another modified EAM potential by combining the potentials of pure elements [25]. Lee *et al.* have analyzed some methods of simulating material systems using a modified EAM potential [26].

This work is the first exhaustive study of the thermodynamic properties as predicted by the Sutton-Chen type potentials over a wide temperature range. In the original Sutton-Chen potential, both the attractive and repulsive contributions have a power-law form while the modified version has an exponential decay as the attractive part. This choice was motivated by results of charge density decay from Density Functional Theory and Hartree-Fock calculations [17, 27]. Also, in the case of the Sutton-Chen potential, the thermal expansion coefficient is greatly overestimated for Cu, Ag, Au and Pt. While the quantum version fares better in most cases, the results are still unsatisfactory. Because of this, a modified Sutton-Chen potential is developed to attempt to improve results while changing the form of the potential as

little as possible. Significant improvement is seen in nearly all the properties studied: phonon spectra, thermal expansion coefficient, adiabatic and isothermal bulk modulus and isobaric heat capacity. Two other potentials by Cleri & Rosato [28] and Dai *et al.* [29] that have an exponential form are included for comparison.

1.1 Pair Potentials

Simple pair potentials are fundamentally limited in some respects. A central-force pair potential will always predict elastic constants $C_{12} = C_{44}$ for cubic systems [12, 39]. The energy required to move an atom from the bulk of a crystal to the surface is known as the vacancy formation energy; the energy to move an atom from the surface to infinity is the cohesive (also sublimation) energy. Pure pair-potentials will always predict these two energies to be equal. In reality the vacancy formation energy is approximately 1/4 to 1/3 the cohesive energy [30]. Pair potentials also lack any environmental dependence (no distinction between surface and bulk atom bond strength is possible) and as such are not suitable for calculating properties of defects and surface interactions. Some attempts have been made to overcome these limitations such as including a volume-dependent term along with the potential energy function [31]. This improves the results of pair potentials to an extent by correctly reproducing the elastic constant relations and some other properties. However, these potentials are still not suitable for studies of surfaces and interfaces since the volume of the sample at these areas is unclear. Further, still not included is any angular dependence of the bonds and there is no fundamental theoretical backing for adding such volume-dependent terms.

The two pair potentials studied in this work are the Morse [2] and the Erkoç [3] potential, both of which are empirical. They are applied to Cu, Ag and Au in order to determine if either parametrization scheme yields consistently better results.

Morse Potential

The Morse 3-parameter potential has the form

$$U(r) = D(e^{-2\alpha(r-r_0)} - 2e^{-\alpha(r-r_0)}) \tag{1.1.1}$$

where D, α and r_0 are adjustable parameters. It has been used to study the formation energy of point and line defects [2]. This potential has been parametrized for metallic systems truncated at distances ranging from nearest to twelfth-nearest neighbours. The parameters were determined by fitting the potential to the sublimation energy at zero temperature, the equilibrium lattice parameter and the compressibility at zero temperature and pressure. A second set of parameters for Cu and Au was derived by setting the total energy equal to the vacancy formation energy rather than the sublimation energy. The motivation for this parametrization scheme was an overestimation of the vacancy formation energy calculated from the initial parameter set. While these two values should be equal in theory for a pair-potential, experimental values differ leading to unique values for the parameters. Parameters for the first, sixth and 12th-nearest neighbour potential are given in Table 1.1.

Erkoç Potential

The Erkoc potential contains eight parameters and has the form [3]:

$$U(r) = \frac{D_{21}A_1e^{-\alpha_1 r^2}}{r^{\lambda_1}} + \frac{D_{22}A_2e^{-\alpha_2 r^2}}{r^{\lambda_2}} \tag{1.1.2}$$

It is formed from pair interactions by fitting the pair potential function to the experimentally determined curve of a metallic dimer [32]. Six of the eight parameters are fit to this curve while the remaining two (D_{21} and D_{22}) are used as scaling parameters determined by fitting the potential to the equilibrium lattice parameter and bulk cohesive energy. While the pairs of parameters D_{2x} and A_x could be combined into a single constant each, having them written separately highlights the fitting process.

Table 1.1: Parameters for the Morse potential. The letters in parentheses beside the element name indicate whether cohesive (coh) or vacancy (vac) formation energy was used in the fitting. The numbers within these parentheses indicate the number of neighbor shells used in the calculation of the parameters. For Ag, only one parameter set was available which was taken from [1]. The remaining parameters are from Cotterill and Doyama [2] based on cohesive energy, lattice parameter and bulk modulus.

Metal	D (eV)	α (Å^{-1})	r_0 (Å)
Cu (coh,1)	0.58922	1.35438	2.54756
Cu (coh,6)	0.32688	1.27234	2.89360
Cu (coh,12)	0.32365	1.29415	2.91331
Cu (vac,1)	0.19500	2.342508	2.547564
Cu (vac,6)	0.170073	2.321248	2.592091
Cu (vac,12)	0.170002	2.321628	2.592351
Au (coh,1)	0.603392	1.481405	2.874127
Au (coh,6)	0.420915	1.439041	3.065135
Au (coh,12)	0.418841	1.444322	3.071131
Au (vac,1)	0.163333	2.847319	2.874127
Au (vac,6)	0.156342	2.839503	2.885484
Au (vac,12)	0.156340	2.839513	2.885490
Ag (coh,12)	0.3294	1.3939	3.096

Table 1.2: Parameters for the Erkoç potential. This potential was first fit to the experimentally determined curve of each elemental dimer. The terms in the potential were then scaled by fitting to equilibrium lattice parameter and cohesive energy for a lattice sum up to eight neighbour shells. Parameters taken from [3] and [1].

Parameter	Cu	Au	Ag
D_{21}	0.436092895	0.888911352	1.00610152
A_1 (eV)	110.766008	345.923364	220.262366
λ_1	2.09045946	1.04289230	1.72376253
α_1 (Å^{-2})	0.394142248	0.750775965	0.673011507
D_{22}	0.245082238	0.254280292	0.221234242
A_2 (eV)	-46.1649783	-38.9245908	-26.0811795
λ_2	1.49853083	1.05974062	1.81484791
α_2 (Å^{-2})	0.207225507	0.229377368	0.120620395

The parameters are given in Table 1.2. This potential was used to study structural stability and energetics of 3 to 7 atom micro-clusters [3] as well as calculate the elastic constants and bulk moduli of several elements. It is interesting to compare the success of these two potentials with regards to bulk properties given that the Morse potential was fit to such properties whereas the Erkoç potential was not.

1.2 Embedded Atom Method

The embedded atom method was first introduced my Daw and Baskes [33] and is one attempt to overcome some of the limitations of pair potentials in the description of metals. The general form of the total energy of a monatomic crystal is

$$U_{tot} = \epsilon \left[\frac{1}{2} \sum_{i,j \neq i} V(r_{ij}) + \sum_{i} F(\rho_i) \right] \tag{1.2.1}$$

where $V(r)$ is a pairwise repulsive term accounting for the core-core and Pauli repulsive forces and $F(\rho)$ is a many-body attractive term that can generally be expressed as a sum:

$$\rho_i = \sum_{j \neq i} \phi(r_{ij}) \tag{1.2.2}$$

$F(\rho)$ may be interpreted in several ways: in the original work by Daw and Baskes [33] it represents the energy required to embed an atom into a host electron density $\rho(r)$. This local density is formed from a rigid superposition of the neighbouring atomic charge densities which are assumed to be spherically symmetric. In this way it captures the many-body effects that are lacking in pair potentials. An alternate interpretation of this term (from the view of tight-binding theory) is that it represents the total band energy—a sum of "hopping" integrals in the case of transition metal d-band electrons [4]. Mathematically, however, the two views are equivalent and provide a straightforward way to include the electronic contribution to metallic bonding without going through an entire band structure calculation.

There are several different functional forms of $F(\rho)$, each with various points of justification. Mei and Davenport, for example, used the following form [34]

$$\begin{aligned} F(\rho) = & - E_c \left[1 - \frac{\alpha}{\beta} \ln\left[\frac{\rho}{\rho_e}\right]\right] \left[\frac{\rho}{\rho_e}\right]^{\alpha/\beta} \\ & + \frac{1}{2}\phi_e \sum_x s_x e^{-(p_x-1)\gamma} \\ & \times \left[1 + (p_x - 1)\delta - p_x \frac{\delta}{\beta} \ln\left[\frac{\rho}{\rho_e}\right]\right] \left[\frac{\rho}{\rho_e}\right]^{p_x \frac{\gamma}{\beta}} \end{aligned} \tag{1.2.3}$$

with $\alpha = (9B_e\Omega_e/E_c)^{1/2}$ (where B_e is the equilibrium bulk modulus, Ω_e is the atomic volume and E_c is the cohesive energy), β, γ, δ, ρ_e and ϕ_e being parameters, s_x being the number of atoms in neighbour shell x and $p_x = \sqrt{x}$. This choice for the density function was motivated by the fact that for most metals the total energy per atom is well represented by [35]

$$E(r_1) = -E_c \left[1 + \alpha(r_1/r_{1e} - 1)\right] e^{-\alpha(r_1/r_{1e}-1)} \tag{1.2.4}$$

where r_1 is the nearest-neighbour distance (r_{1e} at equilibrium), E_c is the cohesive energy and α is given above. Subtracting from this a suitable repulsive two-body term (in this case, one of similar form to Eq. (1.2.4)) yields the basis for finding

$F(\rho)$. The total density was assumed to be exponential: $\rho = \rho_e \exp[-\beta(r_1/r_{1e} - 1)]$ [34]. This form is only analytic for nearest-neighbour interactions, however, and must be replaced with a parametrized function to extend the interaction to further atoms. Following this procedure results in the density function $F(\rho)$ given by Eq. (1.2.3). Since the scaled binding energy of many metals falls on the same curve, only values for cohesive energy, bulk modulus and lattice parameter at equilibrium density are required in order to determine the energy-density relation over the whole range of densities [35].

Another form of $F(\rho)$ used by Baskes [36] to model covalent bonding in silicon is

$$F(\rho) = -E_0 \left(\frac{\rho}{\rho_e}\right) \ln\left(\frac{\rho}{\rho_e}\right) \tag{1.2.5}$$

E_0 being the cohesive energy and ρ_e is the equilibium electron density. The justification for this comes from the fact that the change in first-neighbour distance for silicon is approximately proportional to the logarithm of the change in the number of neighbours [36]. That is, $r - r_0 = \beta \ln(n/n_1)$ with r_0 being the nearest-neighbour distance, β a constant and n/n_1 the ratio of the number of nearest neighbours to that of the reference structure (diamond silicon). There is not, however, any theoretical backing for choosing this function.

From the results of tight-binding theory comes another density function that is a simple square-root function [4]:

$$F(\rho_i) = -c\sqrt{\rho_i} \tag{1.2.6}$$

This is a result that comes from the second-moment approximation of the local density of states in transition metals [35] where the second moment of the density of states is

$$\mu_2 = \int_{-\infty}^{\infty} E^2 D(E) dE \tag{1.2.7}$$

$D(E)$ is the density of states at energy E. This approximation is based on the

Table 1.3: Parameters for the Sutton-Chen potential. Cohesive energy and lattice parameter were fit exactly while m and n were restricted to integers that best reproduced the bulk modulus and elastic constants. Values taken from [4]

Metal	m	n	ϵ (eV)	c	a (Å)
Cu	6	9	1.2382×10^{-2}	39.432	3.6100
Ag	6	12	2.5415×10^{-3}	144.41	4.0900
Au	8	10	1.2793×10^{-2}	34.408	4.0800
Pt	8	10	1.9833×10^{-2}	34.408	3.9200

Friedel model [30] which assumes that the metallic bonding in transition metals is dominated by the d-electrons. The density of states of these electrons is then assumed to be rectangular with a width W and height of $5/W$, so that the total number of states is 5 per atom (corresponding to the 5 unique d-orbitals). The root-mean-square bandwidth can be shown to be proportional to the square-root of the second moment of the density of states [37]. Limiting the interaction to nearest-neighbours and assuming all the orbitals are identical yields a bond energy that is proportional to the second moment of the density of states. This has the consequence that the energy *per bond* decreases as the coordination number increases [38]:

$$\frac{E_{bond}}{z} = \frac{c\sqrt{\rho}}{z} = \frac{\xi\sqrt{z}}{z} = \frac{\xi}{\sqrt{z}} \tag{1.2.8}$$

using z as the coordination number and ξ as a term representing individual atomic contributions to the attractive energy. Such a scheme can be used when dealing with the nearest-neighbour shell where the distances to the reference atom are the same. From this alone it can be seen that such a model should be superior to pure pair-potentials for studying surface and defect properties. This square-root form is used by Sutton and Chen in their potential and is the one that will be analyzed in detail in this work.

1.2.1 The Sutton-Chen Potential

Sutton and Chen [18] used the following power-law form for the pairwise repulsive part of their potential

$$V(r) = (a/r)^n \tag{1.2.9}$$

(with n restricted to integer values) and chose the aforementioned $\sqrt{\rho}$ density function. $\rho_i(r)$ in this case was also chosen to be a power-law function, so that

$$\rho_i(r_{ij}) = \sum_{j \neq i} \phi_j(r_{ij}) = \sum_{j \neq i} (a/r_{ij})^m \tag{1.2.10}$$

where m is also restricted to integer values and $n > m$ always. The total energy is then

$$U_{tot} = \epsilon \sum_i \left[\sum_{j \neq i} \left(\frac{a}{r_{ij}} \right)^n - c \left(\sum_{j \neq i} \left(\frac{a}{r_{ij}} \right)^m \right)^{1/2} \right] \tag{1.2.11}$$

with the indices i and j running over all lattice sites. The justification for using this form comes from several key points. Sutton and Chen developed this potential to study clusters of atoms at both near and far ranges. In order to accommodate this, the potential was required to have N-body effects at close ranges and smoothly fall off to an r^{-6}–like van der Waals tail at long ranges. This behaviour is approximately valid only at long ranges as shown in [18]. Additionally, the many-body term can be rewritten as a convenient summation

$$F(\rho) = -c \left(\frac{a}{r_0} \right)^{m/2} \left(s_1 + \frac{s_2}{\sqrt{2}} + \frac{s_3}{\sqrt{3}} + \dots \right)^{1/2} \tag{1.2.12}$$

where r_0 is the nearest-neighbour distance and s_x is the number of atoms in neighbour shell x. The summation shown applies to a FCC lattice since the distance of neighbour shell x is determined by $r_0\sqrt{x}$. This expression holds as long as the lattice is in an undeformed state or is isotropically strained (in which case it can be described by a change in r_0). It is also quite a simple potential, being chiefly defined by the two parameters n and m while ϵ and a simply define the energy and length scales,

Table 1.4: Parameters for the Quantum Sutton-Chen potential from [5]. Cohesive energy and lattice parameter were fit exactly while m and n were restricted to integers that best reproduced the bulk modulus, phonon frequencies and elastic constants.

Metal	m	n	ϵ	c	a (Å)
Cu	5	10	5.7921×10^{-3}	84.843	3.6030
Ag	6	11	3.9450×10^{-3}	96.524	4.0691
Au	8	11	7.8052×10^{-3}	53.581	4.0651
Pt	7	11	9.7894×10^{-3}	71.336	3.9163

respectively. If m and n are found to be the same for two metals, c will also then be the same. a was chosen to be the lattice parameter at room temperature leaving four parameters to be fitted. Values for these were determined by fitting the potential to the experimental cohesive energy and lattice parameter exactly. Fitting to the bulk modulus was not done exactly but rather in such a way as to best reproduce it and C_{11}, C_{12} and C_{44} while keeping m and n restricted to integer values. m was further restricted to be larger than 5 so that the potential did not have too long an interaction range to be useable in computer simulations. The parameters for Cu, Ag, Au and Pt are given in Table 1.3.

The Sutton-Chen potential has been revised by Kimura *et al.* [5] who have included quantum corrections. Their idea was to re-parametrize the potential by including the zero-point energy of the lattice in the free energy. Parameters c and ϵ were determined by equating the free energy to the cohesive energy when the lattice parameter is equal to its experimental value at 0K. This produced a number of candidate sets of parameters n and m. Choices for these were then determined by selecting those integer values that best reproduced the elastic constants, bulk modulus and phonon frequencies. Values for these parameters for the metals considered are given in Table 1.4.

Motivated by some unsatisfactory results of the Sutton-Chen potential and, to a lesser extent, the quantum Sutton-Chen potential (particularly for the thermal expan-

sion coefficient and heat capacity), we developed a modified version of the potential. The aim was to improve results while making minimal changes to the potential. It is shown in Chapter 4 that the electron density of atoms is better represented by an exponential decay at distances close to the nearest-neighbour separation, a result that clearly cannot be described by the power-law interaction present in the Sutton-Chen potential. Because the force constants required to calculate phonon frequencies (and hence other dynamical properties) are directly related to the derivatives of the embedding function, the form of that function is critical in describing those properties. Thus the exponential form chosen for the density is:

$$\rho_i = \sum_{j \neq i} e^{-\alpha(r_{ij}/a - 1)} \tag{1.2.13}$$

with a once again being the length scaling parameter (chosen to be the lattice constant at room temperature) and α is an adjustable parameter.

The second chapter of this work details the theoretical background required to calculate various thermodynamical properties. Following this are results for the Morse, Erkoç and both Sutton-Chen potentials. In the fourth chapter, the motivation and derivation of the Modified Sutton-Chen potential is outlined. The fifth introduces two other potentials that employ an exponential density function. The sixth and final chapter discusses the results of this work.

Chapter 2

Theory and Calculations

2.1 Phonon Dispersion Curves

2.1.1 Theory of Lattice Vibrations

To calculate the phonon dispersion curves, it is sufficient to consider a primitive crystal without loss of generality. Employing a periodic primitive cell and an infinitely extended crystal, displacement of each atom i from its equilibrium position $\mathbf{r}_e(i)$ by the vector $\mathbf{u}(i)$ may be expressed as

$$\mathbf{r}(i) = \mathbf{r}_e(i) + \mathbf{u}(i) \tag{2.1.1}$$

with components given by

$$r^{\alpha}(i) = r_e^{\alpha}(i) + u_{\alpha}(i) \tag{2.1.2}$$

where $\alpha = x, y, z$. The total energy of the crystal can then be written as

$$T = \sum_{i,\alpha} \frac{1}{2} M_i \dot{u}_{\alpha}^2(l) \tag{2.1.3}$$

where $M(i)$ is the mass of atom i and the summation is carried out over all atoms in the crystal. The total potential energy of the crystal is taken to be $\mathbf{\Phi}$ [40], a function

of the instantaneous positions of all the atoms in the crystal. This function can be expanded into a Taylor series of the atomic displacements $\mathbf{u}(i)$:

$$\begin{aligned}\mathbf{\Phi} = \mathbf{\Phi}_e + \sum_{i,\alpha} \mathbf{\Phi}_\alpha(i) u_\alpha(i) + \frac{1}{2} \sum_{\substack{i,j \\ \alpha,\beta}} \mathbf{\Phi}_{\alpha\beta}(i,j) u_\alpha(i) u_\beta(j) \\ + \frac{1}{3!} \sum_{\substack{i,j,k \\ \alpha,\beta,\gamma}} \mathbf{\Phi}_{\alpha\beta\gamma}(i,j,k) u_\alpha(i) u_\beta(j) u_\gamma(k) + \ldots \end{aligned} \tag{2.1.4}$$

with $\mathbf{\Phi}_e$ representing the energy of the crystal when all atoms are in their rest positions. Subsequent terms in the expansion involve derivatives of the potential with respect to atomic displacements, so that:

$$\mathbf{\Phi}_\alpha(i) = \left. \frac{\partial \mathbf{\Phi}}{\partial u_\alpha(i)} \right|_e \tag{2.1.5}$$

$$\mathbf{\Phi}_{\alpha\beta}(i,j) = \left. \frac{\partial^2 \mathbf{\Phi}}{\partial u_\alpha(i) \partial u_\beta(j)} \right|_e \tag{2.1.6}$$

$$\mathbf{\Phi}_{\alpha\beta\gamma}(i,j,k) = \left. \frac{\partial^3 \mathbf{\Phi}}{\partial u_\alpha(i) \partial u_\beta(j) \partial u_\gamma(k)} \right|_e \tag{2.1.7}$$

where the derivatives are evaluated with all atoms in their equilibrium positions. The coefficients $\mathbf{\Phi}_{\alpha\beta}(i,j)$ are known as the *atomic force constants* of the crystal. The coefficients in 2.1.4 are symmetric, such that

$$\mathbf{\Phi}_{\alpha\beta}(i,j) = \mathbf{\Phi}_{\beta\alpha}(j,i) \tag{2.1.8}$$

$$\begin{aligned}\mathbf{\Phi}_{\alpha\beta\gamma}(i,j,k) = \mathbf{\Phi}_{\beta\alpha\gamma}(j,i,k) = \mathbf{\Phi}_{\gamma\alpha\beta}(k,i,j) = \mathbf{\Phi}_{\alpha\gamma\beta}(k,j,i) \\ = \mathbf{\Phi}_{\gamma\beta\alpha}(i,k,j) \text{ (and all other permutations)} \end{aligned} \tag{2.1.9}$$

since the order of a mixed partial derivative is not important. From the definition of Eq. 2.1.5, it is clear that $\mathbf{\Phi}_\alpha(i)$ is the negative of the force acting on the particle at $\mathbf{r}(i)$ in the α direction. In equilibrium, this term must be zero since the net force

on any individual atom must be zero:

$$\mathbf{\Phi}_\alpha(i) = -\, F_\alpha(i)\big|_e \tag{2.1.10}$$

$F_\alpha(i)$ denotes the Cartesian component α of a force $\mathbf{F}(i)$ on an atom at $\mathbf{r}(i)$. An extension of this interpretation of 2.1.5 can be applied to 2.1.6: it is the negative rate of change of the force in direction α on atom i with respect to displacement of atom j in the β direction, all other atoms remaining in their equilibrium positions. It can be written as

$$\mathbf{\Phi}_{\alpha\beta}(i,j) = -\left.\frac{\partial F_\alpha(i)}{\partial u_\beta(j)}\right|_e \tag{2.1.11}$$

A number of conditions may be imposed on the force constants by subjecting the lattice as a whole to an infinitesimal rigid body translation $\mathbf{v}$. The potential and its derivatives must remain unchanged since these term all depend on the relative separation of atoms. Because of this, the following must hold [41]:

$$\sum_i \mathbf{\Phi}_\alpha(i) = 0 \tag{2.1.12}$$

$$\sum_i \mathbf{\Phi}_{\alpha\beta}(i,j) = \sum_j \mathbf{\Phi}_{\alpha\beta}(i,j) = 0 \tag{2.1.13}$$

$$\sum_i \mathbf{\Phi}_{\alpha\beta\gamma}(i,j,k) = \sum_j \mathbf{\Phi}_{\alpha\beta\gamma}(i,j,k) = \sum_k \mathbf{\Phi}_{\alpha\beta\gamma}(i,j,k) = 0 \tag{2.1.14}$$

and so on for higher order terms.

The hamiltonian for the crystal is simply the sum of the kinetic and potential energies:

$$H = T + \mathbf{\Phi} \tag{2.1.15}$$

Working in the harmonic approximation, where all terms in the expansion of $\mathbf{\Phi}$ (2.1.4) with derivatives of higher order than 2 are neglected, the vibrational Hamiltonian

takes the form

$$H = \mathbf{\Phi}_e + \frac{1}{2}\sum_{\alpha,i} M_i \dot{u}_\alpha^2(i) + \frac{1}{2}\sum_{\substack{i,j \\ \alpha,\beta}} \mathbf{\Phi}_{\alpha\beta}(i,j) u_\alpha(i) u_\beta(j) \tag{2.1.16}$$

If we write the momentum of the lth atom as $\mathbf{p}(l)$ with components $p_i(l)$, equation 2.1.16 may be written as

$$H = \mathbf{\Phi}_e + \sum_{\alpha,i} \frac{p_\alpha^2(i)}{2M_i} + \frac{1}{2}\sum_{\substack{i,j \\ \alpha,\beta}} \mathbf{\Phi}_{\alpha,\beta}(i,j) u_\alpha(i) u_\beta(j) \tag{2.1.17}$$

and from this a set of equations of motion may be obtained:

$$M_i \ddot{u}_\alpha(i) = -\frac{\partial \mathbf{\Phi}}{\partial u_\alpha(i)} = -\sum_{j,\beta} \mathbf{\Phi}_{\alpha\beta}(i,j) u_\beta(j) \tag{2.1.18}$$

These form a set of simultaneous linear differential equations whose solutions may be simplified by the use of periodic boundary conditions and the constraints on the atomic force constants that follow from symmetries of the crystal. These restrictions come from the fact that the potential energy must be independent of rigid translations and rotations of the crystal as well as reflections in any symmetry planes. Solutions to this set of equations are then chosen to be

$$u_\alpha(i) = \frac{1}{\sqrt{M_i}} e_\alpha(i|\mathbf{k}_s) e^{-\mathbf{i}\omega_s(\mathbf{k})t + \mathbf{i}\mathbf{k}\cdot\mathbf{r}(l)} \tag{2.1.19}$$

The vector $\mathbf{k}$ is called the wave vector and it has magnitude 2π divided by the wavelength of an elastic wave propagating through the medium. Its direction is of course in the direction of propagation of the wave. The subscript s denotes the polarization of the phonons and takes one of three values (1,2,3) in a 3-dimensional crystal. The coefficients $e_\alpha(i|\mathbf{k}s)$ satisfy

$$\omega_s^2(\mathbf{k}) e_\alpha(i|\mathbf{k}_s) = \sum_{j,\beta} D_{\alpha\beta}(i,j|\mathbf{k}) e_\beta(j|\mathbf{k}_s) \tag{2.1.20}$$

where $D_{\alpha\beta}(i,j|\mathbf{k})$ is the dynamical matrix and is given by:

$$D_{\alpha\beta}(i,j|\mathbf{k}) = \frac{1}{\sqrt{M_i M_j}} \sum_j \mathbf{\Phi}_{\alpha\beta}(i,j) e^{-\mathbf{i}\mathbf{k}\cdot(\mathbf{r}(i)-\mathbf{r}(j))} \tag{2.1.21}$$

D is a hermitian matrix and has the following properties:

$$D_{\alpha\beta}(i,j|\mathbf{k}) = D^*_{\alpha\beta}(j,i|\mathbf{k}) \tag{2.1.22}$$

$$D_{\alpha\beta}(i,j|-\mathbf{k}) = D^*_{\alpha\beta}(i,j|\mathbf{k}) \tag{2.1.23}$$

In order to obtain a non-trivial solution to Eq. 2.1.20, the determinant of coefficients must vanish:

$$\left|D_{\alpha\beta}(i,j|\mathbf{k}) - \omega_s^2(\mathbf{k})\delta_{\alpha\beta}\delta_{ij}\right| = 0 \tag{2.1.24}$$

which is a 3×3 secular equation. The roots of the eigenvalues of the dynamical matrix are the phonon frequencies $\omega_s(\mathbf{k})$ which of course have three values for each value of $\mathbf{k}$.

Since Eq. 2.1.20 defines $e_\alpha(i|\mathbf{k}_s)$ only to within an arbitrary constant, they are also assumed to satisfy orthonormality and closure conditions:

$$\sum_\alpha e^*_\alpha(i|\mathbf{k}_s) e_\alpha(i|\mathbf{k}_{s'}) = \delta_{ss'} \tag{2.1.25}$$

$$\sum_s e^*_\alpha(i|\mathbf{k}_s) e_\beta(j|\mathbf{k}_s) = \delta_{\alpha\beta}\delta_{ij} \tag{2.1.26}$$

In the following sections, calculations involving derivatives with respect to atomic positions $\mathbf{r}_i$ are used in place of the atomic displacements $\mathbf{u}(i)$ for clarity. Because the two are related linearly, the results remain unaffected.

2.1.2 Phonon Frequencies

We now apply the theory of phonon vibration to the Sutton-Chen potential, keeping the notation of the previous section. Beginning with the general form of the total

energy from Eq. 1.2.1 and using 1.2.6, the potential between any pair of atoms i, j is

$$\mathbf{\Phi} = \epsilon\big[V(r_{ij}) - c\sqrt{\rho_i}\big] \tag{2.1.27}$$

where $r_{ij} = |\mathbf{r}_j - \mathbf{r}_i|$.

Following the expansion in Eq. 2.1.4, the first term is

$$\mathbf{\Phi}_\alpha(i,j) = \epsilon\left[\frac{\partial V(r_{ij})}{\partial r_{ij}^\alpha} - c\frac{\partial}{\partial r_{ij}^\alpha}\left(\rho_i^{1/2}\right)\right] \tag{2.1.28}$$

which using Eq. 1.2.2 then becomes

$$\mathbf{\Phi}_\alpha(i,j) = \epsilon\left[V'(r_{ij})\frac{r_{ij}^\alpha}{r_{ij}} - \frac{c}{2\rho_i^{1/2}}\left(\sum_{k\neq j}\phi'(r_{jk})\frac{r_{jk}^\alpha}{r_{jk}}\right)\right] \tag{2.1.29}$$

with the primes denoting derivatives with respect to the functions' variables and $r_{ij}^\alpha = r_j^\alpha - r_i^\alpha$ (the distance between atoms i and j). The first derivative does not appear in the dynamical matrix, however, because at equilibrium the net force on each atom is zero. The second derivative is required and it is given below:

$$\begin{aligned}
\mathbf{\Phi}_{\alpha\beta}(i,j) = &-\epsilon\left[\big(V_{ij}'' - V_{ij}'\big)\frac{r_{ij}^\alpha r_{ij}^\beta}{r_{ij}^2} + V_{ij}'\frac{\delta_{\alpha\beta}}{r_{ij}^2}\right] - \frac{\epsilon c}{4\rho_i^{3/2}}\left(\sum_{k\neq i}\phi_{ij}'\frac{r_{ik}^\alpha}{r_{ik}}\right)\phi_{ij}'\frac{r_{ij}^\beta}{r_{ij}} \\
&+ \frac{\epsilon c}{2\rho_i^{1/2}}\left[\big(\phi_{ij}'' - \phi_{ij}'\big)\frac{r_{ij}^\alpha r_{ij}^\beta}{r_{ij}^2} + \phi_{ij}'\frac{\delta_{\alpha\beta}}{r_{ij}^2}\right] + \frac{\epsilon c}{4\rho_j^{3/2}}\phi_{ij}'\frac{r_{ij}^\alpha}{r_{ij}}\left(\sum_{k\neq j}\phi_{jk}'\frac{r_{jk}^\beta}{r_{jk}}\right) \\
&+ \frac{\epsilon c}{2\rho_j^{1/2}}\left[\big(\phi_{ij}'' - \phi_{ij}'\big)\frac{r_{ij}^\alpha r_{ij}^\beta}{r_{ij}^2} + \phi_{ij}'\frac{\delta_{\alpha\beta}}{r_{ij}^2}\right] + \frac{1}{4}\sum_{k\neq i,j}\left[\frac{\epsilon c}{\rho_k^{3/2}}\Big(\phi_{ik}'\frac{r_{ik}^\alpha}{r_{ik}}\phi_{jk}'\frac{r_{jk}^\beta}{r_{jk}}\Big)\right]
\end{aligned} \tag{2.1.30}$$

From Eqs. 1.2.9 and 1.2.10 we have:

$$V_{ij}' = V'(r_{ij}) = -n\frac{a^n}{r_{ij}^{n+1}} \tag{2.1.31}$$

$$V_{ij}'' = V''(r_{ij}) = (n^2+n)\frac{a^n}{r_{ij}^{n+2}} \tag{2.1.32}$$

$$\phi_{ij}' = \phi'(r_{ij}) = -m\frac{a^m}{r_{ij}^{m+1}} \tag{2.1.33}$$

$$\phi_{ij}'' = \phi''(r_{ij}) = (m^2+m)\frac{a^m}{r_{ij}^{m+2}} \tag{2.1.34}$$

Using Eq. 2.1.13, it can be seen that

$$\mathbf{\Phi}_{\alpha\beta}(i,i) = -\sum_{j\neq i} \mathbf{\Phi}(i,j) \tag{2.1.35}$$

which means that Eq. 2.1.21 may be rewritten:

$$\begin{aligned} D_{\alpha\beta}(i,j|\mathbf{k}) &= \frac{1}{\sqrt{M_i M_j}} \sum_j \mathbf{\Phi}_{\alpha\beta}(i,j) e^{-\mathbf{i}\mathbf{k}\cdot(\mathbf{r}(i)-\mathbf{r}(j))} \\ &= \frac{1}{\sqrt{M_i M_j}} \left[\mathbf{\Phi}_{\alpha\beta}(i,i) + \sum_{j\neq i} \mathbf{\Phi}_{\alpha\beta}(i,j) e^{-\mathbf{i}\mathbf{k}\cdot(\mathbf{r}(i)-\mathbf{r}(j))} \right] \\ &= \frac{1}{\sqrt{M_i M_j}} \sum_{j\neq i} \left[\mathbf{\Phi}_{\alpha\beta}(i,j) e^{-\mathbf{i}\mathbf{k}\cdot(\mathbf{r}(i)-\mathbf{r}(j))} - 1 \right] \end{aligned} \tag{2.1.36}$$

Combining this result with Eq. 2.1.30 allows one to calculate the dynamical matrix for this model. Eight neighbour shells were included in the calculations for the Sutton-Chen and Quantum Sutton-Chen potentials (a total of 141 atoms) while the Modified Sutton-Chen utilized six shells (87 atoms). Solving the secular equation (2.1.24) then leads to the phonon frequencies by simply taking the square-root of the eigenvalues. In the case of pair potentials, Eq. 2.1.30 reduces to

$$\mathbf{\Phi}_{\alpha\beta}(i,j) = -\epsilon \left[\left(V''_{ij} - V'_{ij}\right) \frac{r^{\alpha}_{ij} r^{\beta}_{ij}}{r^2_{ij}} + V'_{ij} \frac{\delta_{\alpha\beta}}{r^2_{ij}} \right] \tag{2.1.37}$$

Also true for pair-potentials is a simplified calculation of the elements of the 3×3 dynamical matrix via [42]

$$\begin{aligned} D_{ii} &= \frac{8}{M} \sum_s \frac{n^s}{48} \sum_j \alpha^s_j \left\{ 2 - C^s_{j,i} \left[C^s_{j+1,i+1} C^s_{j+2,i+2} + C^s_{j+2,i+1} C^s_{j+1,i+2} \right] \right\} \\ D_{i,i+1} &= \frac{8}{M} \sum_s \frac{n^s}{48} \sum_j \beta^s_j C^s_{j,i+2} \left[S^s_{j+1,i} S^s_{j+2,i+1} + S^s_{j+2,i} S^s_{j+1,i+1} \right] \end{aligned} \tag{2.1.38}$$

where

$$C^s_{j,i} = \cos(\pi a h^s_j k_i), \quad S^s_{j,i} = \sin(\pi a h^s_j k_i) \tag{2.1.39}$$

n^s is the number of neighbours in shell s, M is the atomic mass and α^s_j and β^s_j are the atomic force constants. h^s_j are the atomic position vector components and the k_i

are the components of the incident wavevector $\mathbf{k}$. Subscripts of the form $i+1$ and $i+2$ whose values are greater than 3 are interpreted as $i-2$ and $i-1$, respectively (likewise for j).

In order to make use of these frequencies for computing dynamical properties, a continuum of points describing the First Brillouin Zone (FBZ) would theoretically be required. In practice, one uses a mesh of points to approximate the FBZ; in this work a $20 \times 20 \times 20$-point mesh was used. For each of these $\mathbf{k}$-values, the dynamical matrix was computed and the eigenvalues obtained.

2.2 Thermodynamical Properties

2.2.1 Zero-Point Energy

To determine the zero-point energy of the vibrational Hamiltonian, we begin with the introduction of a pair of operators, $b^\dagger_{\mathbf{k}_s}$ and $b_{\mathbf{k}_s}$. These are the phonon creation and annihilation operators, respectively. They satisfy the commutation relations

$$\left[b_{\mathbf{k}_s}, b_{\mathbf{k}'_{s'}}\right] = \left[b^\dagger_{\mathbf{k}_s}, b^\dagger_{\mathbf{k}'_{s'}}\right] = 0 \tag{2.2.1}$$

$$\left[b_{\mathbf{k}_s}, b^\dagger_{\mathbf{k}'_{s'}}\right] = \Delta(\mathbf{k}-\mathbf{k}')\delta_{ss'} \tag{2.2.2}$$

where

$$\Delta(\mathbf{k}) = \frac{1}{N}\sum_i e^{\mathbf{i}\mathbf{k}\cdot\mathbf{r}_i} \tag{2.2.3}$$

It is convenient to use expansions of u_i^α and p_i^α in terms of plane waves, so that

$$u_i^\alpha = \left(\frac{\hbar}{2NM_i}\right)^{1/2} \sum_{\mathbf{k}_s} \frac{1}{\sqrt{\omega_s(\mathbf{k})}} e_\alpha(i|\mathbf{k}_s) e^{\mathbf{i}\mathbf{k}\cdot\mathbf{r}_i} \left[b_{\mathbf{k}_s} + b^\dagger_{-\mathbf{k}_s}\right] \tag{2.2.4}$$

$$p_i^\alpha = -\mathbf{i}\left(\frac{\hbar M_i}{2N}\right)^{1/2} \sum_{\mathbf{k}_s} \sqrt{\omega_s(\mathbf{k})} e_\alpha(i|\mathbf{k}_s) e^{\mathbf{i}\mathbf{k}\cdot\mathbf{r}_i} \left[b_{\mathbf{k}_s} - b^\dagger_{-\mathbf{k}_s}\right] \tag{2.2.5}$$

where $\hbar$ is the reduced Planck's constant, N is the number of primitive cells in a parallelepiped which fills all of the crystal space (without gaps or overlap), $\mathbf{r}_i$ is the displacement between the reference atom and atom i and $\mathbf{k}$ and $\mathbf{k}'$ are restricted to lie inside the FBZ. The derivation of the above is similar to that of the raising and lowering operators of the simple harmonic oscillator [41]. Making use of these new operators yields the following expression for the Hamiltonian:

$$H = \sum_{\mathbf{k}_s} \hbar\omega_s(\mathbf{k}) \left[b^\dagger_{\mathbf{k}_s} b_{\mathbf{k}_s} + \frac{1}{2} \right] \tag{2.2.6}$$

Defining the ground state as

$$b_{\mathbf{k}_s} |0\rangle = 0 \tag{2.2.7}$$

for all $\mathbf{k}_s$, the solutions to the Hamiltonian (2.2.6) can be written:

$$\begin{aligned} &|n_{s_1}(\mathbf{k}_1), \ldots, n_{s_3}(\mathbf{k}_1), \ldots, n_{s_1}(\mathbf{k}_N, \ldots, n_{s_3}(\mathbf{k}_N)\rangle \\ &= \left(\prod_{\mathbf{k}}^{N} \prod_{s=1}^{3} (n_{\mathbf{k}_s})! \right)^{-1/2} \prod_{\mathbf{k}}^{N} \prod_{s=1}^{3} (b^\dagger_{\mathbf{k}_s})^{n_{\mathbf{k}_s}} |0\rangle \end{aligned} \tag{2.2.8}$$

with energy eigenvalues

$$E(n_{\mathbf{k}_s}) = \sum_{\mathbf{k}}^{N} \sum_{s=1}^{3} \hbar\omega_s(\mathbf{k}) \left[n_{\mathbf{k}_s} + \frac{1}{2} \right] \tag{2.2.9}$$

where $n_{\mathbf{k}_s} = 0, 1, 2, \ldots$ is the number of phonons of frequency $\omega_s(\mathbf{k})$ present in state (2.2.8). Looking at Eq. 2.2.9, the zero-point energy is clearly the energy when $n_{\mathbf{k}_s} = 0$,

$$E_0 = \sum_{\mathbf{k}_s} \frac{1}{2} \hbar\omega_s(\mathbf{k}) \tag{2.2.10}$$

2.2.2 Linear Thermal Expansion

Derivation of the thermodynamical functions of a crystal in the harmonic approximation begins with the partition function:

$$Z = Tr\{e^{-\beta H}\} \tag{2.2.11}$$

with H being the Hamiltonian and $\beta = 1/k_BT$ (where k_B is Boltzmann's constant and T is the absolute temperature). Working in the space in which H is diagonal, the partition function can be written as

$$\begin{aligned} Z &= \sum_{n_{\mathbf{k}_1} s_1=0}^{\infty} \cdots \sum_{n_{\mathbf{k}_N} s_3=0}^{\infty} \exp\left\{-\beta \sum_{\mathbf{k}_s} \hbar\omega_s(\mathbf{k})\left[n_{\mathbf{k}_s} + \frac{1}{2}\right]\right\} \\ &= \prod_{\mathbf{k}_s} \frac{e^{-\frac{1}{2}\beta\hbar\omega_s(\mathbf{k})}}{1 - e^{-\beta\hbar\omega_s(\mathbf{k})}} \end{aligned} \tag{2.2.12}$$

When working with thermodynamic properties of materials at equilibrium, the Helmholtz free energy is most useful since those properties depend on the minimum of that energy. It is formally defined as

$$F = U - TS \tag{2.2.13}$$

where U is the internal energy and S is the entropy of the system. In dealing with phonon vibrational energy, it can also be related to the partition function via

$$F_{vib} = -k_BT\log Z = k_BT \sum_{\mathbf{k}_s} \log\left[2\sinh\frac{\hbar\omega_s(\mathbf{k})}{2k_BT}\right] \tag{2.2.14}$$

Using Eq. 2.2.13, the differential energy can be expressed as

$$dF = -SdT - PdV + \mu dN \tag{2.2.15}$$

where the relation

$$dS = \frac{1}{T}\left(dU + PdV - \mu dN\right) \tag{2.2.16}$$

was used [43]. Since in our case the number of particles is constant, $dN = 0$ and the following relation for entropy emerges:

$$S = -\left(\frac{\partial F}{\partial T}\right)_V \tag{2.2.17}$$

Making use of Eq. 2.2.14,

$$S_{vib} = k_B \sum_{\mathbf{k}_s} \left[\frac{\hbar\omega_s(\mathbf{k})}{2k_BT} \coth\Big(\frac{\hbar\omega_s(\mathbf{k})}{2k_BT}\Big) - \log\Big\{ 2\sinh\Big(\frac{\hbar\omega_s(\mathbf{k})}{2k_BT}\Big)\Big\}\right] \tag{2.2.18}$$

Combining Eqs. 2.2.14 and 2.2.18 yields

$$U_{vib} = F_{vib} + TS_{vib} = \sum_{\mathbf{k}_s} \frac{1}{2}\hbar\omega_s(\mathbf{k}) \coth\Big(\frac{\hbar\omega_s(\mathbf{k})}{2k_BT}\Big) \tag{2.2.19}$$

Having an expression for the vibrational contribution to the internal energy, we now add to it the static energy of the crystal to obtain the full Helmholtz free energy at temperature T and volume V (or equivalently at lattice parameter a):

$$F(a,T) = U_{tot} + F_{vib}(a,T) = U_{tot} + k_BT \sum_{\mathbf{k}_s} \log\Big\{ 2\sinh\frac{\hbar\omega_s(\mathbf{k},a)}{2k_BT}\Big\} \tag{2.2.20}$$

U_{tot} is the static crystal contribution to the energy. The vibration free energy F_{vib} is an explicit function of T and an implicit function of a through the phonon frequencies $\omega_s(\mathbf{k}, a)$. The contribution to the free energy from the electron gas has been neglected since it is small and insignificant below about 10K [12].

Given that there is zero pressure on the crystal, the equilibrium lattice parameter at a temperature T can be determined by minimizing the free energy as follows:

$$\left(\frac{\partial F(a,T)}{\partial a}\right)_T = \frac{\partial U}{\partial a} + \left(\frac{\partial F_{vib}(a,T)}{\partial a}\right)_T = 0 \tag{2.2.21}$$

When working with this expression, it is convenient to express it in terms of the energy per atom rather than the total energy. As was stated in the previous section, the summation of the $\mathbf{k}$ vectors is carried out on a $20 \times 20 \times 20$-point mesh in the FBZ to determine the vibrational contribution to the free energy. This is carried out for each value of T over a range from nearly 0K to 1250K in increments of 10K. The lattice parameter is varied at each value of T until (2.2.21) is satisfied. This value of a is then taken to be the equilibrium lattice parameter at that T and labeled $a_e(T)$.

The linear thermal expansion coefficient can then be determined using

$$\alpha(T) = \frac{1}{a_e(T)} \left(\frac{da_e(T)}{dT} \right)_P \tag{2.2.22}$$

However, in order to compare theoretical results with those obtained from experiment, a rescaled version of Eq. 2.2.22 is used:

$$\alpha(T) = \frac{1}{a_e(T_c)} \left(\frac{da_e(T)}{dT} \right)_P \tag{2.2.23}$$

where T_c is a reference temperature, set to $293K$ for the results in this work.

2.2.3 Isothermal Bulk Modulus

The isothermal bulk modulus describes a substance's resistance to compression and is the inverse of the isothermal compressibility. Deriving an expression for B_T, the bulk modulus in question, begins by obtaining the equation of state for the system. At a given T and V, the pressure is given by

$$P = -\left(\frac{\partial F}{\partial V} \right)_T \tag{2.2.24}$$

The bulk modulus has volume dependence given by [43]

$$B_T = -V \left(\frac{\partial P}{\partial V} \right)_T \tag{2.2.25}$$

which when combined with 2.2.24 yields:

$$\begin{aligned} B_T &= V \left(\frac{\partial^2 F}{\partial V^2} \right)_T \\ &= V \left(\frac{\partial^2 U}{\partial V^2} \right)_T + V \left(\frac{\partial^2 F_{vib}(a,T)}{\partial V^2} \right)_T \end{aligned} \tag{2.2.26}$$

It is convenient to express this derivative in terms of lattice parameter rather than volume, a modification that can be achieved by using the volume per atom in a FCC

crystal:

$$V = \frac{1}{4}a^3 \tag{2.2.27}$$

$$\frac{\partial V}{\partial a} = \frac{3}{4}a^2 \tag{2.2.28}$$

and so,

$$\partial V = \frac{3}{4}a^2 \partial a \tag{2.2.29}$$

Eq. 2.2.26 then becomes

$$B_T = \frac{4}{9a}\left[\left(\frac{\partial^2 U}{\partial a^2}\right)_T + \left(\frac{\partial^2 F_{vib}(a,T)}{\partial a^2}\right)_T\right] \tag{2.2.30}$$

and is calculated numerically since the a dependence of $F_{vib}(a,T)$ is implicit in the phonon frequencies.

2.2.4 Heat Capacity C_V and C_P

Eq. 2.2.19 can be used to determine the specific heat at constant volume of the crystal, C_V.

$$\begin{aligned} C_V &= \sum_{\mathbf{k},s} C_V(\mathbf{k}_s) = \left(\frac{\partial U}{\partial T}\right)_V \\ &= k_B \sum_{\mathbf{k}_s} \left(\frac{\hbar\omega_s(\mathbf{k})}{2k_B T}\right)^2 \frac{1}{\sinh^2[\hbar\omega_s(\mathbf{k})/2k_B T]} \end{aligned} \tag{2.2.31}$$

This accounts for the phonon contribution to the specific heat but neglects the electronic contribution. This must be added separately:

$$C_V = C_V^{ph} + C_V^{el} \tag{2.2.32}$$

The electronic contribution can be calculated using the density of states at the Fermi level as was done previously in [44] using the STUTTGART TB-LMTO-ASA program.

The specific heat at constant pressure, C_P, is related to that at constant volume

by

$$C_P - C_V = -T\left(\frac{\partial V}{\partial T}\right)_T^2 \left(\frac{\partial P}{\partial V}\right)_T \tag{2.2.33}$$

which can be written

$$C_P - C_V = \alpha_V^2 B_T V T \tag{2.2.34}$$

by using the definition of the volume thermal expansion:

$$\alpha_V = \frac{1}{V}\left(\frac{\partial V}{\partial T}\right)_P \tag{2.2.35}$$

The volume thermal expansion coefficient is simply derived from the linear thermal expansion coefficient via $\alpha_V = 3\alpha$. Once again converting Eq. 2.2.34 into an expression involving lattice parameter rather than volume and adding in the electronic contribution yields

$$C_P = C_V^{ph} + C_V^{el} + \frac{9a^3}{4}\alpha^2 B_T T \tag{2.2.36}$$

Once again the calculation is done by using a set number of irreducible points in the FBZ to carry out the summation over the phonon frequencies. This allows the third term in Eq. 2.2.36 to be determined, at which point it is added to the other two terms to obtain the results for the temperature-dependent C_P.

2.2.5 Adiabatic Bulk Modulus

Starting with the adiabatic compressibility [43],

$$K_S(T) = -\frac{1}{V}\left(\frac{\partial V}{\partial P}\right)_S \tag{2.2.37}$$

the adiabatic bulk modulus can be written as the reciprocal of the compressibility:

$$B_S(T) = \big(K_S(T)\big)^{-1} = -V\left(\frac{\partial P}{\partial V}\right)_S \tag{2.2.38}$$

Similarly, the isothermal compressibility is

$$K(T) = -\frac{1}{V}\left(\frac{\partial V}{\partial P}\right)_T \tag{2.2.39}$$

which is of course the reciprocal of the isothermal bulk modulus. It can then be shown [43] that

$$K(T) - K_S(T) = \frac{TV\alpha_V^2(T)}{C_P} \tag{2.2.40}$$

which can be combined with Eq. 2.2.34 to yield

$$C_P\left(K(T) - K_S(T)\right) = K(T)(C_P - C_V) \tag{2.2.41}$$

and so,

$$B_S(T) = \frac{C_P}{C_V}B(T) \tag{2.2.42}$$

2.2.6 Grünesien Parameter

The Grüneisen parameter describes the relative rate of change of phonon frequencies with volume. It can be derived beginning with the equation of state:

$$\begin{aligned} P &= -\left(\frac{\partial F}{\partial V}\right)_T \\ &= -\frac{\partial U(a)}{\partial V} + \frac{1}{V}\sum_{\mathbf{k},s}\gamma_s(\mathbf{k})\epsilon(\omega_s(\mathbf{k})) \end{aligned} \tag{2.2.43}$$

where the Grüneisen parameter $\gamma_s(\mathbf{k})$ for each phonon mode s with wavevector $\mathbf{k}$ is given by

$$\gamma_s(\mathbf{k}) = -\frac{V}{\omega_s(\mathbf{k})}\frac{\partial\omega_s(\mathbf{k})}{\partial V} \tag{2.2.44}$$

The mean vibrational energy, ϵ, of the phonon modes is

$$\epsilon\big(\omega_s(\mathbf{k})\big) = \hbar\omega_s(\mathbf{k})\left[\frac{1}{2} + \frac{1}{e^{\hbar\omega_s(\mathbf{k})/k_BT} - 1}\right] \tag{2.2.45}$$

The overall Grüneisen parameter is taken as an average of the individual parameters for each vibrational mode. These are weighted by the isochoric heat capacity $C_V(\mathbf{k}, s)$

of each phonon mode. Thus,

$$\gamma(T) = \frac{\sum_{\mathbf{k},s} \gamma_s(\mathbf{k}) C_V(\mathbf{k}, s)}{\sum_{\mathbf{k},s} C_V(\mathbf{k}, s)} \tag{2.2.46}$$

whre the weight factors $C_V(\mathbf{k}, s)$ are calculated using Eq. 2.2.31. Due to the difficulty in experimentally measuring this parameter, the available data is limited. It can also be calculated using several bulk properties of the solid, as shown below:

$$\gamma = \frac{\alpha}{B_T C_V \rho} \tag{2.2.47}$$

where ρ is the density of the solid and the other variables are as they were defined previously. This is a less accurate definition of γ, however, due to the fact that all phonon modes are implicitly given equal weight.

2.2.7 Root-Mean-Square Displacement

The root-mean-square (RMS) displacement of atoms in a crystal describes the (thermally averaged) deviation of their positions from equilibrium values. Such an expression can be derived from the partition function and is given by [40]

$$\left\langle \bar{u^2} \right\rangle_T = \sum_{\mathbf{k},s} \frac{\hbar}{2M\omega_s(\mathbf{k})} \coth\left(\frac{\beta\hbar\omega_s(\mathbf{k})}{2}\right) \tag{2.2.48}$$

This can be a useful tool for predicting melting temperatures of solids, as was first discussed by Lindemann [45]. He stated that RMS displacement of atoms in a crystal in excess of $10 - 12\%$ of the nearest-neighbour distance can be interpreted as the beginning of melting. Because this value is only an estimate of when melting should occur, one cannot fault a potential for not reproducing this result exactly. Only large deviation from it may be considered significant.

Chapter 3

Results

3.1 Pair-Potentials

Shown in Figs. 3.1 to 3.21 are the phonon dispersion curves, thermal expansion coefficient, adiabatic and isothermal bulk moduli, specific heat at constant pressure, Grüneisen parameter and root-mean-square displacement as a function of temperature for the Morse and Erkoç potentials. The Morse potential has two sets of parameters associated with it, one determined using the vacancy formation energy and the other using sublimation energy. They are denoted Morse-V and Morse-S, respectively. In the following calculations the interaction range of the potentials was extended to include up to twelve neighbour shells.

For both Cu and Ag, the Erkoç potential performs significantly better than the Morse-V and Morse-S when predicting the phonon dispersion curves. For Cu, the Erkoç predicts frequencies that are 4% too high at the X-point while the Morse-V and Morse-S overestimate the values by 14% and 40%, respectively. The slopes of these curves near the zone center are considerably lower for the Erkoç, however. Ag presents a similar situation where the Erkoç predicts frequencies 9% too high in the [100] direction while the Morse-S is far higher at 39% at the X-point. The situation

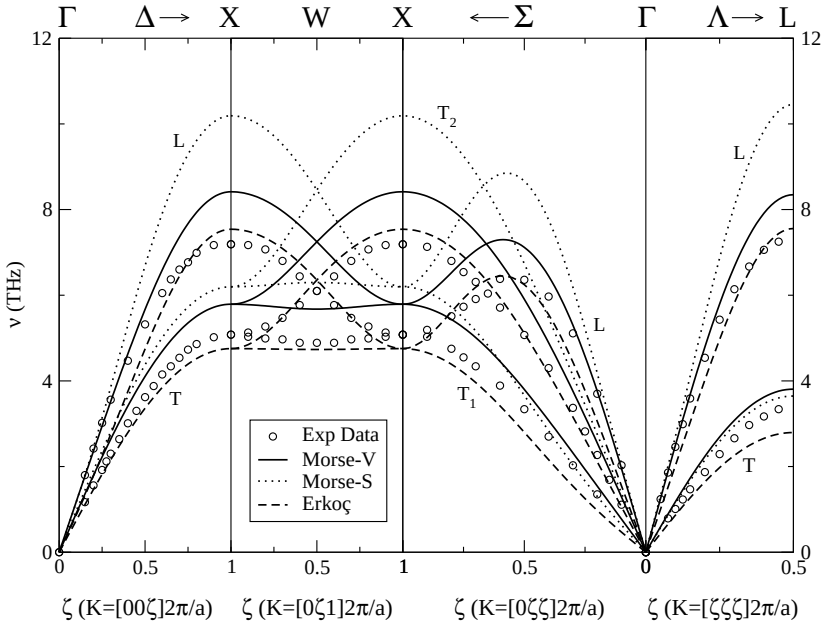

Figure 3.1: Phonon dispersion curves for Cu as calculated using the Morse and Erkoç potentials. Experimental data taken from [6].

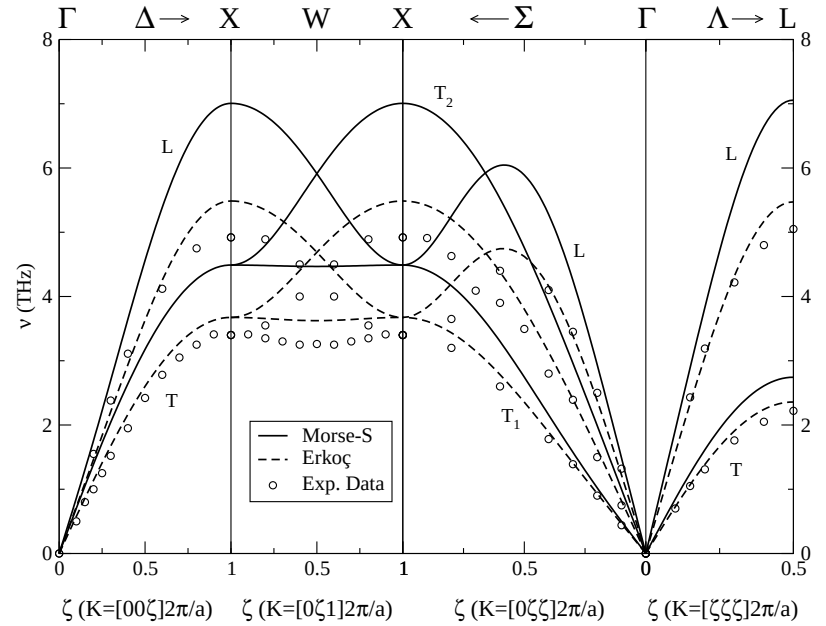

Figure 3.2: Phonon dispersion curves for Ag as calculated using the Morse and Erkoç potentials. Experimental data taken from [7].

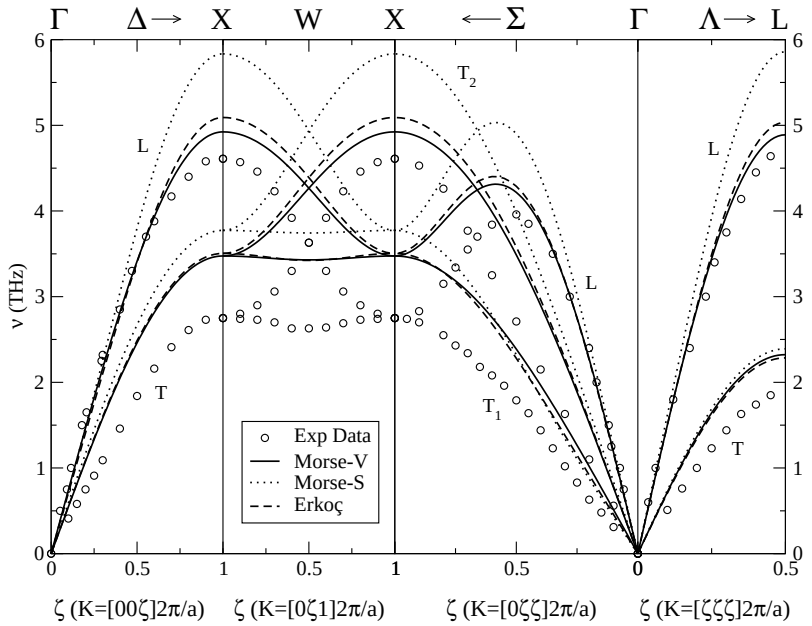

Figure 3.3: Phonon dispersion curves for Au as calculated using the Morse and Erkoç potentials. Experimental data taken from [8].

changes for Au where the Morse-V is now closest to experiment, albeit only just. All calculated curves are far too high for the transverse branches, particularly in the [100] direction. The Morse-V is nearest with a 21% overestimation.

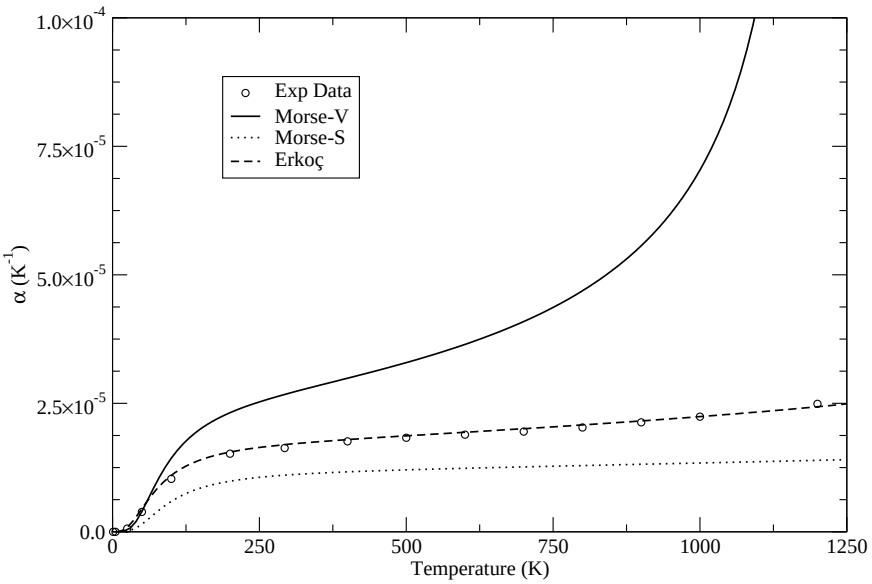

Figure 3.4: Thermal expansion coefficient for Cu as calculated using the Morse and Erkoç potentials. Experimental data taken from [9].

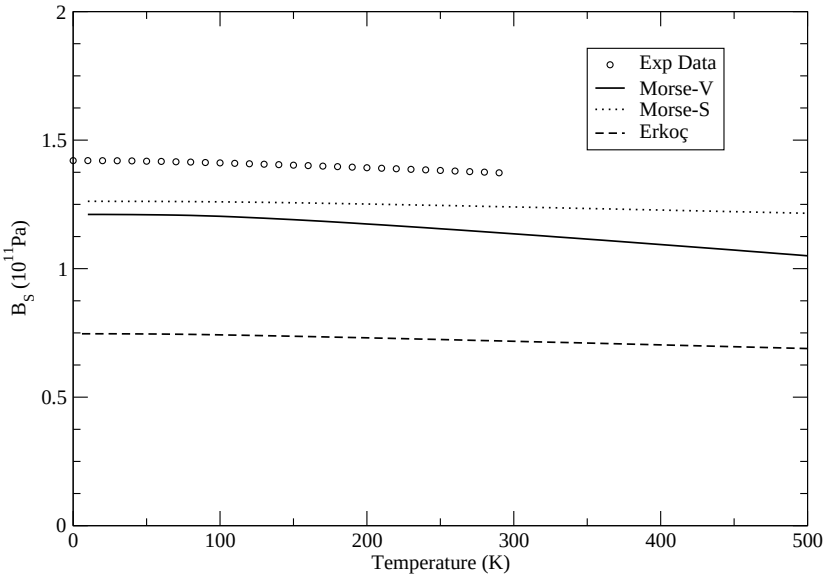

Figure 3.5: Adiabatic bulk modulus for Cu as calculated using the Morse and Erkoç potentials. Experimental data taken from [10].

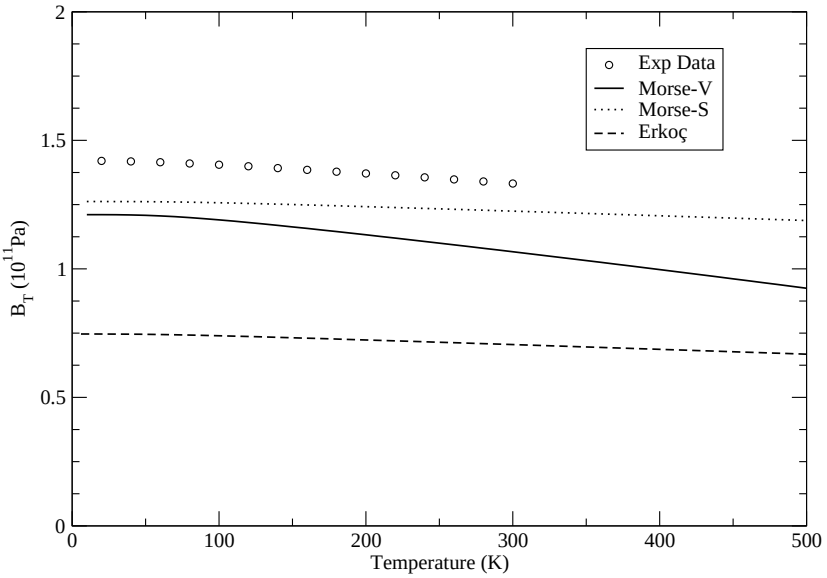

Figure 3.6: Isothermal bulk modulus for Cu as calculated using the Morse and Erkoç potentials. Experimental data taken from [11] and [12].

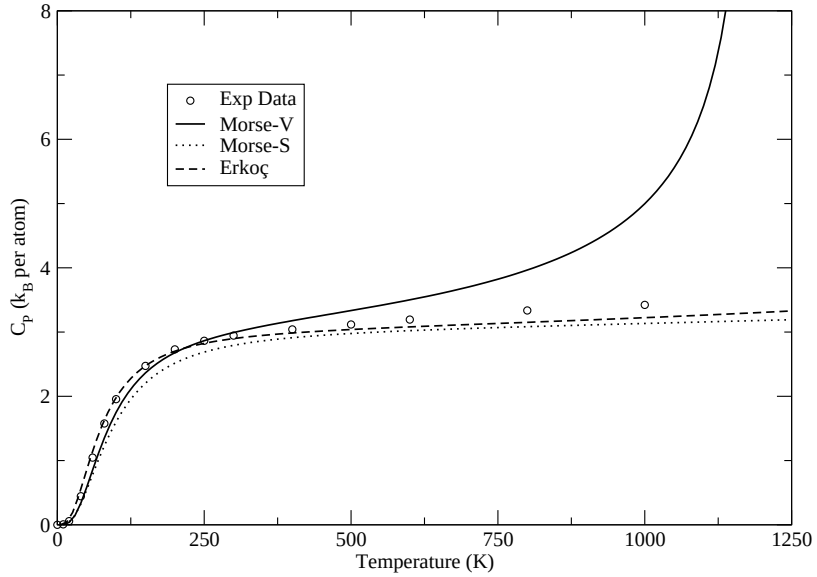

Figure 3.7: Specific heat at constant pressure for Cu as calculated using the Morse and Erkoç potentials. Experimental data taken from [13].

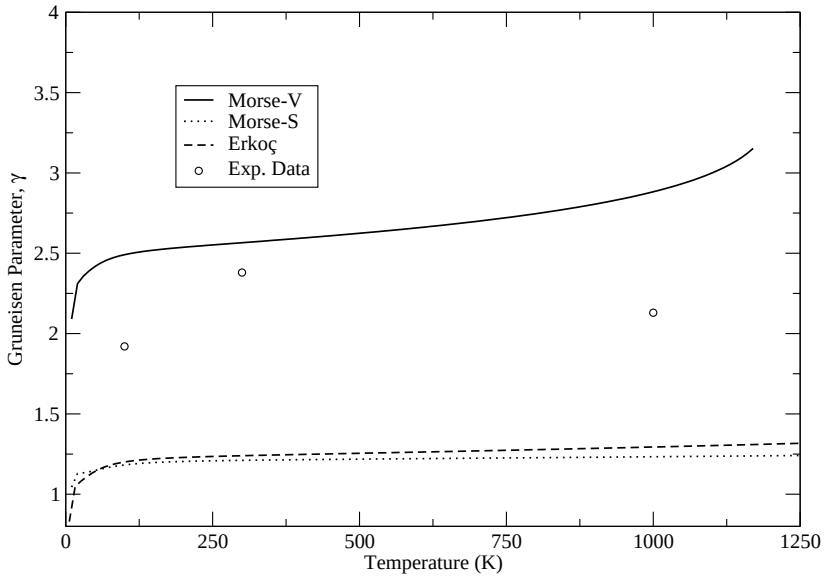

Figure 3.8: Grüneisen parameter for Cu as calculated using the Morse and Erkoç potentials. Experimental data taken from [14].

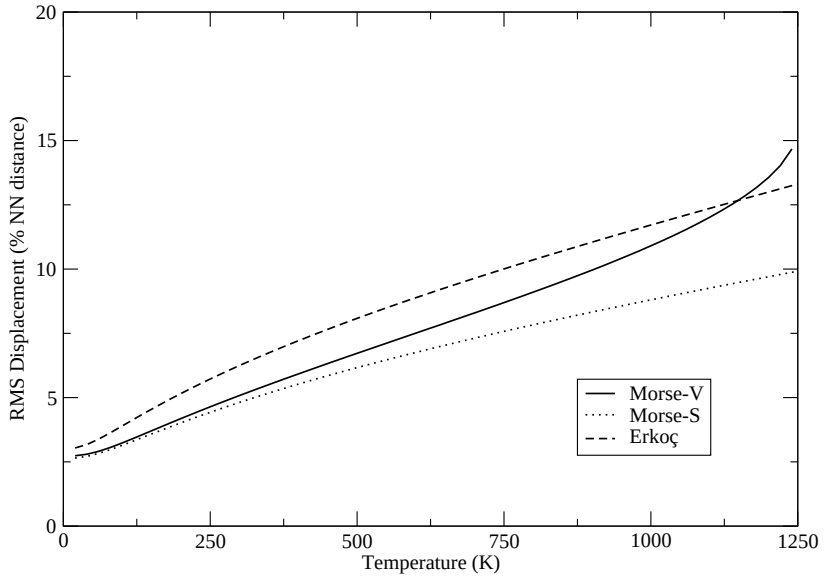

Figure 3.9: Atomic root-mean-square displacement for Cu as calculated using the Morse and Erkoç potentials.

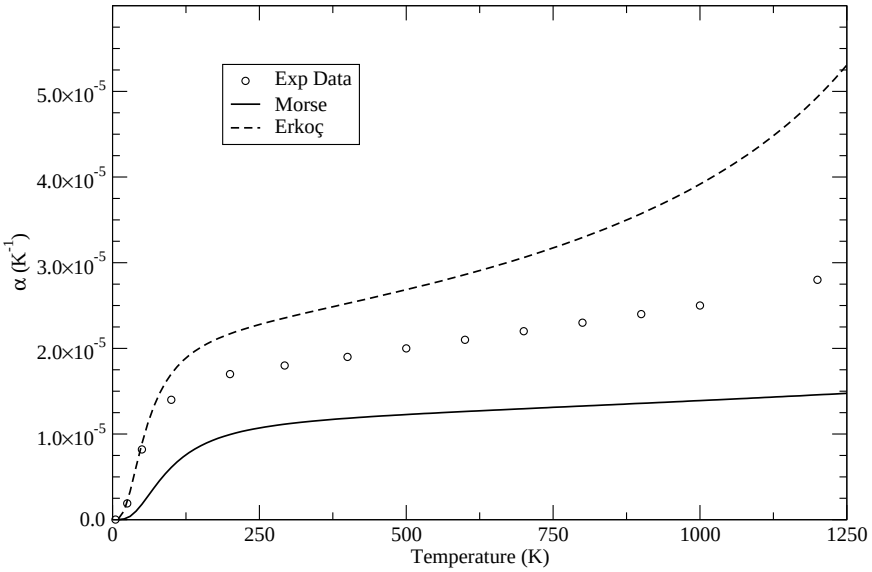

Figure 3.10: Thermal expansion coefficient for Ag as calculated using the Morse and Erkoç potentials. Experimental data taken from [9].

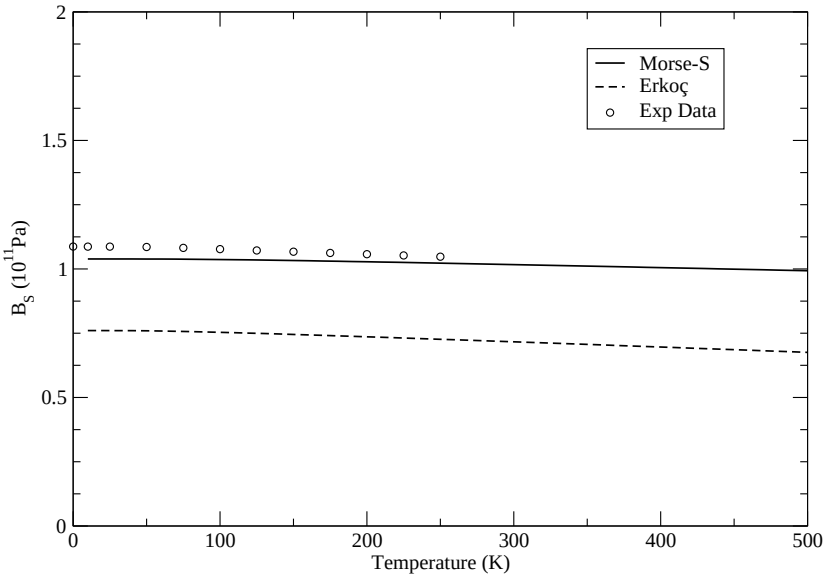

Figure 3.11: Adiabatic bulk modulus for Ag as calculated using the Morse and Erkoç potentials. Experimental data taken from [15].

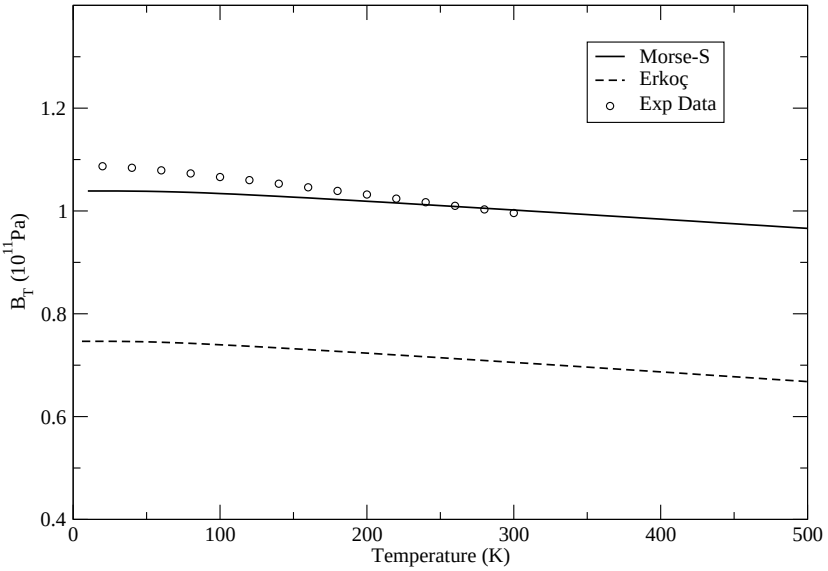

Figure 3.12: Isothermal bulk modulus for Ag as calculated using the Morse and Erkoç potentials. Experimental data taken from [11] and [12].

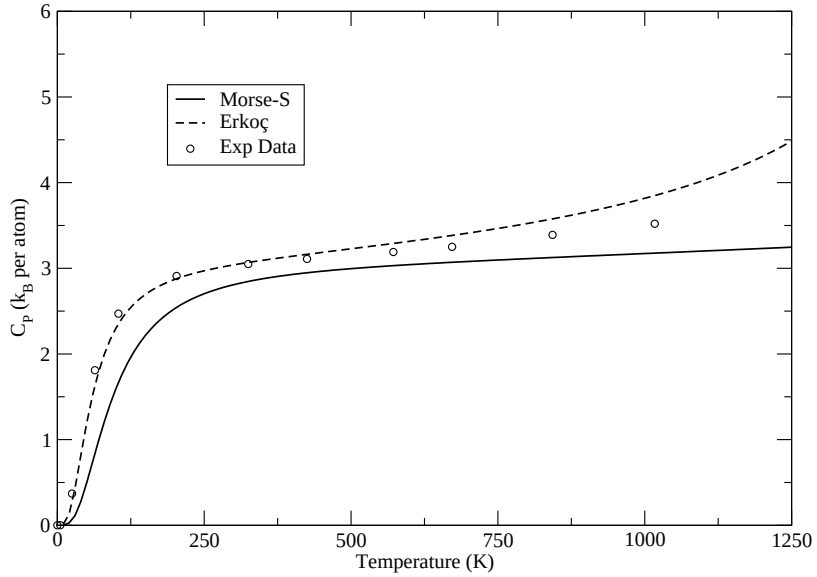

Figure 3.13: Specific heat at constant pressure for Ag as calculated using the Morse and Erkoç potentials. Experimental data taken from [13].

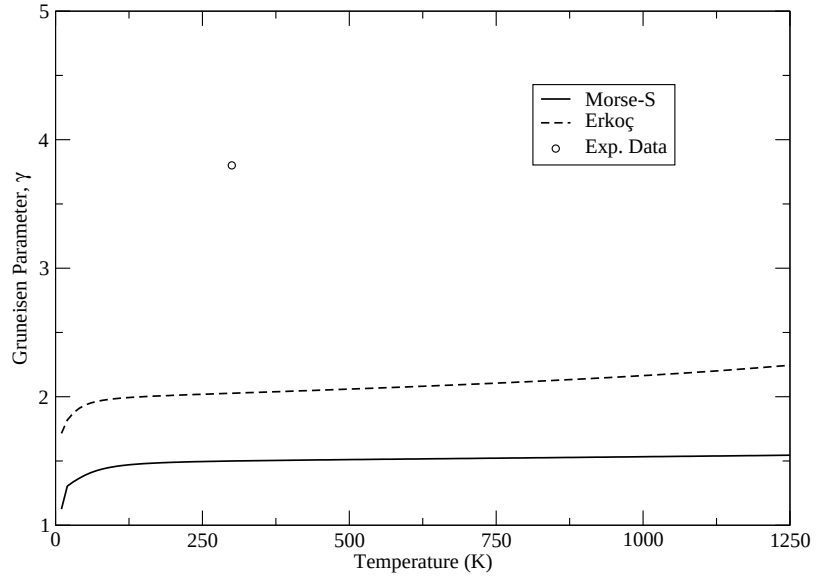

Figure 3.14: Grüneisen parameter for Ag as calculated using the Morse and Erkoç potentials. Experimental data taken from [14].

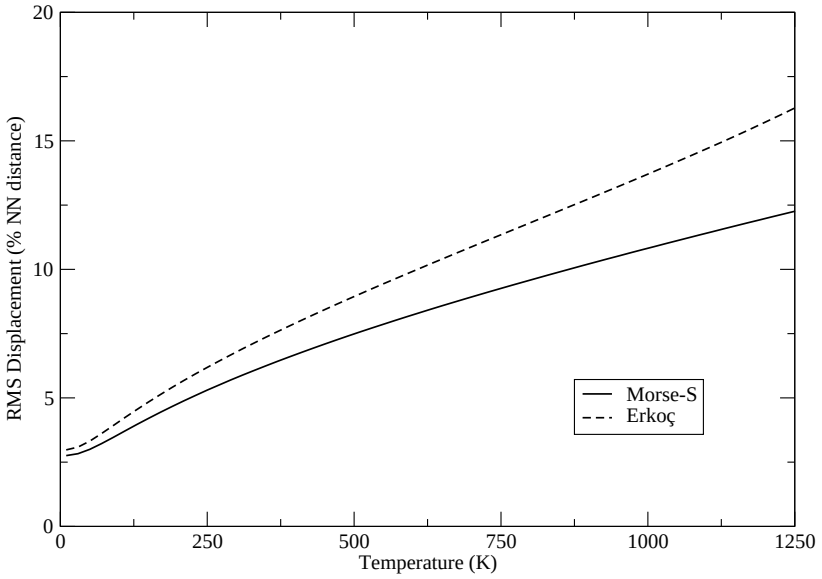

Figure 3.15: Atomic root-mean-square displacement for Ag as calculated using the Morse and Erkoç potentials.

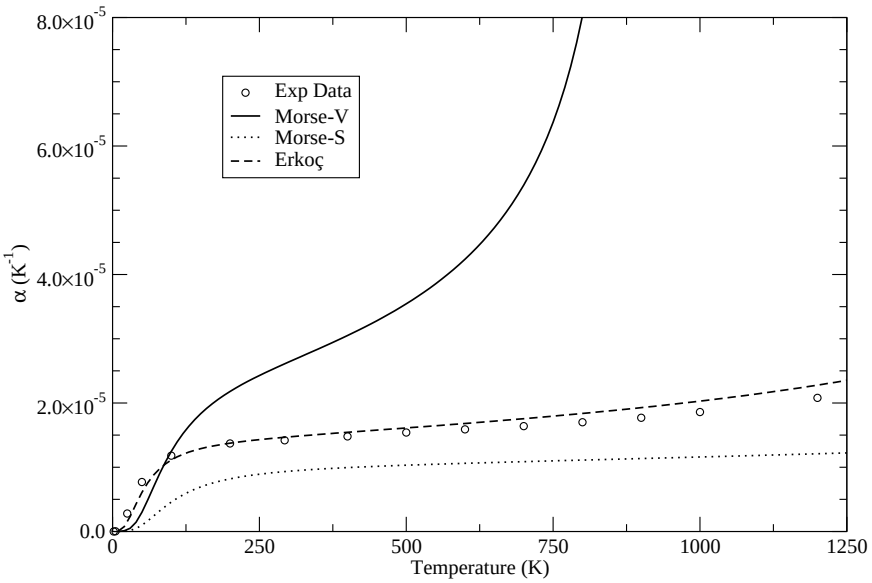

Figure 3.16: Thermal expansion coefficient for Au as calculated using the Morse and Erkoç potentials. Experimental data taken from [9].

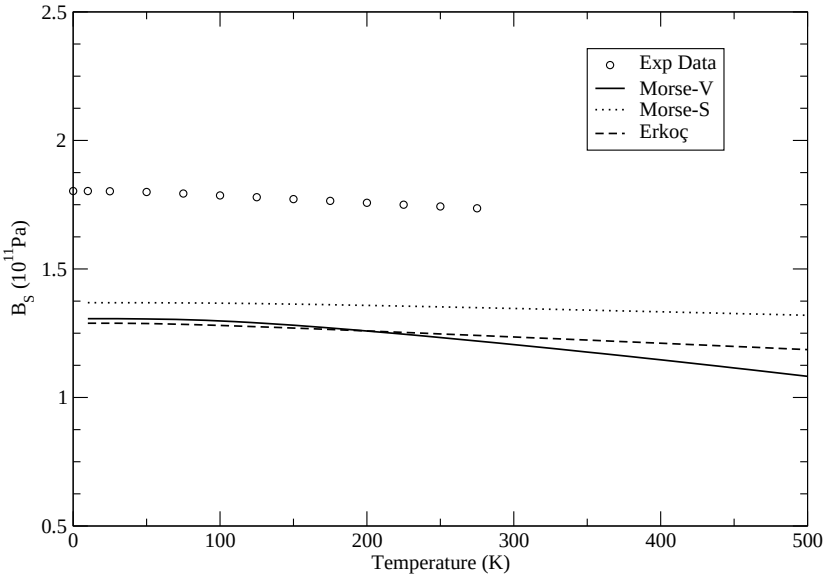

Figure 3.17: Adiabatic bulk modulus for Au as calculated using the Morse and Erkoç potentials. Experimental data taken from [15].

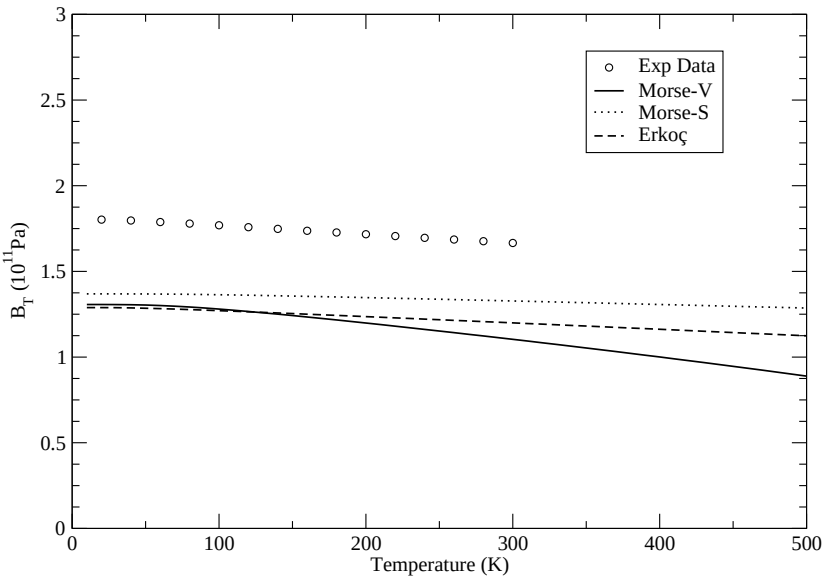

Figure 3.18: Isothermal bulk modulus for Au as calculated using the Morse and Erkoç potentials. Experimental data taken from [11] and [12].

As can be seen in the results, each potential has its strengths and weaknesses. The Erkoç potential performs very well for predicting the thermal expansion coefficients and heat capacities of all metals considered here. The Morse potential, however, better describes the bulk moduli in all cases. This can be explained by the way the two models were fitted to determine their parameters. The Erkoç potential was not fit to bulk properties at all; six of the eight parameters were fit to the potential curve of a dimer of each element while the remaining two parameters were determined by a many-body fitting to equilibrium lattice parameter and cohesive energy. This is the only way that many-body effects are captured in this potential. The Morse potential was fit directly to the experimentally determined compressibility of each metal, thereby immediately guaranteeing that the bulk modulus will be well represented also (since one is the reciprocal of the other). Evidently this sort of fitting fails to properly represent the thermal expansion coefficient. It seems that having more parameters does improve results overall, as evidenced by the superior performance of the Erkoç potential in most cases.

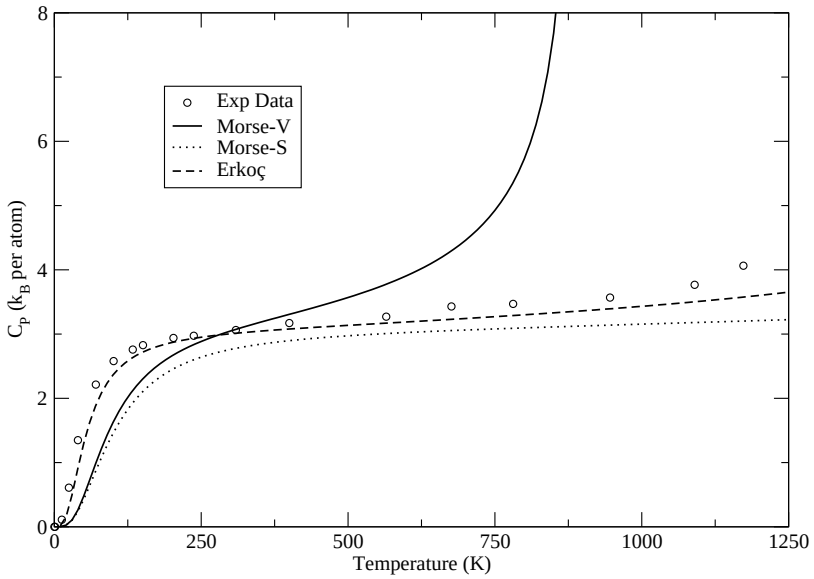

Figure 3.19: Specific heat at constant pressure for Au as calculated using the Morse and Erkoç potentials. Experimental data taken from [13].

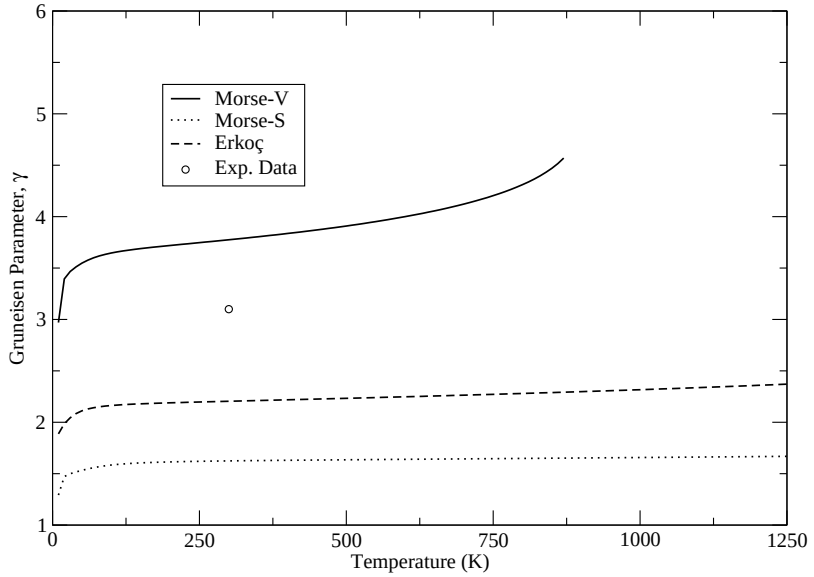

Figure 3.20: Grüneisen parameter for Au as calculated using the Morse and Erkoç potentials. Experimental data taken from [16].

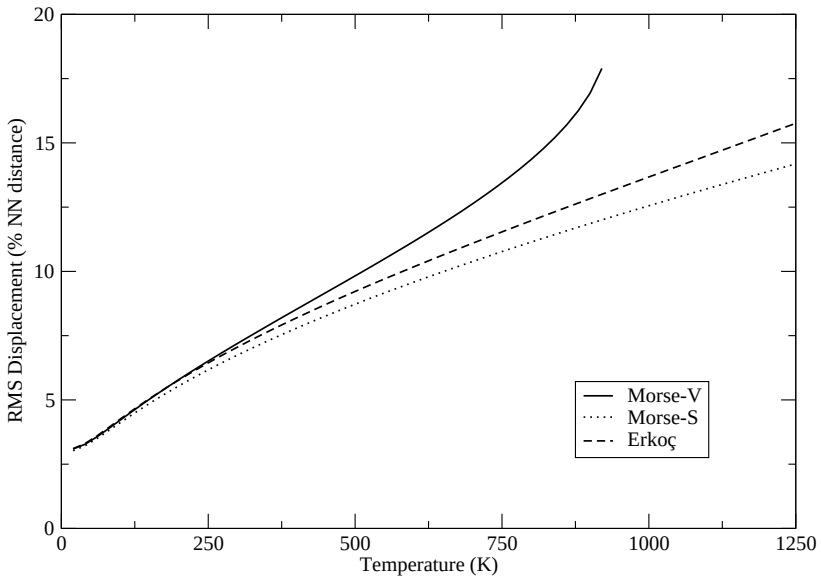

Figure 3.21: Atomic root-mean-square displacement for Au as calculated using the Morse and Erkoç potentials.

3.2 EAM Results

Sutton-Chen and Quantum Sutton-Chen

Results for the Sutton-Chen and Quantum Sutton-Chen are plotted in Figs. 3.22 to 3.49. The Sutton-Chen potential results are denoted by SC and the Quantum Sutton-Chen results are denoted by Q-SC. As was done by Kimura *et al.*, the interaction range is taken to include eight neighbour shells (a distance of two lattice parameters).

The predicted phonon dispersion curves for the Sutton-Chen and Quantum Sutton-Chen potentials are given in Figs. 3.22 to 3.25. The SC potential does not predict the phonon frequencies very well in the symmetry directions shown here. For Cu, values are 16% too low at the X-point in the [100] longitudinal branch. They are 7% too high for Ag, 35% too low for Au and 32% too low for Pt. The QSC improves on these results quite dramatically: the longitudinal branch in the [100] direction is 3.7% too low for Cu, 4% for Ag, 23% for Au and 11% for Pt. Compared with the pair-potential results, the QSC performs slightly better for Cu and Ag. The situation for Au is different since there are large discrepancies between calculations and exper-

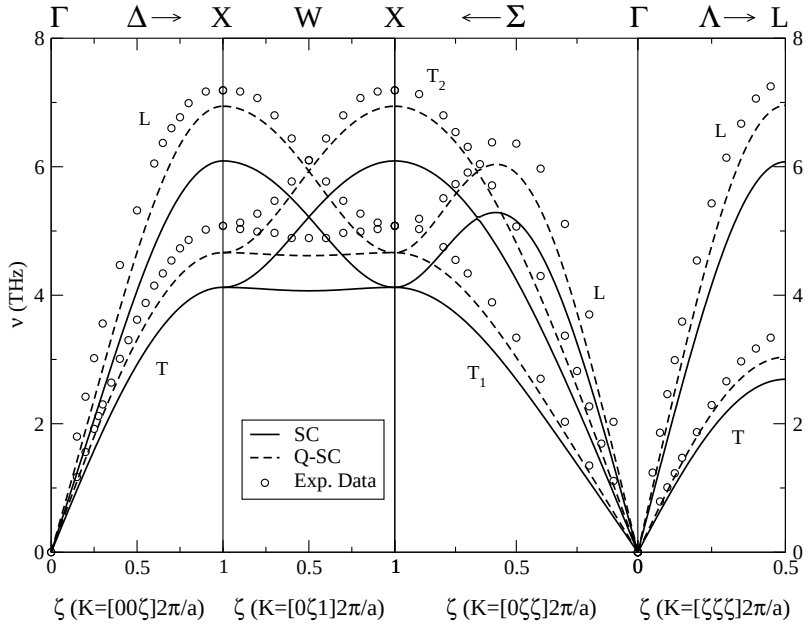

Figure 3.22: Phonon dispersion curves for Cu as calculated using the Sutton-Chen and Quantum Sutton-Chen potentials. Experimental data taken from [6].

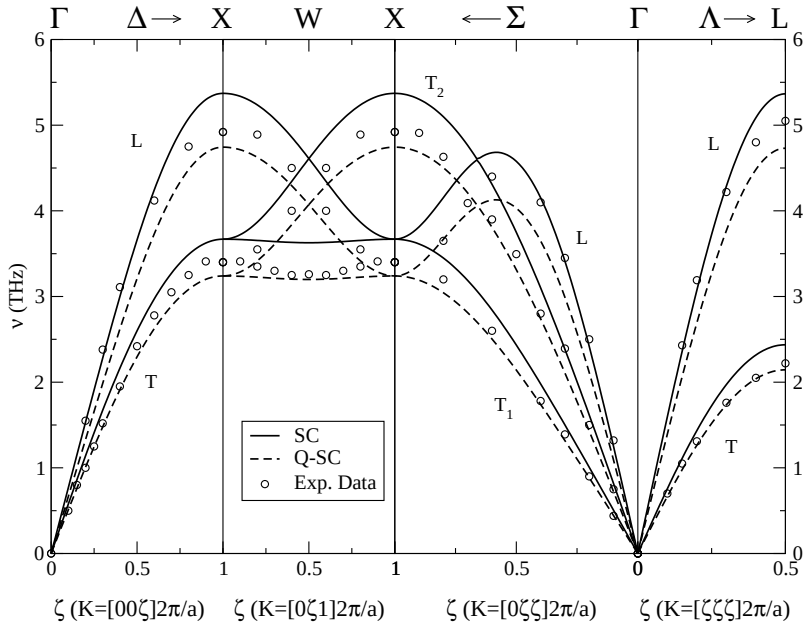

Figure 3.23: Phonon dispersion curves for Ag as calculated using the Sutton-Chen and Quantum Sutton-Chen potentials. Experimental data taken from [7].

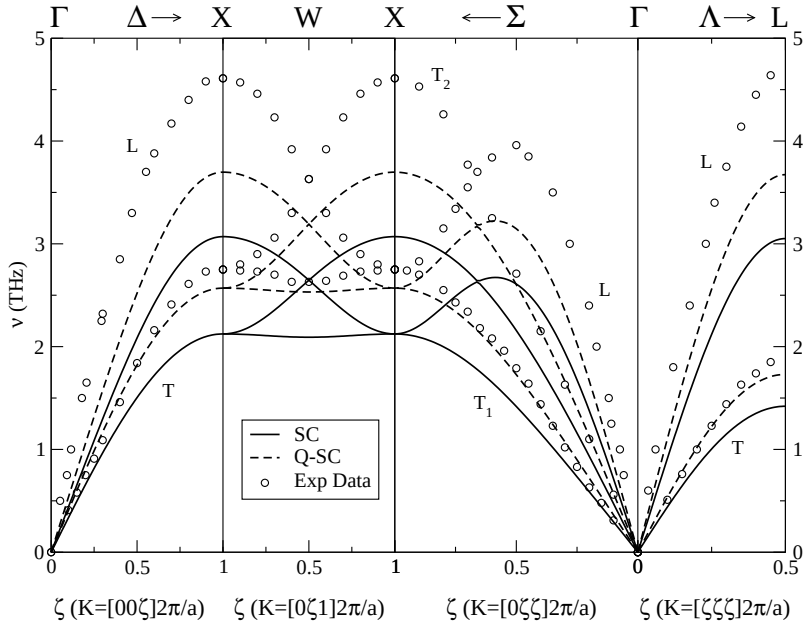

Figure 3.24: Phonon dispersion curves for Au as calculated using the Sutton-Chen and Quantum Sutton-Chen potentials. Experimental data taken from [8].

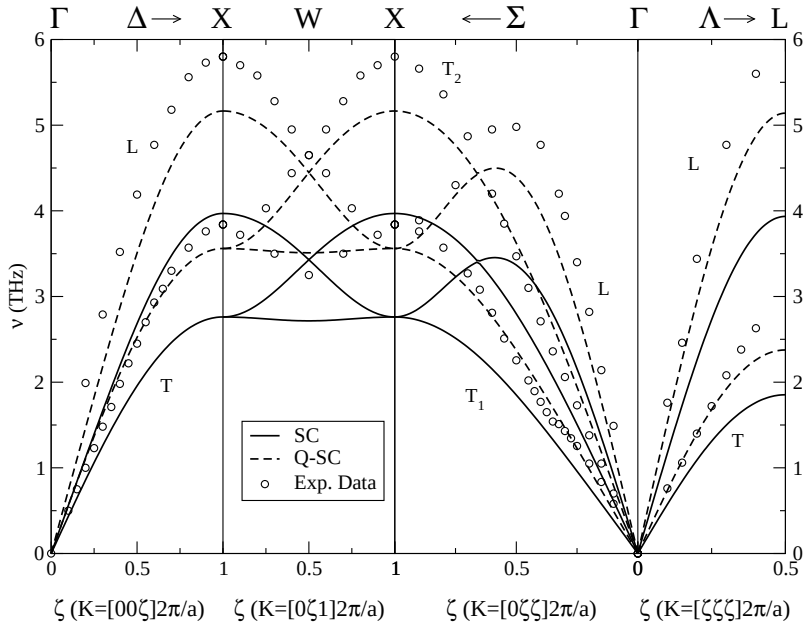

Figure 3.25: Phonon dispersion curves for Pt as calculated using the Sutton-Chen and Quantum Sutton-Chen potentials. Experimental data taken from [8].

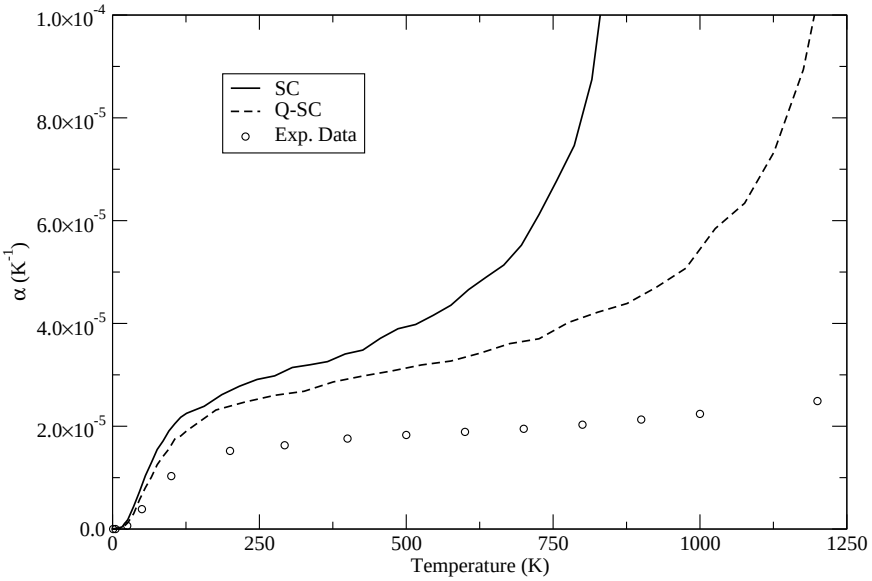

Figure 3.26: Thermal expansion coefficient for Cu as calculated using the Sutton-Chen and Quantum Sutton-Chen potentials. Experimental data taken from [9].

iment for different branches. The Morse-V potential fares better for the longitudinal [100] branch while the many-body QSC performs better on the transverse branch in the same direction.

The Quantum Sutton-Chen potential shows marked improvement over the Sutton-Chen in all properties studied here for all metals except Ag. The thermal expansion coefficient is still overestimated in both cases, however. The predicted melting point of Cu ranges from 550K to 700K for the Sutton-Chen potential and 700K to 800K for the Quantum Sutton-Chen potential. Neither of these agrees with the actual value of 1358K.

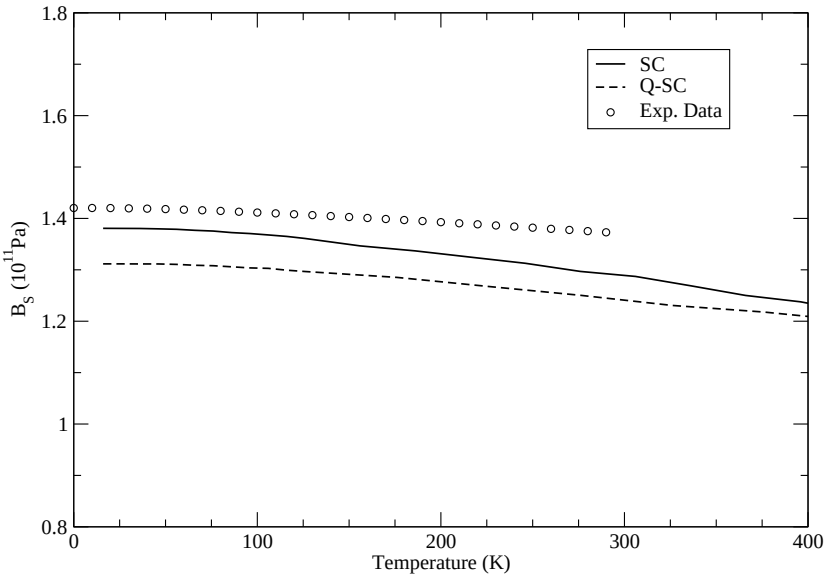

Figure 3.27: Adiabatic bulk modulus for Cu as calculated using the Sutton-Chen and Quantum Sutton-Chen potentials. Experimental data taken from [10].

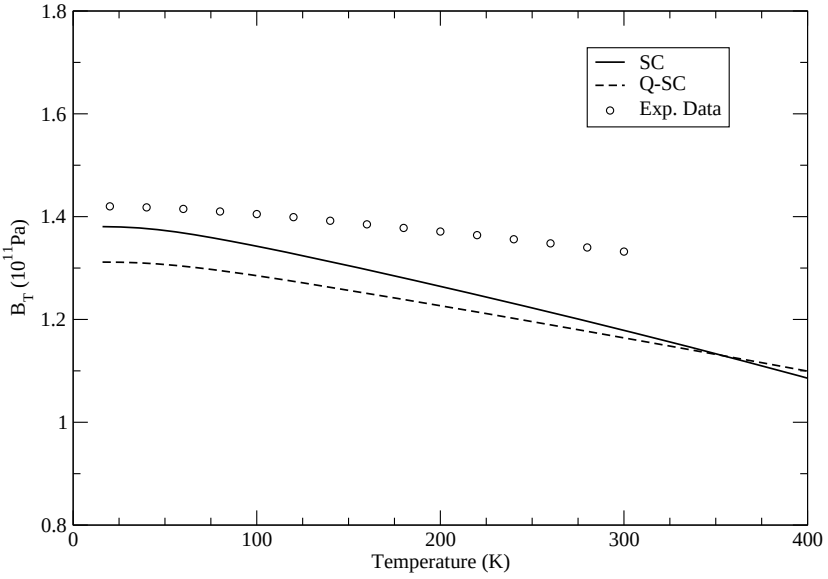

Figure 3.28: Isothermal bulk modulus for Cu as calculated using the Sutton-Chen and Quantum Sutton-Chen potentials. Experimental data taken from [11] and [12].

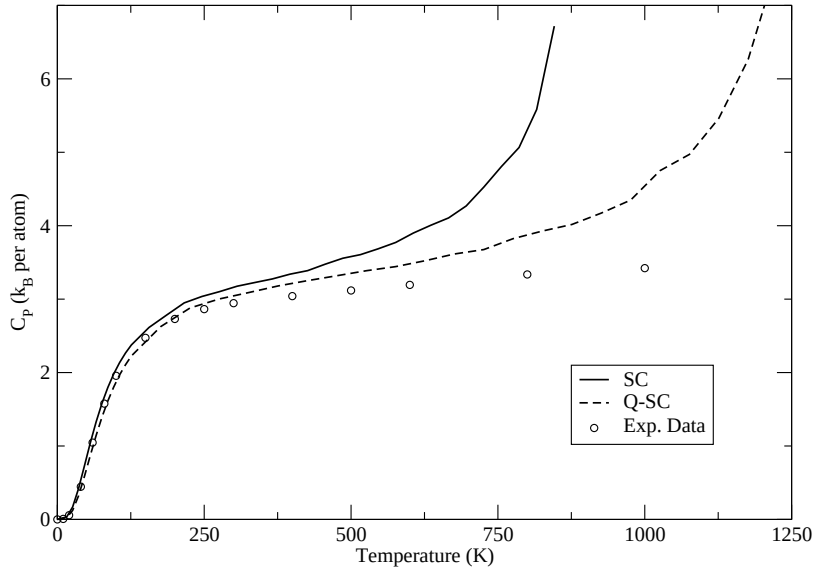

Figure 3.29: Specific heat at constant pressure for Cu as calculated using the Sutton-Chen and Quantum Sutton-Chen potentials. Experimental data taken from [13].

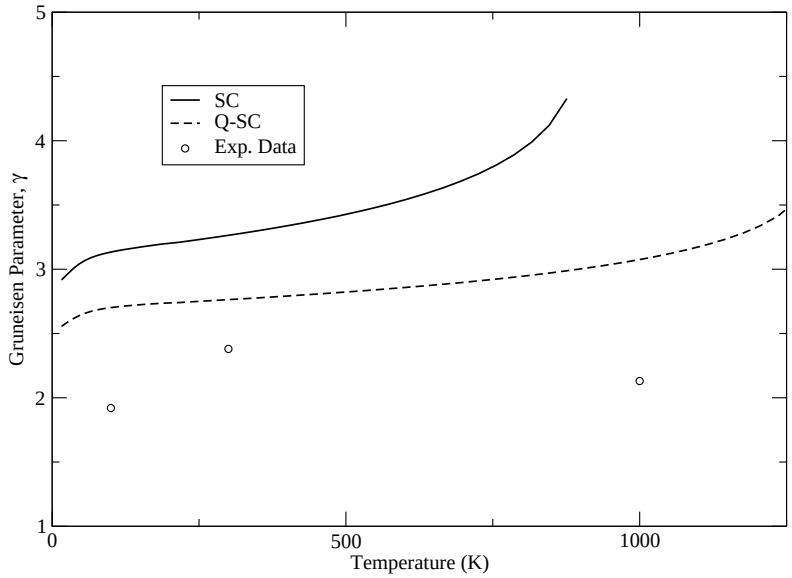

Figure 3.30: Grüneisen parameter for Cu as calculated using the Sutton-Chen and Quantum Sutton-Chen potentials. Experimental data taken from [14].

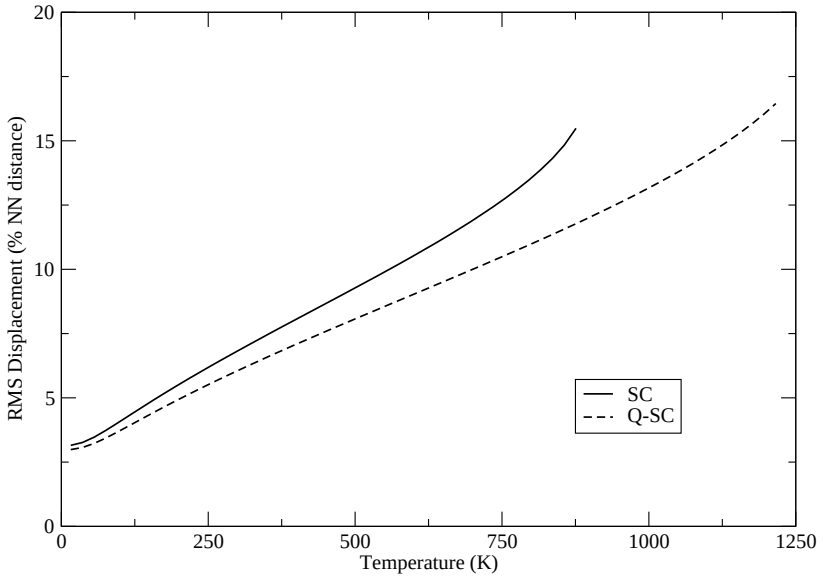

Figure 3.31: Atomic root-mean-square displacement for Cu as calculated using the Sutton-Chen and Quantum Sutton-Chen potentials.

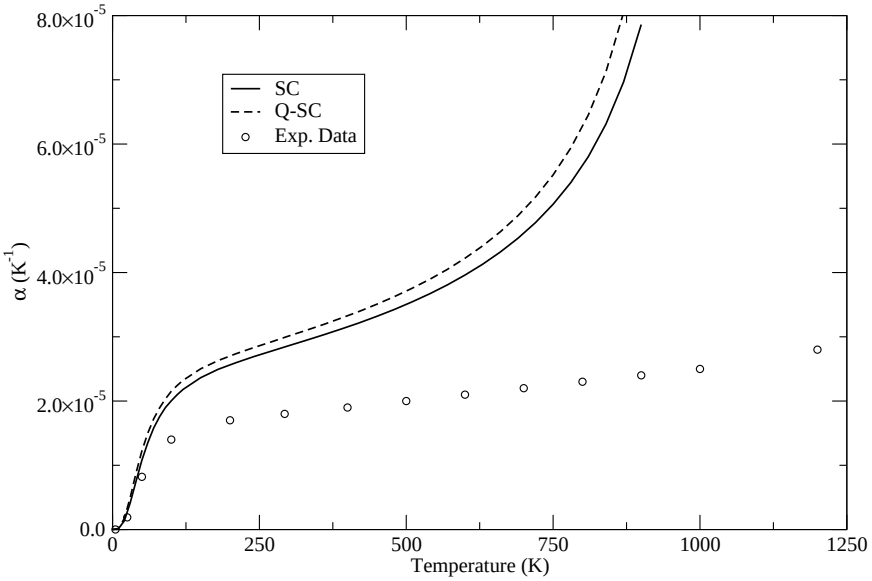

Figure 3.32: Thermal expansion coefficient for Ag as calculated using the Sutton-Chen and Quantum Sutton-Chen potentials. Experimental data taken from [9].

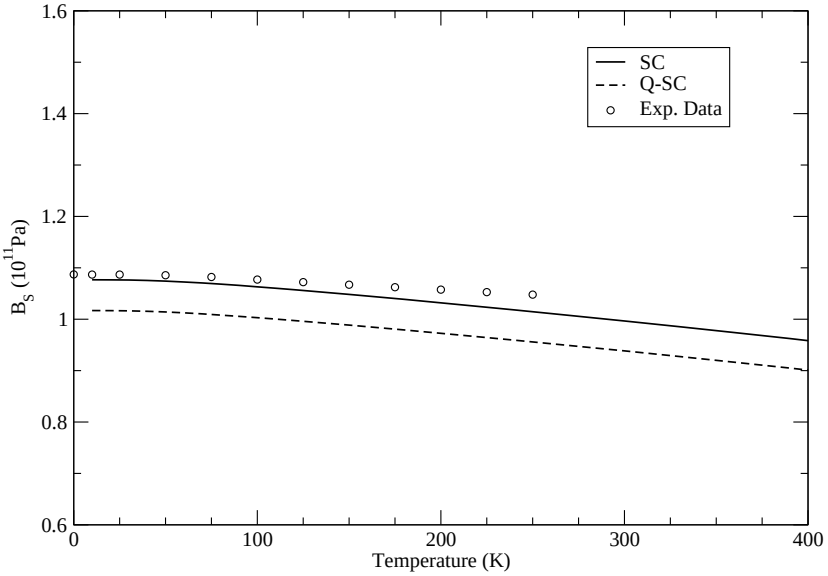

Figure 3.33: Adiabatic bulk modulus for Ag as calculated using the Sutton-Chen and Quantum Sutton-Chen potentials. Experimental data taken from [15].

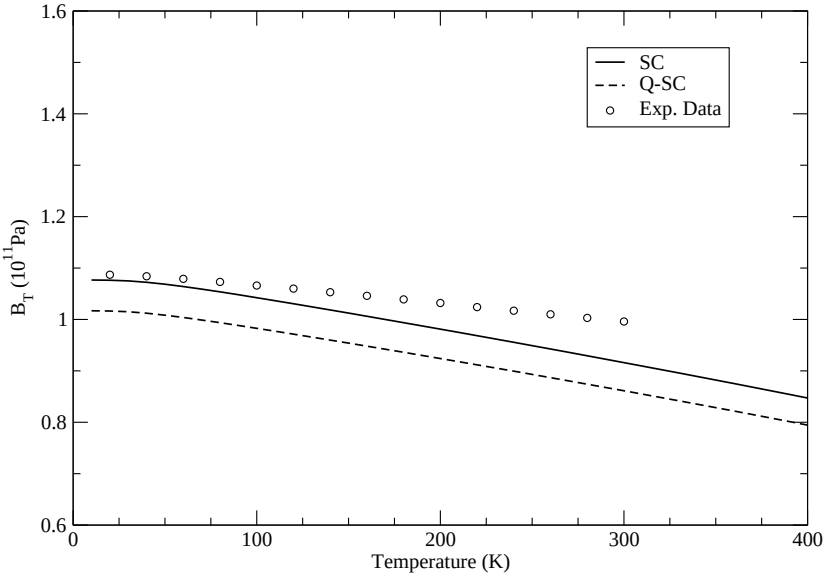

Figure 3.34: Isothermal bulk modulus for Ag as calculated using the Sutton-Chen and Quantum Sutton-Chen potentials. Experimental data taken from [11] and [12].

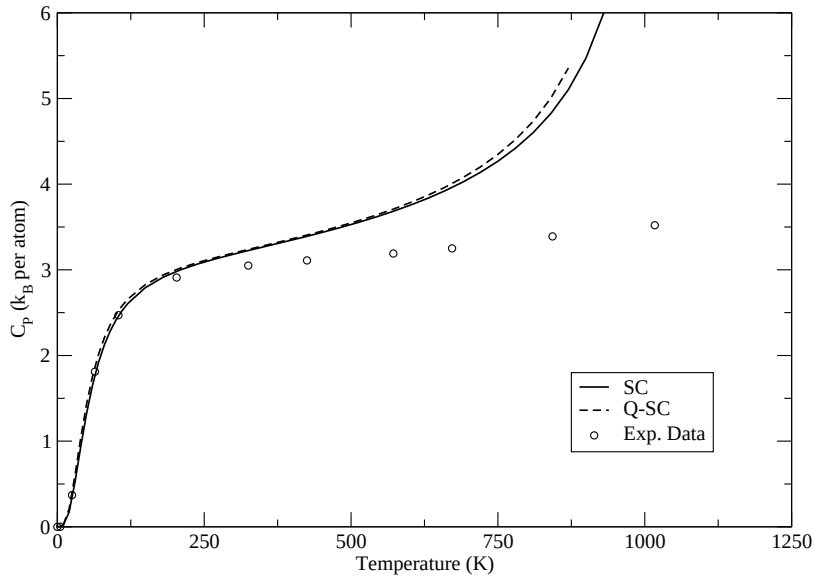

Figure 3.35: Specific heat at constant pressure for Ag as calculated using the Sutton-Chen and Quantum Sutton-Chen potentials. Experimental data taken from [13].

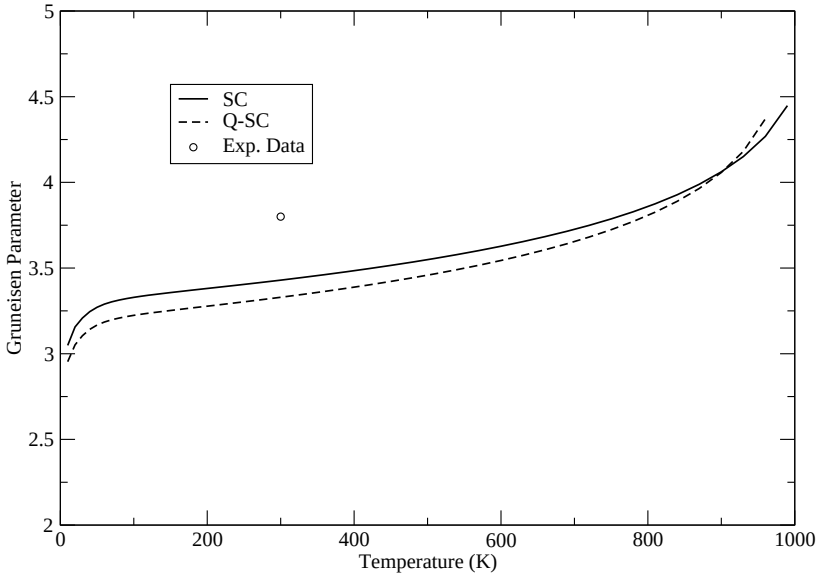

Figure 3.36: Grüneisen parameter for Ag as calculated using the Sutton-Chen and Quantum Sutton-Chen potentials. Experimental data taken from [14].

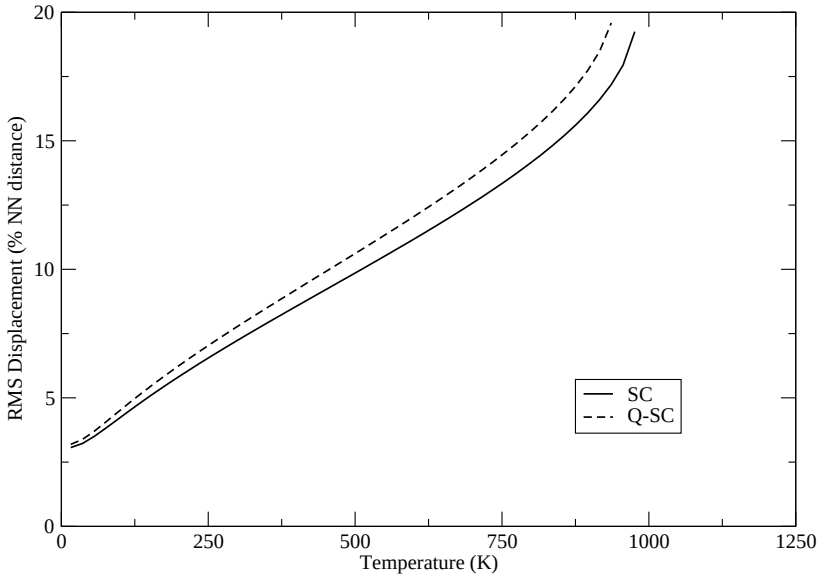

Figure 3.37: Atomic root-mean-square displacement for Ag as calculated using the Sutton-Chen and Quantum Sutton-Chen potentials.

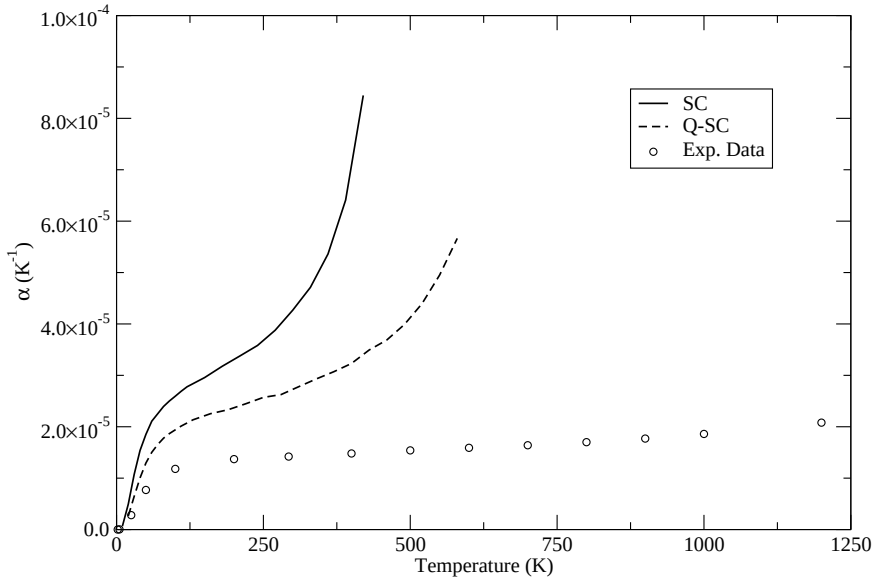

Figure 3.38: Thermal expansion coefficient for Au as calculated using the Sutton-Chen and Quantum Sutton-Chen potentials. Experimental data taken from [9].

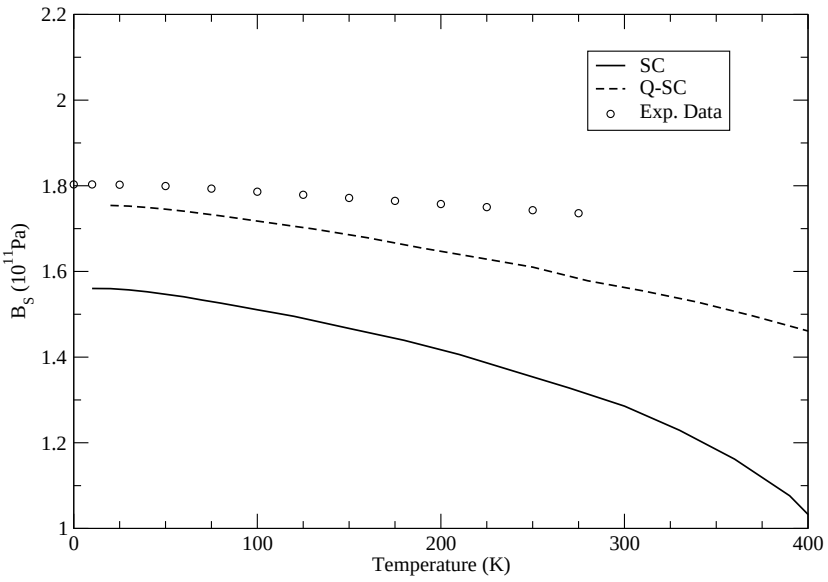

Figure 3.39: Adiabatic bulk modulus for Au as calculated using the Sutton-Chen and Quantum Sutton-Chen potentials. Experimental data taken from [15].

Au was seen to be a particularly difficult element to properly predict and the situation is unchanged with these potentials. The thermal expansion coefficient is largely overestimated, about 3 times larger than experiment for the SC and nearly twice as large for Q-SC potential at 300K. The adiabatic bulk modulus is 25% too low for the SC and 10% too low for the Q-SC case.

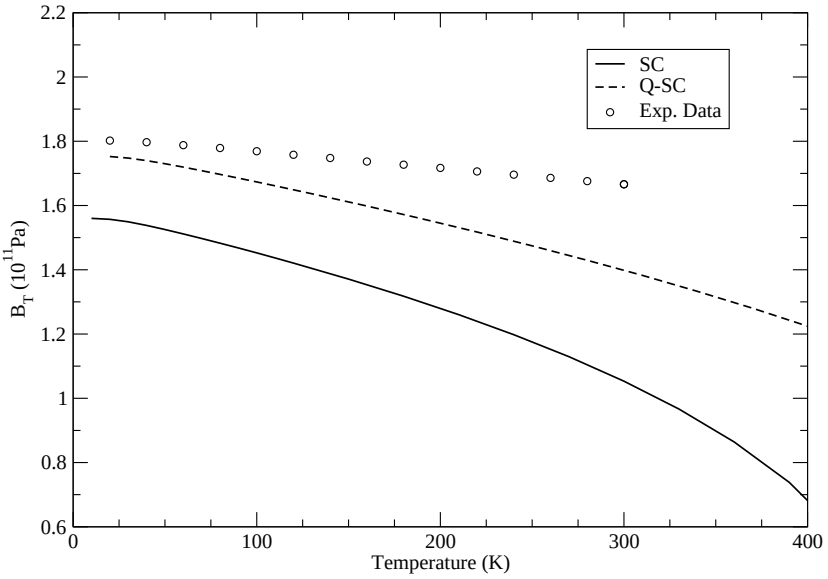

Figure 3.40: Isothermal bulk modulus for Au as calculated using the Sutton-Chen and Quantum Sutton-Chen potentials. Experimental data taken from [11] and [12].

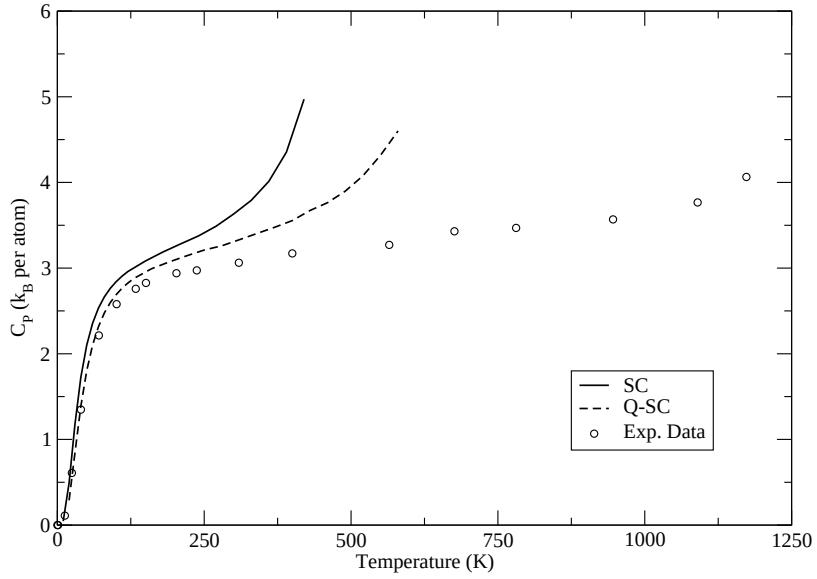

Figure 3.41: Specific heat at constant pressure for Au as calculated using the Sutton-Chen and Quantum Sutton-Chen potentials. Experimental data taken from [13].

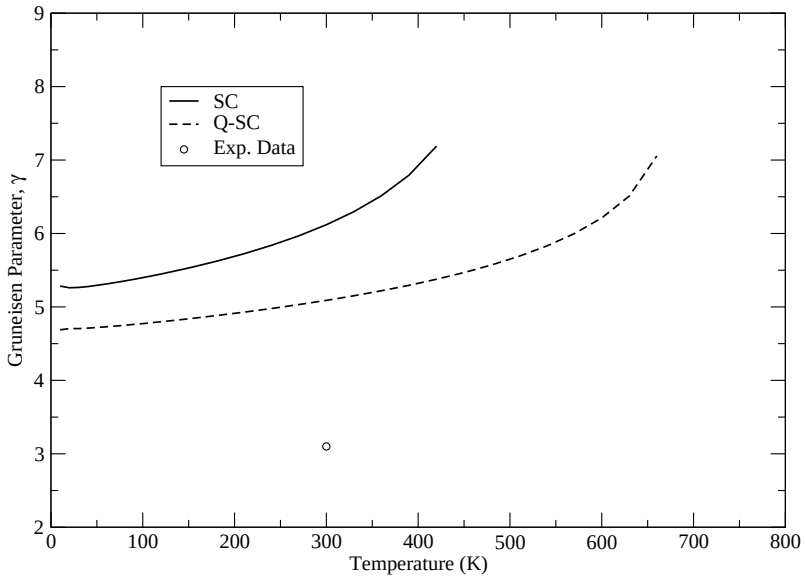

Figure 3.42: Grüneisen parameter for Au as calculated using the Sutton-Chen and Quantum Sutton-Chen potentials. Experimental data taken from [16].

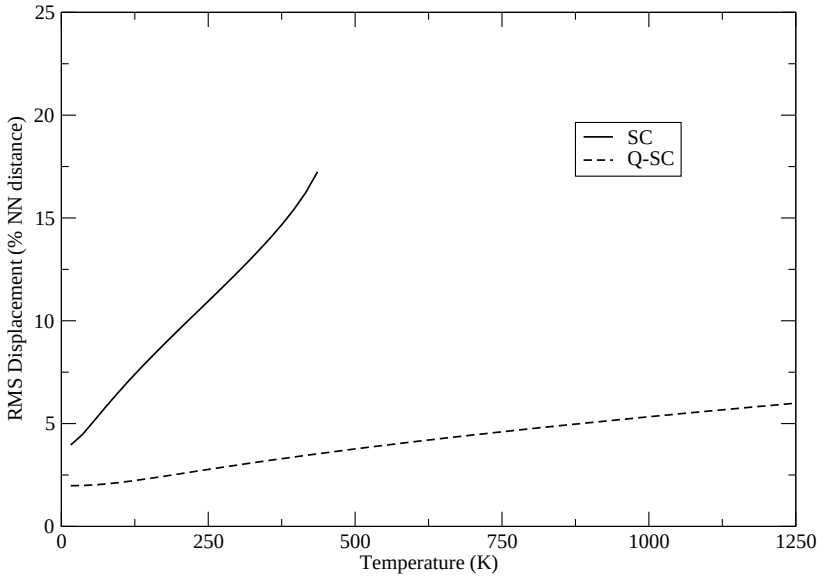

Figure 3.43: Atomic root-mean-square displacement for Au as calculated using the Sutton-Chen and Quantum Sutton-Chen potentials.

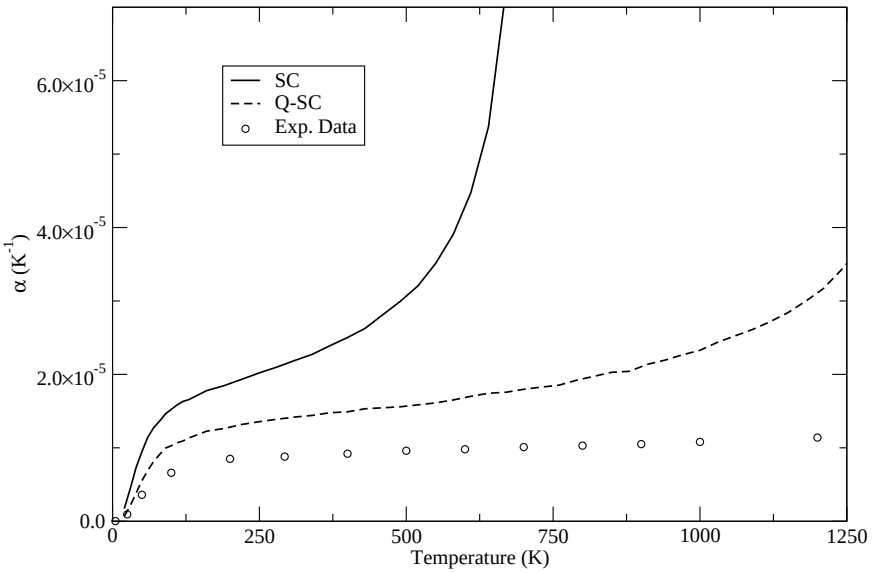

Figure 3.44: Thermal expansion coefficient for Pt as calculated using the Sutton-Chen and Quantum Sutton-Chen potentials. Experimental data taken from [9].

Since Pt is not in the same group as the other three studied in this work, it can give further insight into these potentials. Here the Q-SC shows a dramatic improvement over the SC potential in all areas except isothermal bulk modulus where it is difficult to decide the superior result. Specific heat is particularly well described by the Q-SC. A trend can be identified here where the thermal expansion coefficient is much too high with these potentials. C_P is also seen to diverge at higher temperatures in a similar manner for the unmodified SC potential.

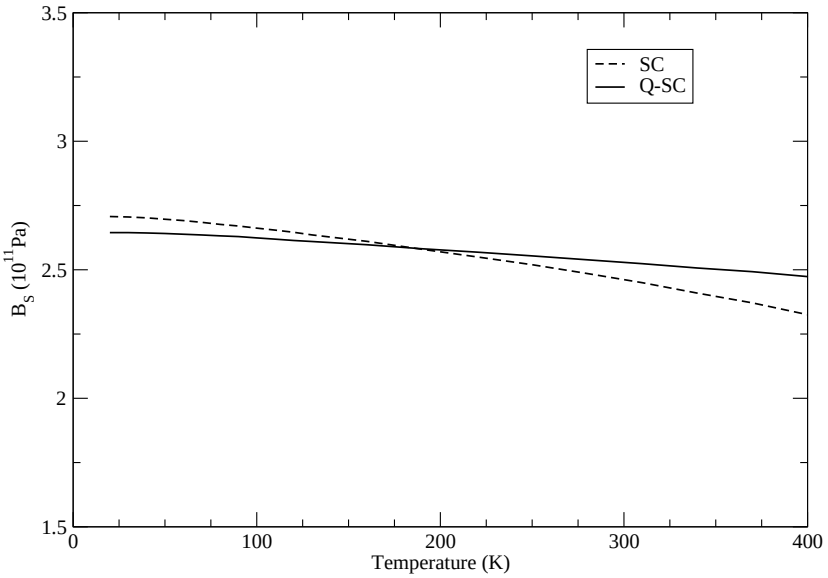

Figure 3.45: Adiabatic bulk modulus for Pt as calculated using the Sutton-Chen and Quantum Sutton-Chen potentials. Experimental data taken from [15].

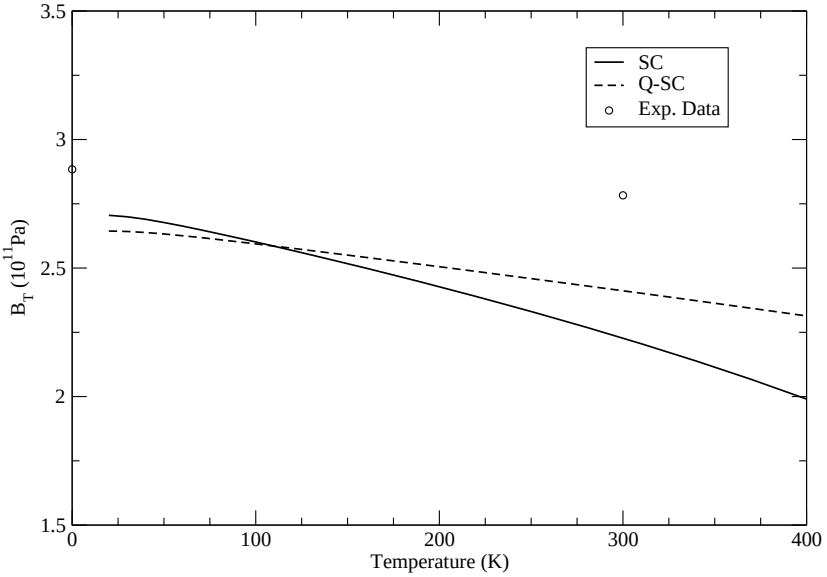

Figure 3.46: Isothermal bulk modulus for Pt as calculated using the Sutton-Chen and Quantum Sutton-Chen potentials. Experimental data taken from [11] and [12].

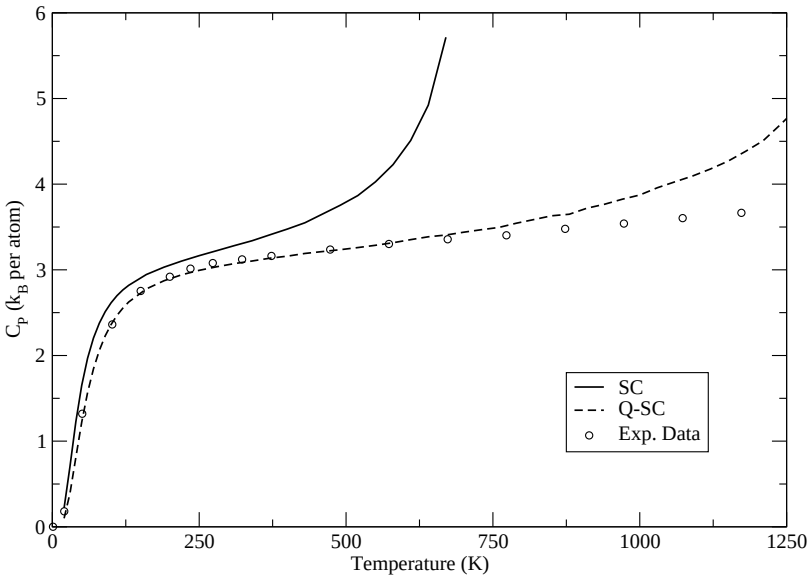

Figure 3.47: Specific heat at constant pressure for Pt as calculated using the Sutton-Chen and Quantum Sutton-Chen potentials. Experimental data taken from [13].

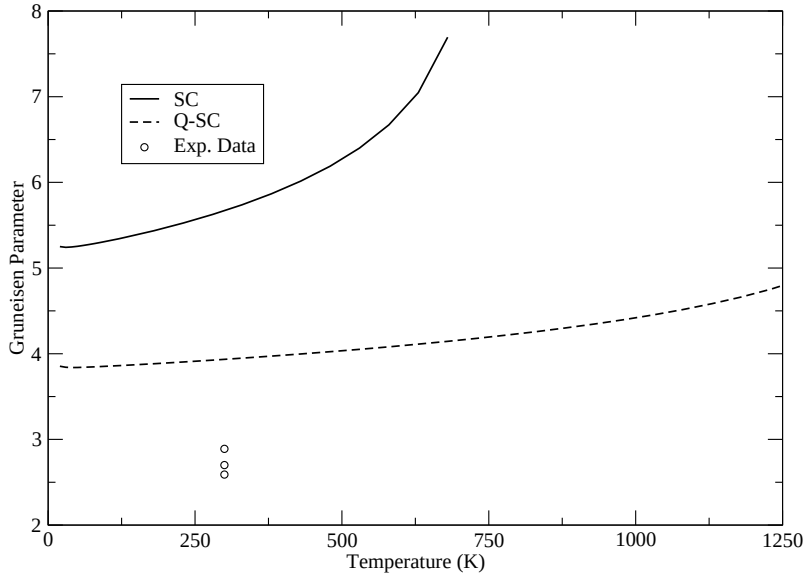

Figure 3.48: Grüneisen parameter for Pt as calculated using the Sutton-Chen and Quantum Sutton-Chen potentials. Experimental data taken from [16].

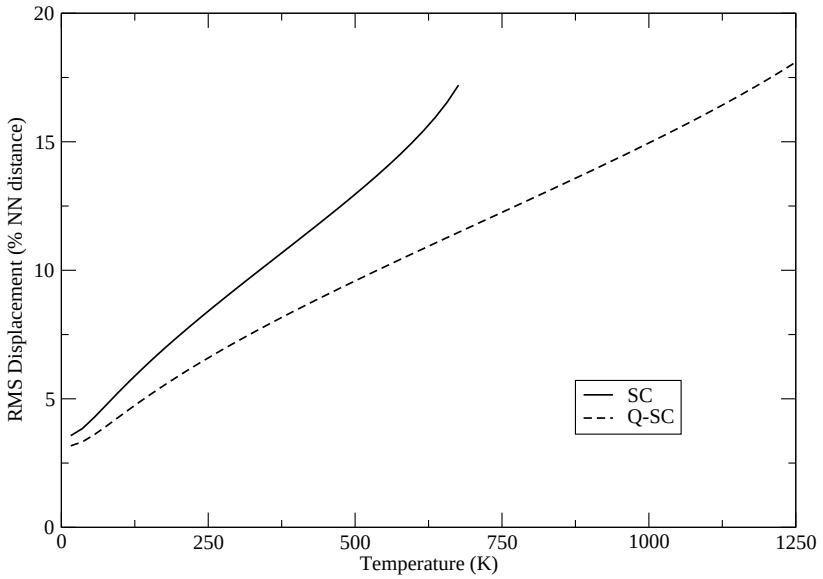

Figure 3.49: Atomic root-mean-square displacement for Pt as calculated using the Sutton-Chen and Quantum Sutton-Chen potentials.

Chapter 4

Modified Sutton-Chen Potential

4.1 Motivation

From the results of the previous section it can be seen that there is an inherent instability in the Sutton-Chen (SC) potential at high temperatures. The results for thermal expansion are overestimated which in turn causes the same for the heat capacity. Both isothermal and adiabatic bulk moduli are underestimated. One must then conclude that the potential predicts the metals to soften more rapidly than is experimentally observed. This comes from a decrease in the phonon frequencies with temperature at an overestimated rate.

The Quantum Sutton-Chen (QSC) potential does improve the situation quite dramatically; in nearly all cases, the results are a closer fit to the experimental values. Including quantum effects meant the calculations must also account for the zero-point energy, which is a small contribution to the free energy and appears as follows at 0K [5]:

$$F_0 = U_{tot} + \sum_{\mathbf{k},s} \frac{1}{2}\hbar\omega_s(\mathbf{k}) \tag{4.1.1}$$

For temperatures above 0K, the free energy regains the vibrational term present in Eq. 2.2.20. Neglecting these small corrections to the potential, the QSC is essentially

a re-parametrized version of the original SC potential. While the results are improved, there is still evidence of instability at higher temperatures in the form of the diverging thermal expansion coefficient. The re-parametrization has shifted the divergence further up in the temperature range, but it is still present. This supports the idea that there is a fundamental issue with this potential that cannot be resolved by simply changing the parameters.

T. Çağin *et al.* [46] have done some molecular dynamics simulations using the SC potential and found results that agree with those found in this work, namely that the thermal expansion is overestimated. The conclusion they drew is that it must be a parametrization issue that causes the results to disagree [46]. Since there is essentially an alternate parametrization scheme provided by [5], we may decide if this is indeed the case. Again, the results are improved with the alternate parameters but the issues with the potential are not resolved. The thermal expansion coefficient is still predicted to be significantly larger than is experimentally measured and the high-temperature divergence still exists. In the case of Ag, the new parametrization scheme actually worsens the situation. It is therefore our conclusion that it is the form of the potential that is at the root of this issue rather than the specific choice of parameters.

4.2 Derivation

Based on theoretical arguments with support from the results of Cleri & Rosato and Dai *et al.* that will be discussed in the next chapter, we believe that an exponential decay of the electron density would provide a more physically realistic picture of metals and hence also a better fit to experimental results. In order to make the most meaningful comparison to the original SC potential, the number of parameters is kept the same and only the density function is altered. Of course, the square-root form of

the density function is unchanged as well. The new function has the form

$$\rho_i = \sum_{j \neq i} e^{-\alpha(r_{ij}/a - 1)} \tag{4.2.1}$$

where α is an adjustable parameter and a is the same length scaling unit used in the repulsive term (chosen to be the lattice parameter at room temperature). The full potential is then

$$U(r_{ij}) = \epsilon \left[\sum_{j \neq i} \left(\frac{a}{r_{ij}} \right)^n - c \left(\sum_{j \neq i} e^{-\alpha(r_{ij}/a - 1)} \right)^{1/2} \right] \tag{4.2.2}$$

where ϵ, c, n and α are adjustable parameters. Inclusion of the factor of e^{α} in the density function is simply a choice of convenience as this resulted in values for c that were closer to those used in the QSC model. Since now there is only one exponent (n), the restriction that it must be an integer is lifted. Initially this restriction was imposed to allow the parameters to be transferred from one metal to another by changing ϵ and a, provided the crystal structure and the exponents n and m were the same for both metals. Because there is no physical reason for this restriction, we decide to work without it. Also due to the change of ρ_i, the density function can no longer be expressed as a convenient summation as it appears in Eq. 1.2.12.

It is worth noting that Mei and Davenport used a polynomial fit for the density function in an attempt to produce an overall exponential decay. This was motivated by Hartree-Fock calculations [27] that have shown the electron density to be well approximated by the function

$$\rho = \rho_e e^{-\beta(r_1/r_{1e} - 1)} \tag{4.2.3}$$

when r_1 is not far from r_{1e}, the equilibrium nearest-neighbour distance. This issue here is that this is an overall charge density, so that the individual charge densities cannot be expressed in such a form for any neighbour sum beyond the first. A sum of exponential functions cannot be expressed as a single exponential function. The

solution Mei and Davenport proposed was to use a polynomial fit:

$$\sum_m s_m f(r_m) = \rho_e e^{-\beta(r_1/r_{1e}-1)} \tag{4.2.4}$$

where $f(r)$ is chosen to be a parametrized function that satisfies Eq. 4.2.4. It was chosen to be a power-law type polynomial of the form

$$f(r) = f_e \sum_{l=0}^{k} c_l \left(\frac{r_{1e}}{r}\right)^l \tag{4.2.5}$$

where f_e and c_l are constants. With this form a sum over k neighbour shells would appear as an overall exponential decay. Such a decay is desirable because as can be seen in Fig. 4.1, the charge density decay of Cu as calculated using Density Functional Theory (DFT) can be fit very well by an exponential function. A power-law decay function is also fit to the same curve for comparison. It is evident that the exponential function is a closer fit to the data than the power-law function, suggesting this is a more physically accurate description.

Even the parametrized polynomial fit of Mei and Davenport, Eq. 4.2.5, can be very well represented by a single exponential function. A comparison of the two is shown in Fig. 4.2. Also included in the plot is a function of the same form as that used by Sutton and Chen for comparison. The exponential function is quite close to the function used by Mei and Davenport while the power-law decay of Sutton and Chen shows a noticeable deviation in its curvature. This was further motivation for choosing the simple exponential decay for the modified model.

What we have, then, is a Modified Sutton-Chen (MSC) potential that retains the same essential characteristics: four parameters, simple mathematical form and the square-root density function. In order to determine appropriate values for the four parameters, a damped least-squares fitting was done using the Levenberg-Marquardt algorithm [47]. Four properties were chosen for the fitting: cohesive energy, equilibrium lattice parameter, isothermal bulk modulus and elastic constant C_{11}. The

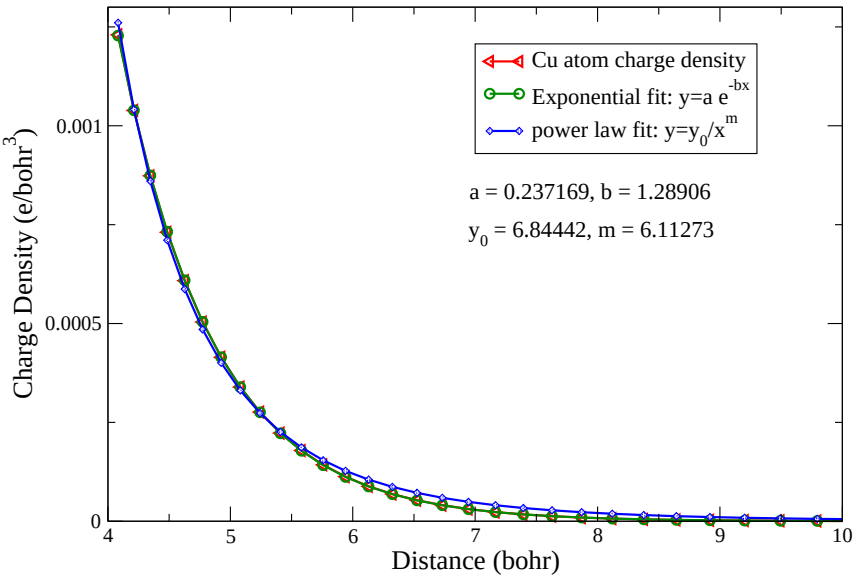

Figure 4.1: Charge density as a function of distance in Cu. Power-law and exponential functions are fit to the charge density decay with distance as predicted by Density Functional Theory. DFT calculations taken from [17].

fitting was done at 300K so that room-temperature values for these properties were used and the interaction range was extended up to sixth-nearest neighbours. It was found that going beyond the sixth neighbour shell yielded only very small changes to the results at the cost of greatly increased computing time (primarily due to the three-body interactions present in Eq. 2.1.30).

It is, of course, possible to have multiple sets of parameters that satisfy the conditions at 300K. In this event, parameters that gave best results at higher temperatures were selected. The parameters for the MSC potential are given in Table 4.1. It should be noted, however, that for the case of Au only three of the four properties were fitted (bulk modulus was not fitted exactly). The reason for this is simply that the fitting algorithm could not converge on a set of values for the parameters that would correctly reproduce all of the properties. This may be a sign that this potential is unable to capture the more complex bonding character of Au involving *s*-*d* orbital

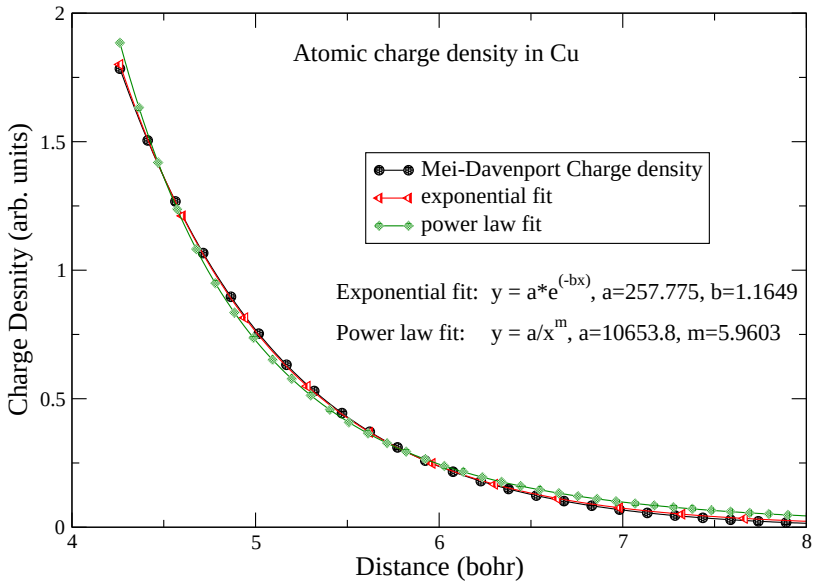

Figure 4.2: Comparison of charge density decays of Cu from various models. Included are the results of Mei and Davenport (a polynomial decay) and an exponential decay of the type used in the Modified Sutton-Chen potential.

hybridization [28], [48]. Some results for Au were not reproduced accurately as a result. It is worth noting that Au is a particularly difficult metal to describe with such a potential, as can be seen from the previous results of this work.

Results for the MSC potential are given in Figs. 4.3 to 4.30 and are plotted with those of the SC and QSC potentials for comparison.

Referring to Fig. 4.3, it can be seen that the MSC does not improve significantly on the QSC results, being slightly closer to experiment in the [100] transverse branch (4% too high versus 5% too low) but slightly further in the longitudinal (10% too high compared to 3.7% too low) at the zone boundary. The slopes of the curves near the zone center are better represented by the MSC, however. The situation is quite similar for Ag where the MSC is 1% to the transverse branch in the [100] direction but 2% further in the longitudinal. The reverse is true in the [111] direction. Despite being fit to only three of the four chosen properties, the results for Au are significantly

Table 4.1: Parameters for the Modified Sutton-Chen potential. Parameters were fit to cohesive energy, lattice parameter, elastic constant C_{11} and isothermal bulk modulus in all cases except for Au where fitting to bulk modulus was not possible.

Metal	ϵ (eV)	c	n	α	a (Å)
Cu	2.23462×10^{-3}	220.509	11.6386	5.56463	3.6150
Ag	2.19855×10^{-3}	147.145	11.9227	7.82127	4.0860
Au	9.57463×10^{-3}	38.2201	10.2109	10.3061	4.0790
Pt	8.27886×10^{-3}	71.9841	11.2309	9.33477	3.9240

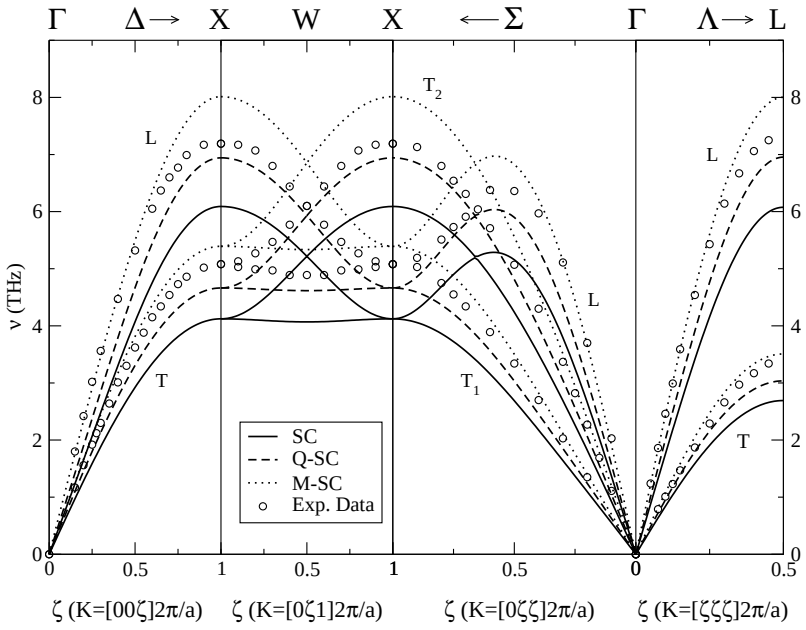

Figure 4.3: Phonon dispersion curves for Cu as calculated using the Modified Sutton-Chen potential. Results for the Sutton-Chen and Quantum Sutton-Chen potentials are included for comparison. Experimental data taken from [6].

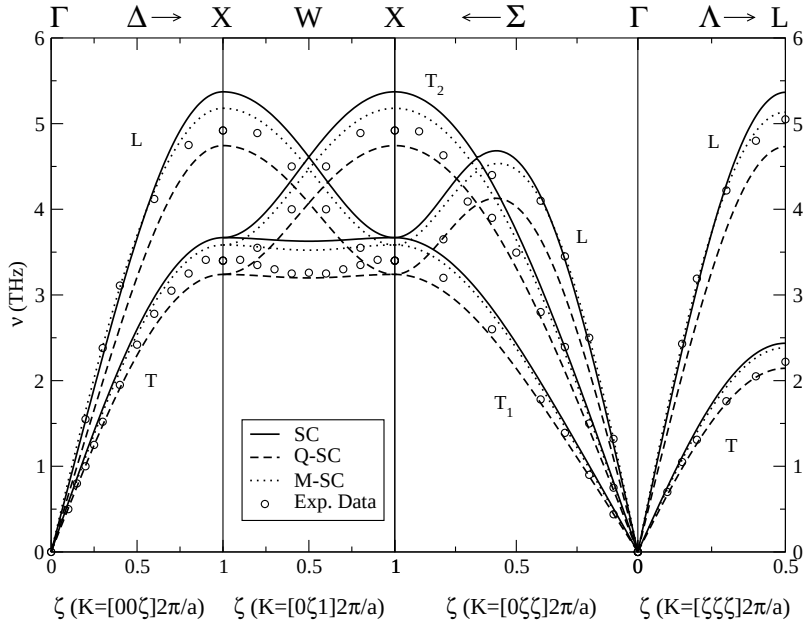

Figure 4.4: Phonon dispersion curves for Ag as calculated using the Modified Sutton-Chen potential. Results for the Sutton-Chen and Quantum Sutton-Chen potentials are included for comparison. Experimental data taken from [6].

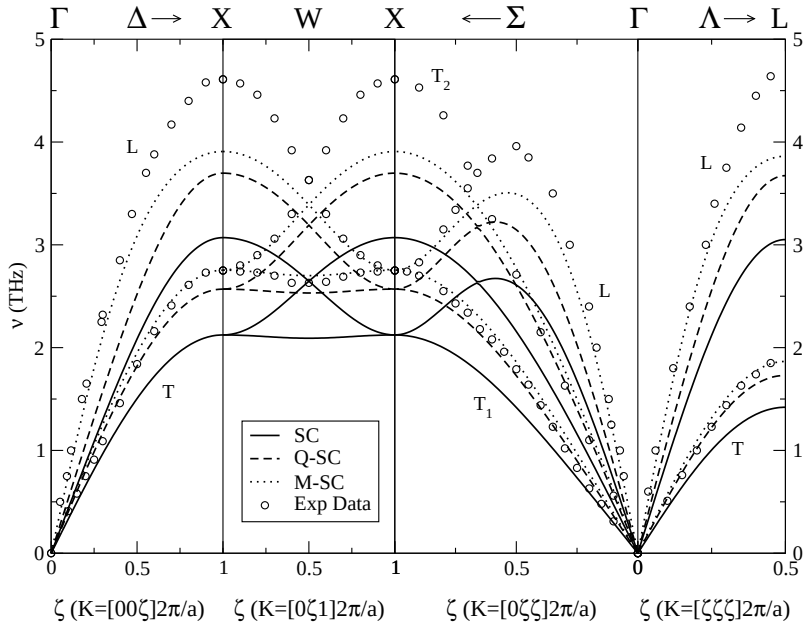

Figure 4.5: Phonon dispersion curves for Au as calculated using the Modified Sutton-Chen potential. Results for the Sutton-Chen and Quantum Sutton-Chen potentials are included for comparison. Experimental data taken from [6].

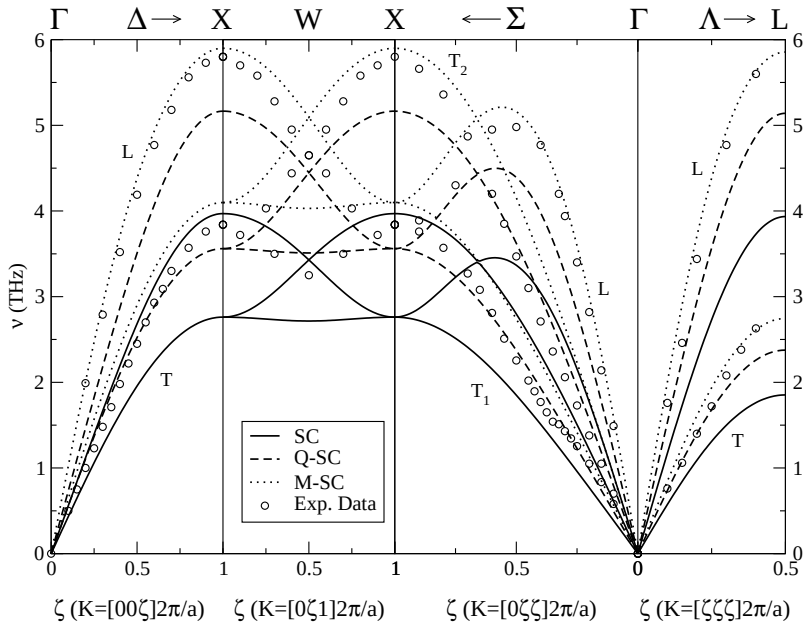

Figure 4.6: Phonon dispersion curves for Pt as calculated using the Modified Sutton-Chen potential. Results for the Sutton-Chen and Quantum Sutton-Chen potentials are included for comparison. Experimental data taken from [6].

improved for the MSC compared to both the SC and QSC. The transverse branches are reproduced almost exactly in all cases except the T_2 branch in the [110] direction. In the [100] direction, the longitudinal branch is 19% too low at the X-point compared with the QSC result being 23% too low. For Pt the results again favour the MSC which overestimates the [100] longitudinal branch by 1.5% compared to the QSC's 11% underestimation at the zone boundary. Both the QSC and MSC are 5% from experiment in the transverse branch of the same direction. Phonons in the [111] direction are best reproduced by the MSC potential.

Comparing these phonon calculations to those of the pair-potentials, it is difficult to determine which method is best overall. The Erkoç potential does well for Cu at the zone boundaries but the slopes near the zone center are too low. This also leads to poor results for the bulk modulus and elastic constants since they are directly related to the slopes of the dispersion curves [49]. Au is overall best represented by the MSC potential, though none of the models considered thus far are very accurate

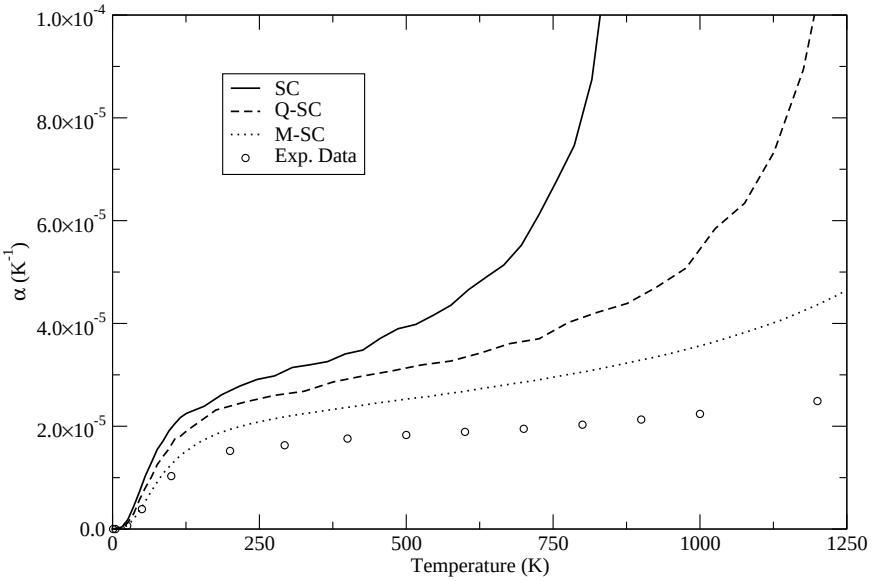

Figure 4.7: Thermal expansion coefficient for Cu as calculated using the Modified Sutton-Chen potential. Results for the Sutton-Chen and Quantum Sutton-Chen potentials are included for comparison. Experimental data taken from [9].

over the entire spectrum. As for Ag, the QSC and MSC fare about equally well and do improve over the pair-potential results.

Cu is often seen as a benchmark for inter-atomic potentials because certain properties can be well represented even by pair-potential models [50]. Despite this, the results for the thermal expansion coefficient of Cu do not agree with experimental data for the MSC as well as the SC and QSC potentials. It is 35% too large for the MSC, 62% too large for the QSC and nearly double the experimental value for the SC at 300K. Results for the phonon dispersion curves are mixed. The longitudinal branches are better represented by the QSC potential, but most of the transverse are better predicted by the MSC. The slopes of the dispersion curves at low **k**-values are fit well by the MSC. This is to be expected because this potential was directly fit to C_{11}, a quantity that depends on the slopes of the dispersion curves near the FBZ center [28]. The isothermal bulk modulus is better represented by the MSC since it was directly fit to this quantity. The adiabatic case is slightly different, however, since the SC underestimates it by 8% while the MSC overestimates it by 3% at 300K.

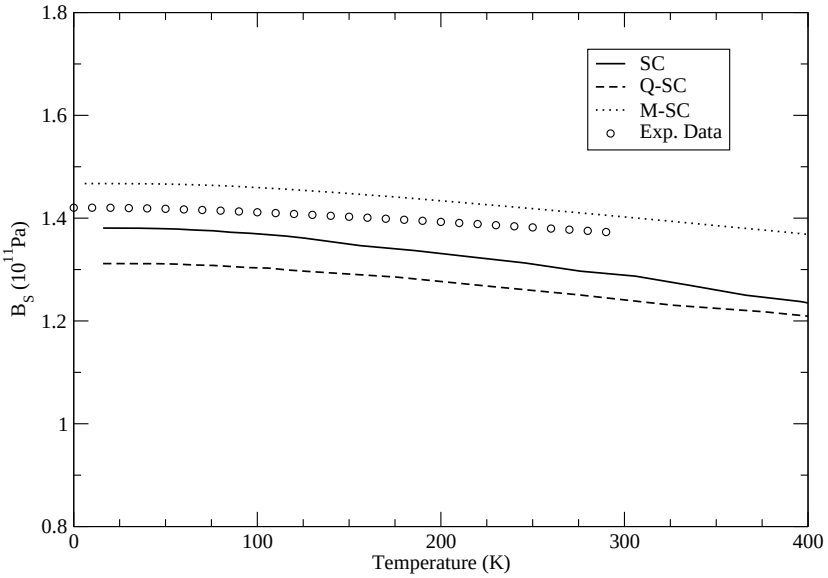

Figure 4.8: Adiabatic bulk modulus for Cu as calculated using the Modified Sutton-Chen potential. Results for the Sutton-Chen and Quantum Sutton-Chen potentials are included for comparison. Experimental data taken from [10].

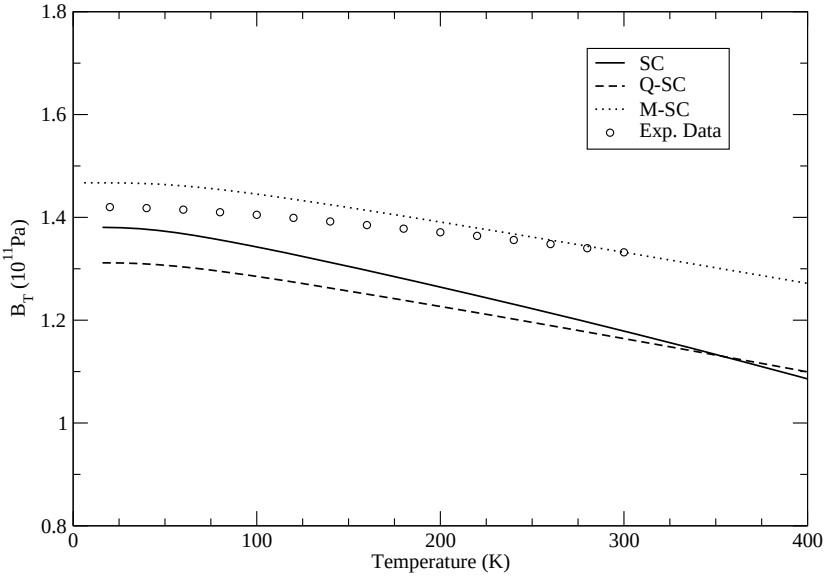

Figure 4.9: Isothermal bulk modulus for Cu as calculated using the Modified Sutton-Chen potential. Results for the Sutton-Chen and Quantum Sutton-Chen potentials are included for comparison. Experimental data taken from [11] and [12].

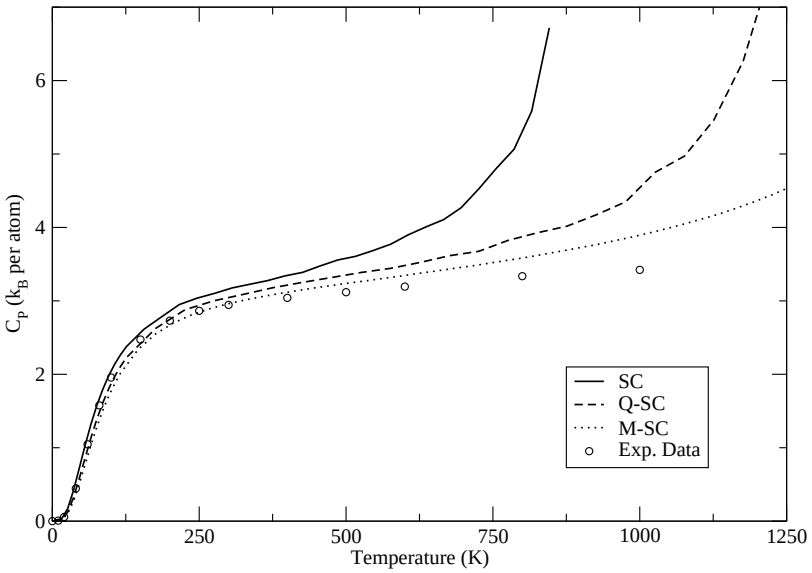

Figure 4.10: Specific heat at constant pressure for Cu as calculated using the Modified Sutton-Chen potential. Results for the Sutton-Chen and Quantum Sutton-Chen potentials are included for comparison. Experimental data taken from [13].

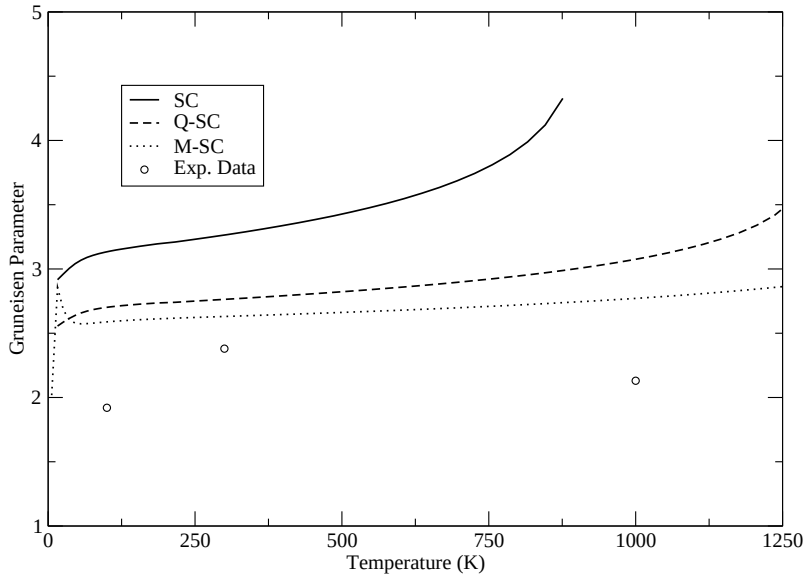

Figure 4.11: Grüneisen parameter for Cu as calculated using the Modified Sutton-Chen potential. Results for the Sutton-Chen and Quantum Sutton-Chen potentials are included for comparison. Experimental data taken from [14].

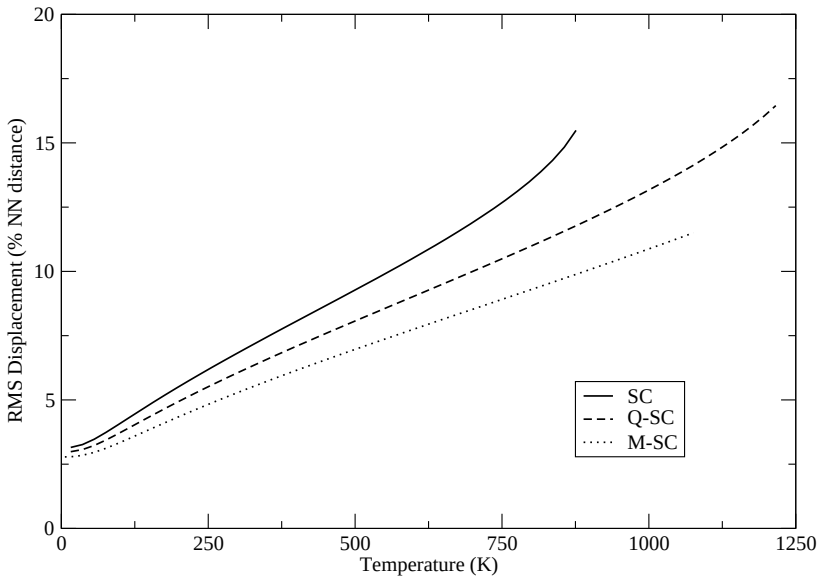

Figure 4.12: Atomic root-mean-square displacement for Cu as calculated using the Modified Sutton-Chen potential. Results for the Sutton-Chen and Quantum Sutton-Chen potentials are included for comparison.

The QSC underestimates it further by 9%. Experimental data is very limited for the Grüneisen parameter and what there is often has a significant error margin associated with it. The MSC predicts a value that is 10% too large at 300K while the SC and QSC predict values that are 49% and 17% too large, respectively.

Ag is unique in this study since it is the only element where most results of the QSC are actually further from experiment than those of the SC potential. The MSC does offer modest improvement in most ways, though the phonon spectrum is not consistently better represented. Both the longitudinal and transverse modes are 8% too large at the X-point for the MSC. The QSC does fare better here than the SC overall, with nearly exact agreement for the transverse branch in the [111] direction. None of the potentials predict the path X-W-X very accurately. The thermal expansion coefficient too large in all cases once again: 36% for the MSC, 58% for the SC and 66% for the QSC. The isothermal and adiabatic bulk moduli are best predicted by the MSC, with 1% and 2% deviation from experiment, respectively. Isobaric heat capacity is nearly identical for all three potentials up to about 300K

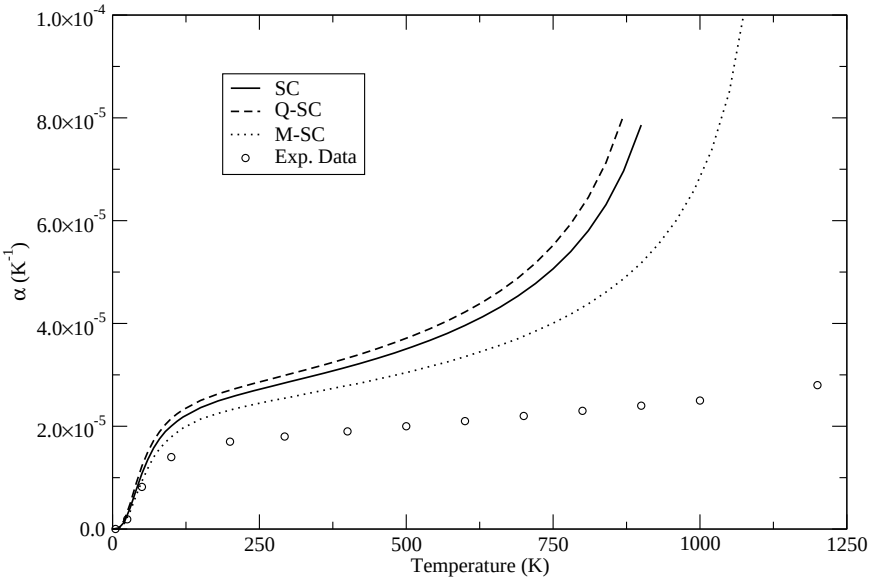

Figure 4.13: Thermal expansion coefficient for Ag as calculated using the Modified Sutton-Chen potential. Results for the Sutton-Chen and Quantum Sutton-Chen potentials are included for comparison. Experimental data taken from [9].

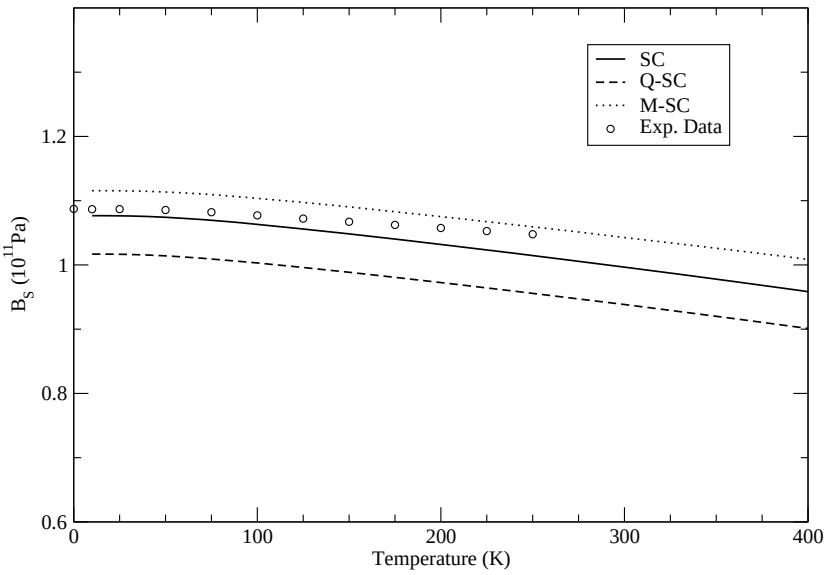

Figure 4.14: Adiabatic bulk modulus for Ag as calculated using the Modified Sutton-Chen potential. Results for the Sutton-Chen and Quantum Sutton-Chen potentials are included for comparison. Experimental data taken from [10].

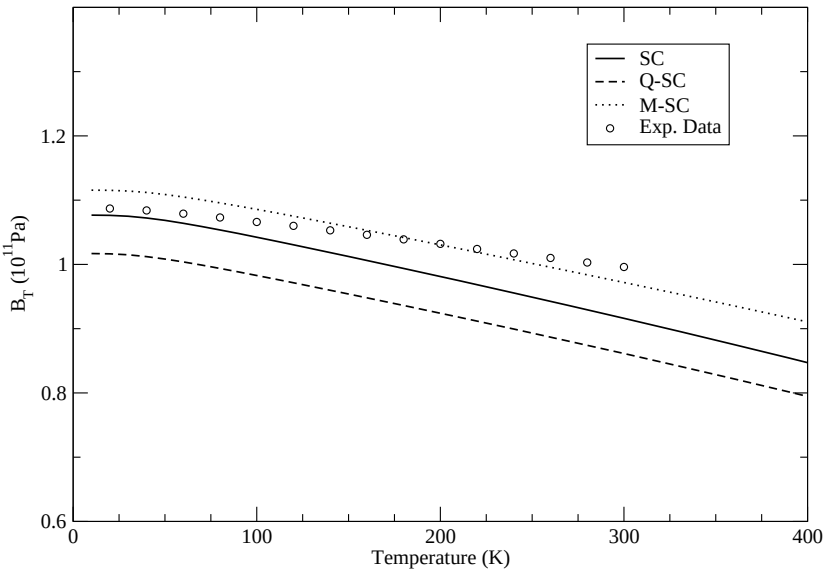

Figure 4.15: Isothermal bulk modulus for Ag as calculated using the Modified Sutton-Chen potential. Results for the Sutton-Chen and Quantum Sutton-Chen potentials are included for comparison. Experimental data taken from [11] and [12].

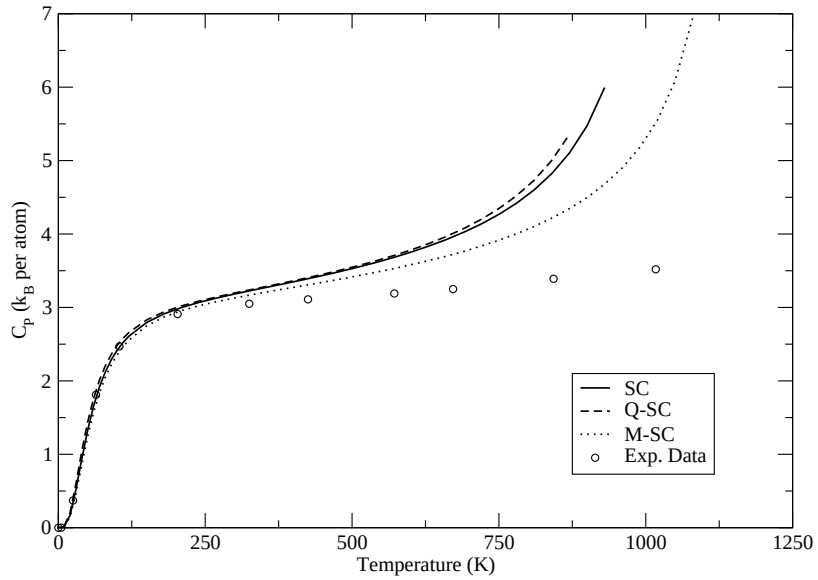

Figure 4.16: Specific heat at constant pressure for Ag as calculated using the Modified Sutton-Chen potential. Results for the Sutton-Chen and Quantum Sutton-Chen potentials are included for comparison. Experimental data taken from [13].

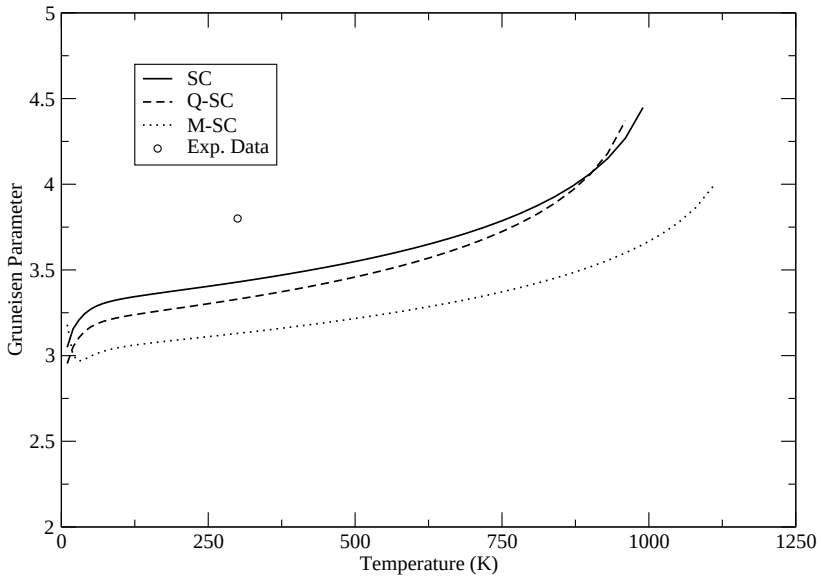

Figure 4.17: Grüneisen parameter for Ag as calculated using the Modified Sutton-Chen potential. Results for the Sutton-Chen and Quantum Sutton-Chen potentials are included for comparison. Experimental data taken from [14].

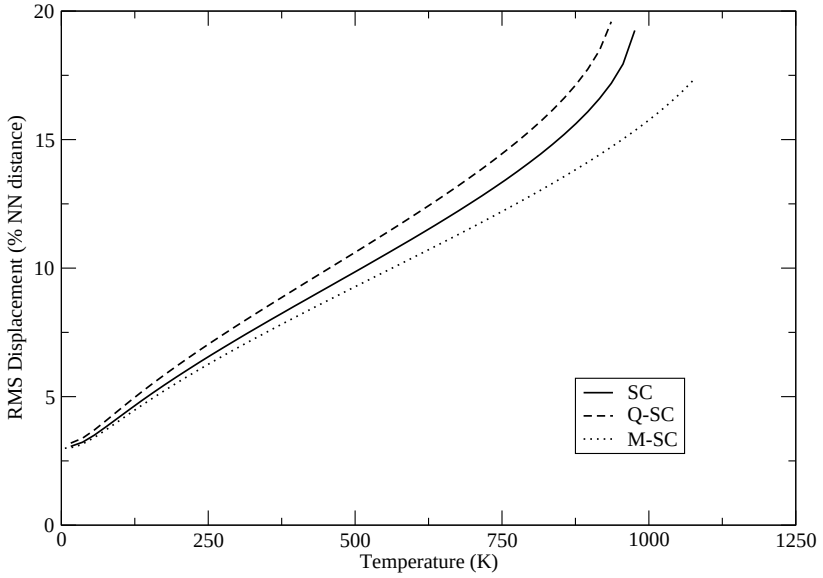

Figure 4.18: Atomic root-mean-square displacement for Ag as calculated using the Modified Sutton-Chen potential. Results for the Sutton-Chen and Quantum Sutton-Chen potentials are included for comparison.

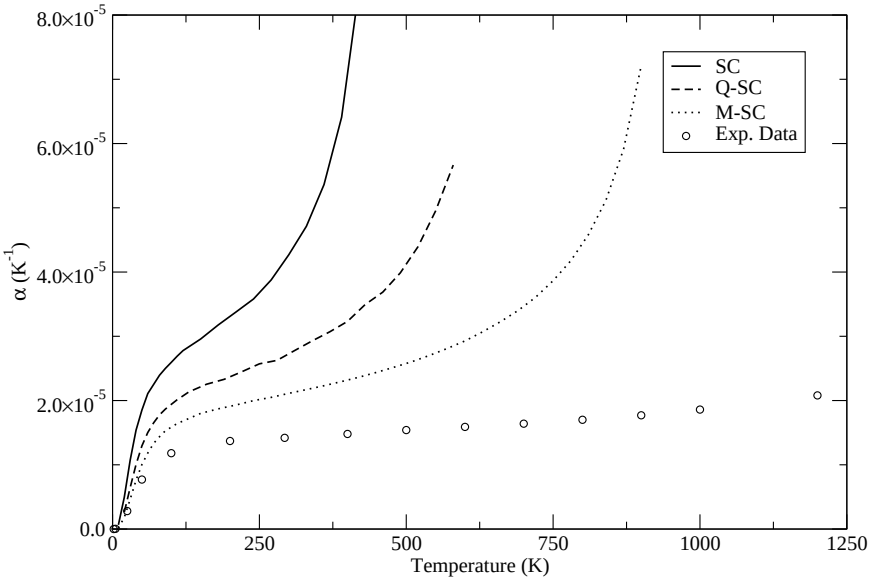

Figure 4.19: Thermal expansion coefficient for Au as calculated using the Modified Sutton-Chen potential. Results for the Sutton-Chen and Quantum Sutton-Chen potentials are included for comparison. Experimental data taken from [9].

beyond which the MSC remains closest to experimental values.

Results for Au are noteworthy since this was the only element where four parameters were fit to three experimental properties. When attempting to fit to all four experimental properties, achieving convergence of the parameters proved impossible. Because of this, fitting to isothermal bulk modulus was omitted. Even so, results are largely improved over the SC and QSC potentials for most properties. As expected, the bulk moduli are only about as accurate as those predicted by the QSC and their curves cross over at one point in the range 100-180K. The thermal expansion coefficient is still 50% too large for the MSC at 300K, though it does improve on both the SC and QSC results (which are 190% and 93% too large, respectively). Phonon spectra are very well represented by the MSC for all lower transverse branches in the symmetry directions. The longitudinal modes, while improved over the other potentials, are still 17% too low in the [100] direction for example.

The results for Pt are improved in nearly all properties with the MSC potential. The thermal expansion deviates from experiment by 37% at 300K for the MSC, 75%

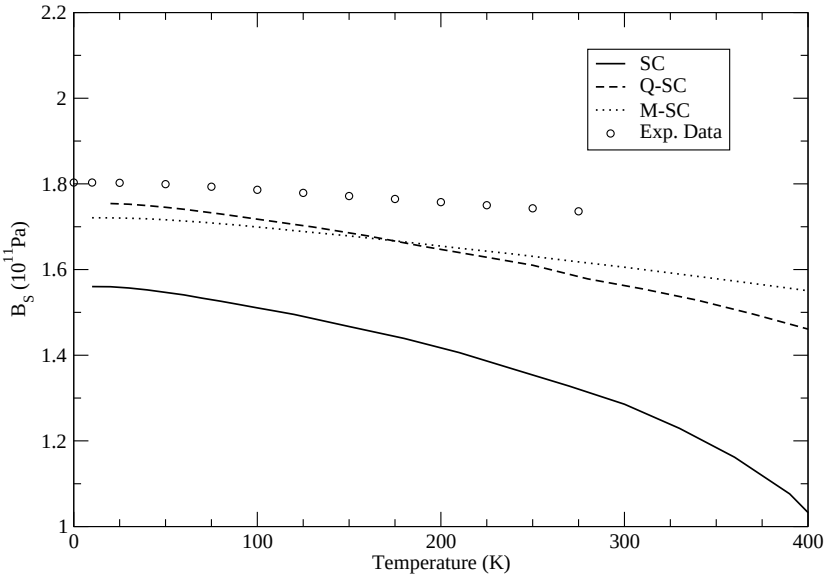

Figure 4.20: Adiabatic bulk modulus for Au as calculated using the Modified Sutton-Chen potential. Results for the Sutton-Chen and Quantum Sutton-Chen potentials are included for comparison. Experimental data taken from [10].

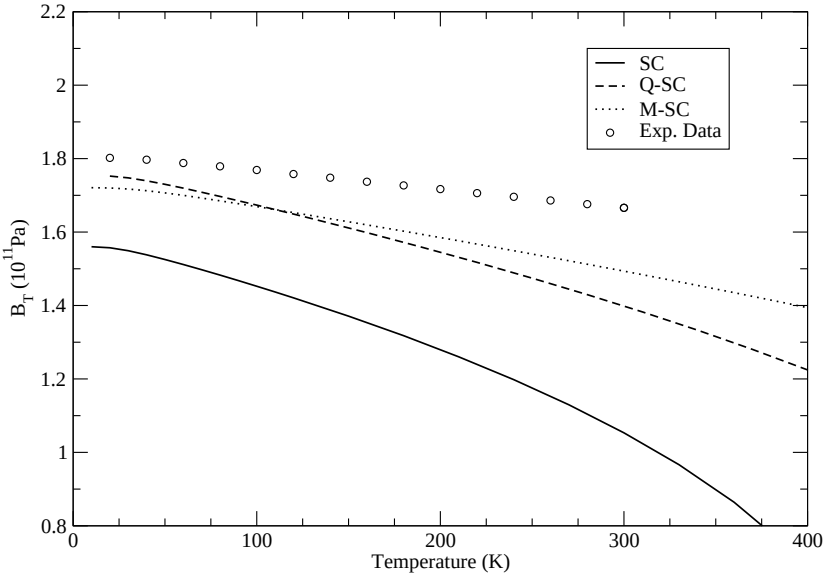

Figure 4.21: Isothermal bulk modulus for Au as calculated using the Modified Sutton-Chen potential. Results for the Sutton-Chen and Quantum Sutton-Chen potentials are included for comparison. Experimental data taken from [11] and [12].

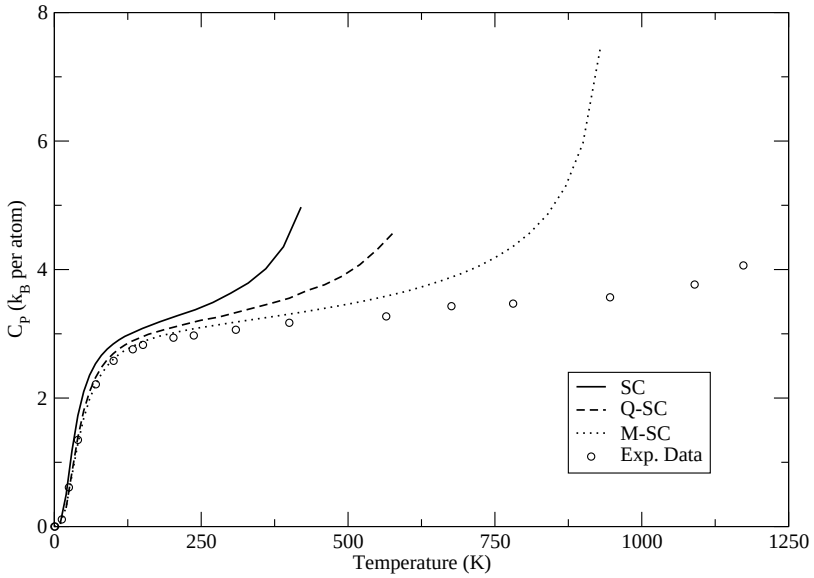

Figure 4.22: Specific heat at constant pressure for Au as calculated using the Modified Sutton-Chen potential. Results for the Sutton-Chen and Quantum Sutton-Chen potentials are included for comparison. Experimental data taken from [13].

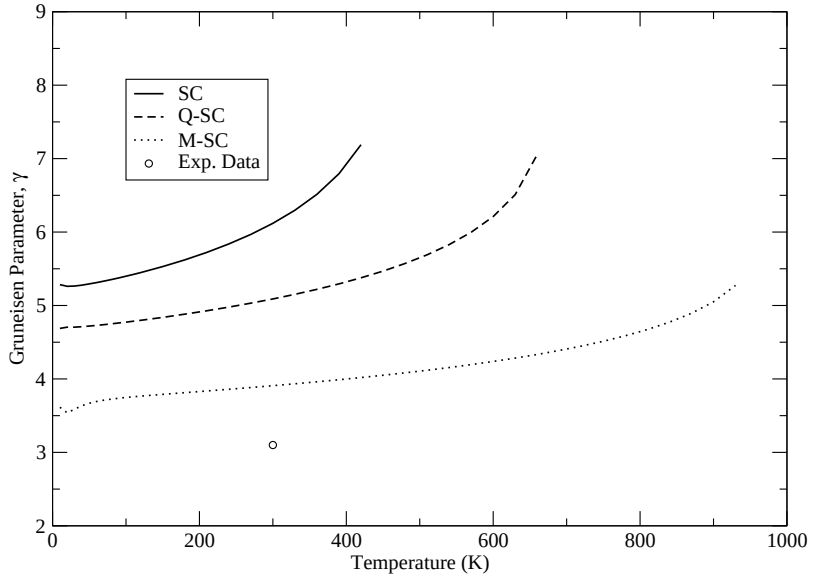

Figure 4.23: Grüneisen parameter for Au as calculated using the Modified Sutton-Chen potential. Results for the Sutton-Chen and Quantum Sutton-Chen potentials are included for comparison. Experimental data taken from [16].

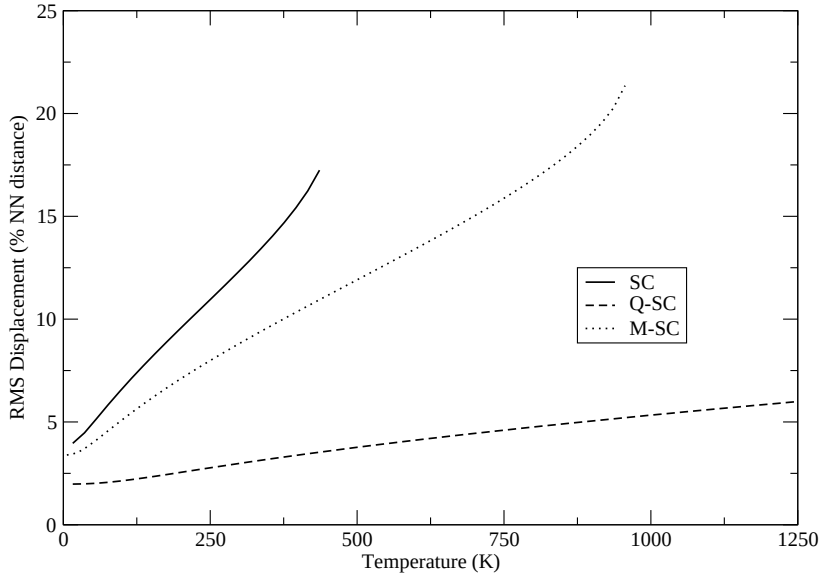

Figure 4.24: Atomic root-mean-square displacement for Au as calculated using the Modified Sutton-Chen potential. Results for the Sutton-Chen and Quantum Sutton-Chen potentials are included for comparison.

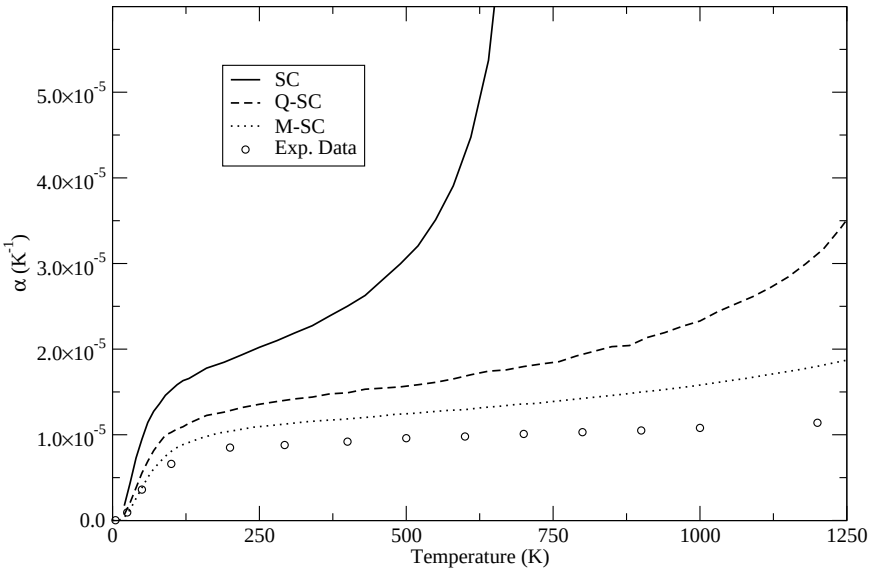

Figure 4.25: Thermal expansion coefficient for Pt as calculated using the Modified Sutton-Chen potential. Results for the Sutton-Chen and Quantum Sutton-Chen potentials are included for comparison. Experimental data taken from [9].

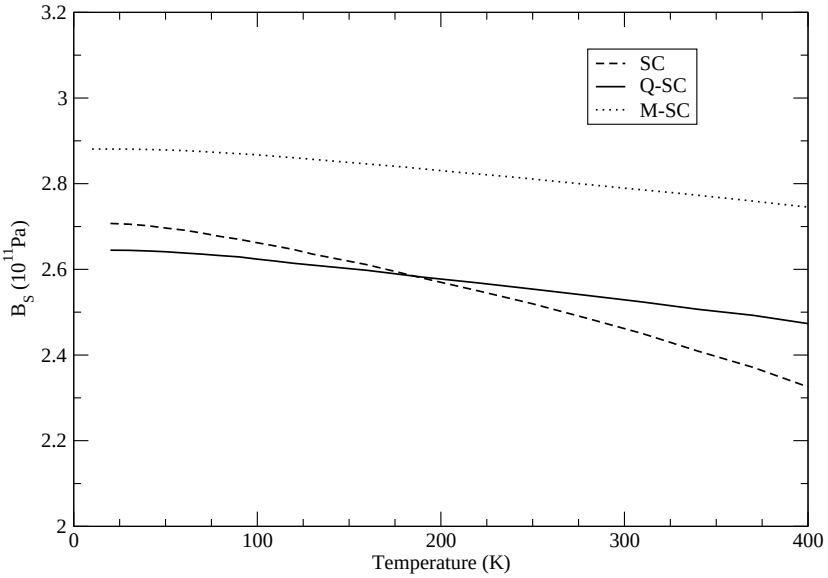

Figure 4.26: Adiabatic bulk modulus for Pt as calculated using the Modified Sutton-Chen potential. Results for the Sutton-Chen and Quantum Sutton-Chen potentials are included for comparison. Experimental data taken from [10].

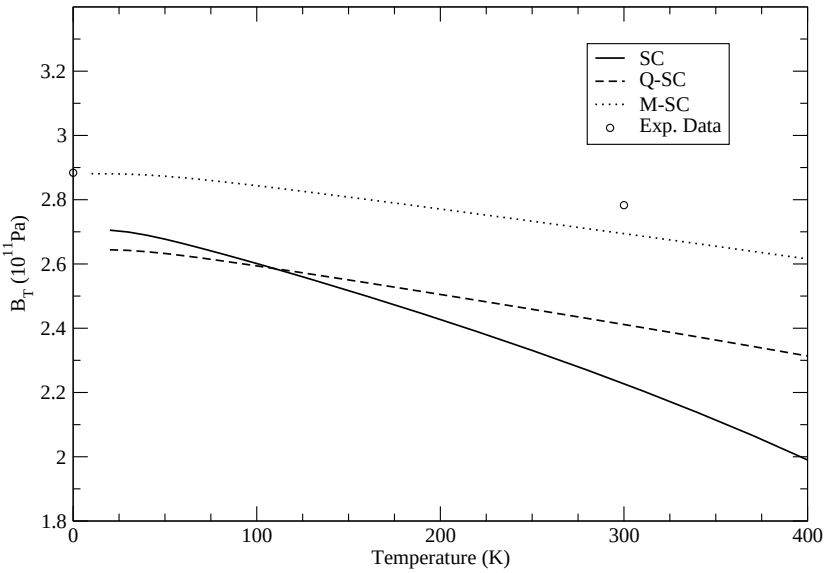

Figure 4.27: Isothermal bulk modulus for Pt as calculated using the Modified Sutton-Chen potential. Results for the Sutton-Chen and Quantum Sutton-Chen potentials are included for comparison. Experimental data taken from [11] and [12].

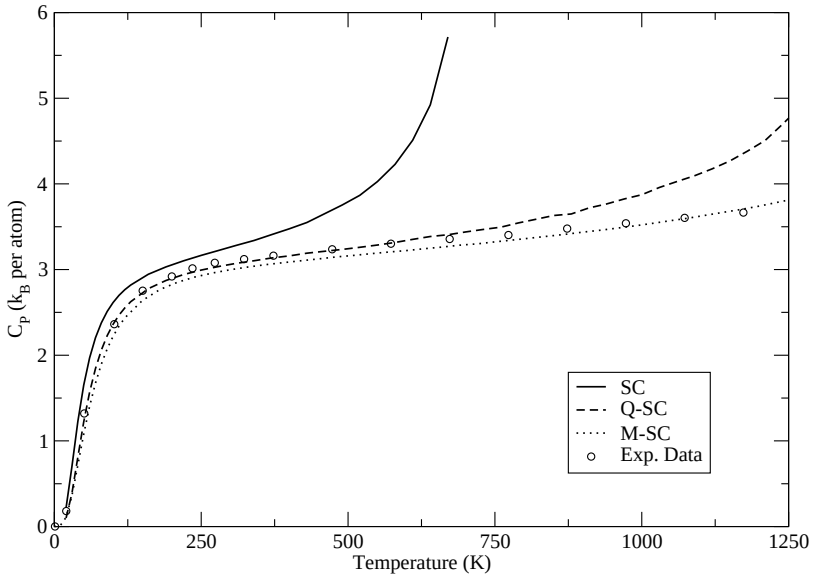

Figure 4.28: Specific heat at constant pressure for Pt as calculated using the Modified Sutton-Chen potential. Results for the Sutton-Chen and Quantum Sutton-Chen potentials are included for comparison. Experimental data taken from [13].

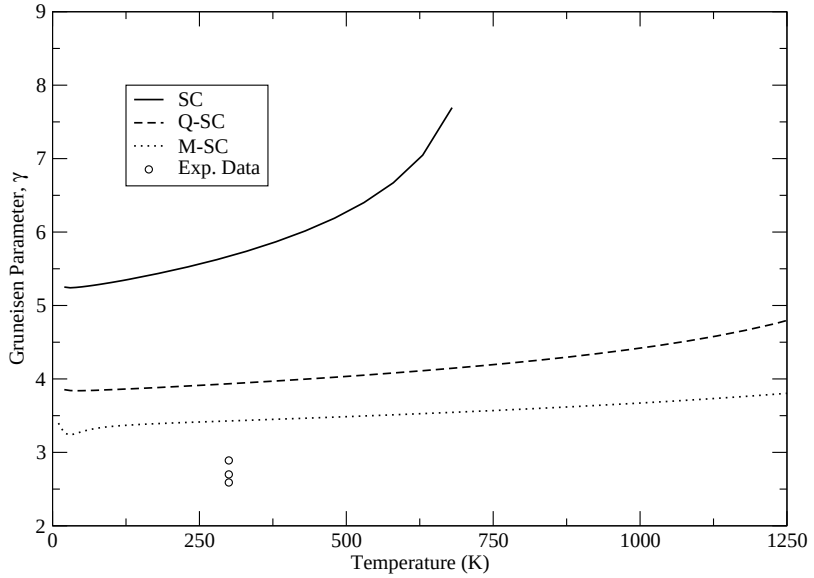

Figure 4.29: Grüneisen parameter for Pt as calculated using the Modified Sutton-Chen potential. Results for the Sutton-Chen and Quantum Sutton-Chen potentials are included for comparison. Experimental data taken from [16].

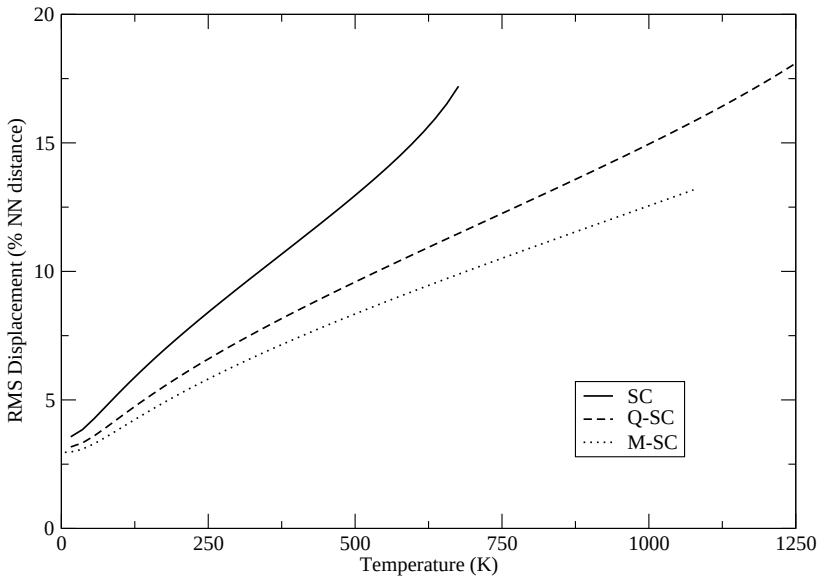

Figure 4.30: Atomic root-mean-square displacement for Pt as calculated using the Modified Sutton-Chen potential. Results for the Sutton-Chen and Quantum Sutton-Chen potentials are included for comparison.

for the QSC and 168% for the SC potential. Isobaric specific heat is slightly too low at temperatures in the range 0-750K but agrees well with experiment beyond that. Due to limited availability of experimental data for the adiabatic bulk modulus, it is difficult to compare the potentials in this case. The isothermal bulk modulus is better represented by the MSC than both the SC and QSC, however. At 300K the MSC predicts a B_T that is 7% too large, while the SC is 17% too low and the QSC is 10% too low. Phonon curves are improved in all branches and agree very well with experiment in the [111] direction in particular.

The calculated elastic constants for the Morse, Erkoç and Sutton-Chen–type potentials are given in Tables 4.2 to 4.5. All values are given at 0K.

C_{11} is generally well represented by the MSC potential, as one would expect given that it was fit to this constant. The fitting was done at 300K rather than 0K, however, which does lead to some (expected) discrepancies in the results. In all cases, C_{11} is slightly overestimated at 0K by the MSC while C_{12} is slightly too low. It is very close in Cu and Ag, being 1% and 3% too low, respectively. C_{12} is best

Table 4.2: Elastic constants C_{11}, C_{12} and C_{44} at 0K for Cu as calculated with the Morse, Erkoç, Sutton-Chen, Quantum Sutton-Chen and Modified Sutton-Chen models. Experimental data taken from [5]. All values expressed in units of 10^{11}Pa.

Cu	C_{11}	C_{12}	C_{44}
Exp.	1.7620	1.2494	0.8177
Morse-V	1.7523	1.0274	1.0274
Morse-S	1.6291	1.1444	1.1444
Erkoç	0.8630	0.6368	0.6368
SC	1.6451	1.2526	0.5639
Q-SC	1.6447	1.1451	0.7101
M-SC	1.8438	1.2333	0.9060

Table 4.3: Elastic constants C_{11}, C_{12} and C_{44} at 0K for Ag as calculated with the Morse, Erkoç, Sutton-Chen, Quantum Sutton-Chen and Modified Sutton-Chen models. Experimental data taken from [5]. All values expressed in units of 10^{11}Pa.

Ag	C_{11}	C_{12}	C_{44}
Exp.	1.3149	0.9733	0.5109
Morse-S	1.2407	0.8472	0.8472
Erkoç	0.9203	0.5757	0.5757
SC	1.3692	0.9308	0.5746
Q-SC	1.2698	0.8905	0.5113
M-SC	1.4028	0.9493	0.6184

Table 4.4: Elastic constants C_{11}, C_{12} and C_{44} at 0K for Au as calculated with the Morse, Erkoç, Sutton-Chen, Quantum Sutton-Chen and Modified Sutton-Chen models. Experimental data taken from [5]. All values expressed in units of 10^{11}Pa.

Au	C_{11}	C_{12}	C_{44}
Exp.	2.0163	1.6967	0.4544
Morse-V	1.7399	0.9369	0.9369
Morse-S	1.6445	1.1087	1.1087
Erkoç	1.6389	0.9917	0.9917
SC	1.7763	1.4554	0.4178
Q-SC	2.0706	1.5976	0.5987
M-SC	2.0661	1.5355	0.6739

Table 4.5: Elastic constants C_{11}, C_{12} and C_{44} at 0K for Pt as calculated with the Sutton-Chen, Quantum Sutton-Chen and Modified Sutton-Chen models. Experimental data taken from [5]. All values expressed in units of 10^{11}Pa.

Pt	C_{11}	C_{12}	C_{44}
Exp.	3.5800	2.5360	0.7740
SC	3.0810	2.5250	0.7241
Q-SC	3.2193	2.3577	1.1272
M-SC	3.5848	2.5083	1.3847

reproduced by the QSC for Au and by the SC for Pt. The only instance where a pair potential produces the best result is C_{11} for Cu where the Morse-V is less than 1% from experiment. Overall the Sutton-Chen–type potentials perform considerably better here than the pair potentials. One key factor supporting this is that the Cauchy equality ($C_{12} = C_{44}$) is of course maintained by pair-potentials but violated by the many-body potentials, as is the case in real metallic systems [46].

Chapter 5

Tight-Binding Potentials

The Potentials of Cleri-Rosato and Dai *et al.*

We will now briefly examine the results of two tight-binding potentials, both employing the square-root density function; those of F. Cleri & V. Rosato [28] and X. Dai *et al.* [29]. The potential used by Cleri & Rosato (CR) was extended to include up to fifth-neighbour interactions and has the form

$$U(r_{ij}) = \sum_j A_{ij} e^{-p_{ij}\left(r_{ij}/r_0^{ij}-1\right)} - \left[\sum_j \xi_{ij}^2 e^{-2q_{ij}\left(r_{ij}/r_0^{ij}-1\right)}\right]^{1/2} \tag{5.0.1}$$

where A_{ij}, p_{ij}, ξ_{ij} and q_{ij} are groups of parameters that depend on the elements present in the solid (they each reduce to one value for pure solids). r_0^{ij} is the nearest-neighbour distance between atoms i and j which again reduces to one value for solids composed of one element. ξ is interpreted as an effective hopping integral that describes the overlap of the bonding orbitals. Values for these parameters for the elements considered here are given in Table 5.1.

Regarding the results for the phonon dispersion curves for Cu, the Dai *et al.* potential is better overall, though it does overestimate the longitudinal frequency in the [100] direction at the X-point by 10%. The CR is below experimental values by

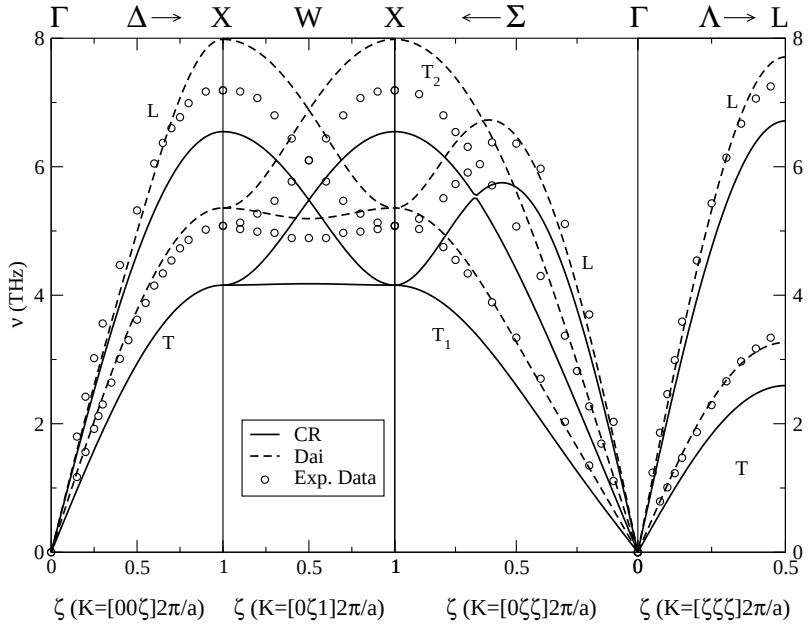

Figure 5.1: Phonon dispersion curves for Cu as calculated using the Cleri-Rosato and Dai *et al.* potentials. Experimental data taken from [6].

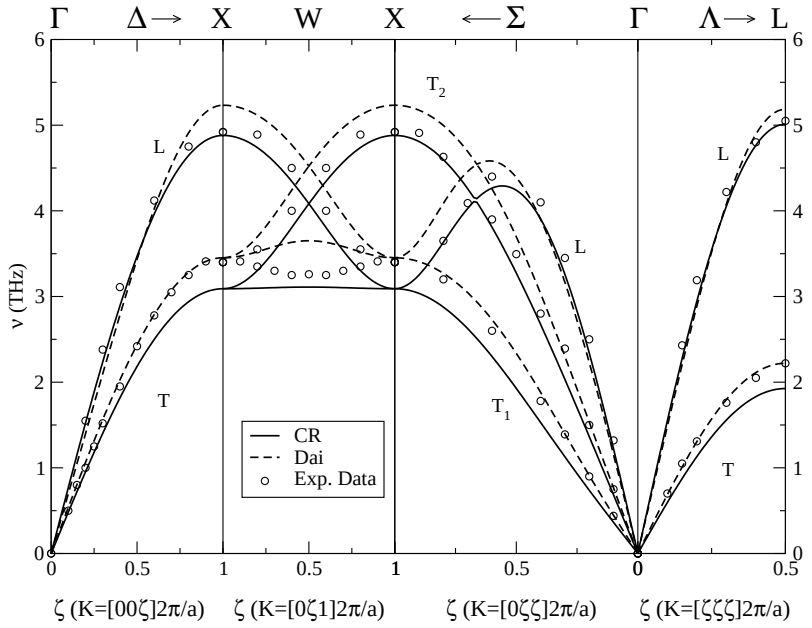

Figure 5.2: Phonon dispersion curves for Ag as calculated using the Cleri-Rosato and Dai *et al.* potentials. Experimental data taken from [7].

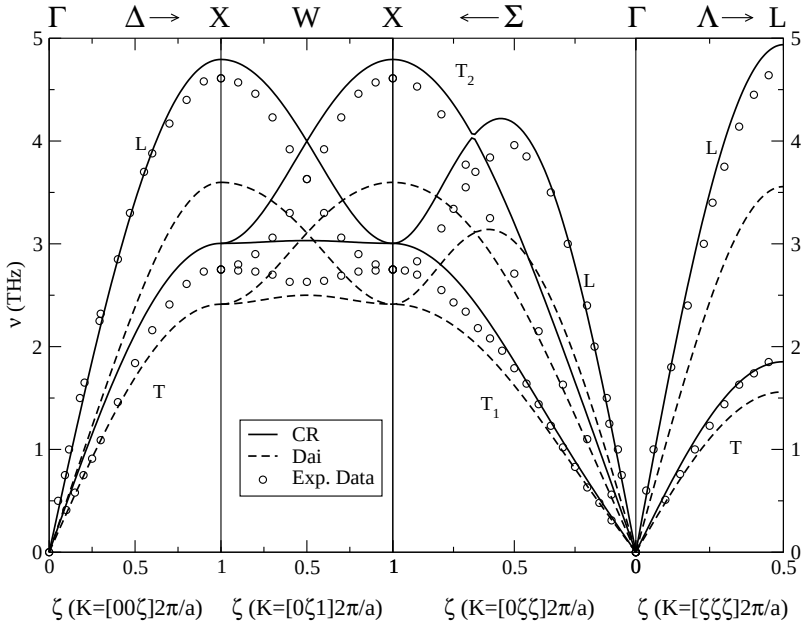

Figure 5.3: Phonon dispersion curves for Au as calculated using the Cleri-Rosato and Dai *et al.* potentials. Experimental data taken from [8].

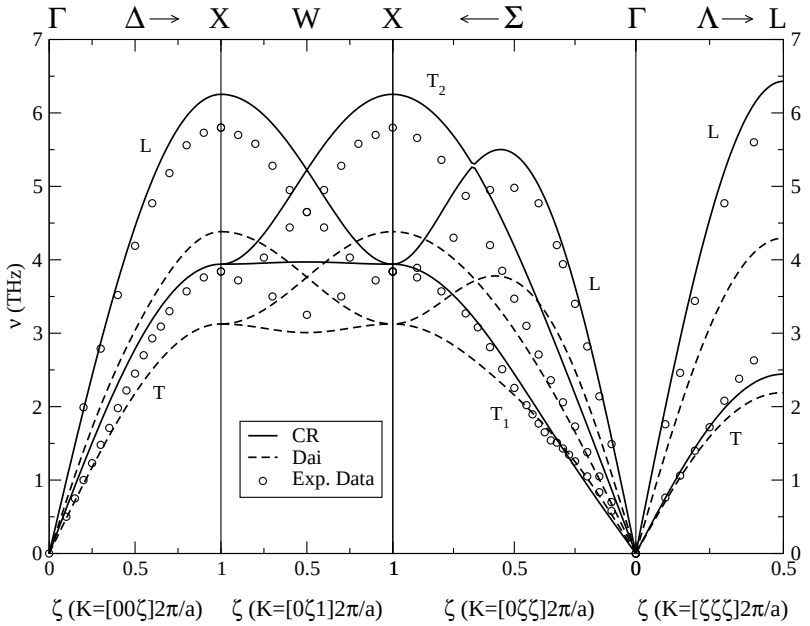

Figure 5.4: Phonon dispersion curves for Pt as calculated using the Cleri-Rosato and Dai *et al.* potentials. Experimental data taken from [8].

Table 5.1: Parameters for the Cleri-Rosato potential. Fitting was done to the experimental cohesive energy, lattice parameter and elastic constants. The range of interactions was limited to fifth-neighbours.

Metal	A (eV)	ξ (eV)	p	q
Cu	0.0855	1.224	10.960	2.278
Ag	0.1028	1.178	10.928	3.139
Au	0.2061	1.790	10.229	4.036
Pt	0.2975	2.695	10.612	4.004

9% in the same branch. The slopes of the dispersion curves near the zone center are better represented by the Dai potential, particularly in the [111] direction. Each of the branches in the [100] direction for Ag are well represented by one of the potentials: CR does well in the longitudinal direction while Dai performs better in the transverse. The well-matched branches are within 1% of experimental values in each case. The situation is similar in the [111] direction, though the Dai potential does not deviate as much. Phonons in Au are predicted quite well by the CR potential in the [100] direction with a deviation of 3.5% in the longitudinal and 5% in the transverse direction. This is a significant improvement over both the pair-potentials and also the SC and QSC models. The Dai potential does not perform very well here with a 23% underestimation of the longitudinal branch. Pt is predicted similarly with a maximum deviation of 8% for the CR at the X-point and 25% for the Dai potential. Again the CR performs slightly better than both the SC and QSC.

Results for thermal expansion, heat capacities, bulk moduli and RMS displacement are given in Figs. 5.1 to 5.28. There is significant improvement in most cases over the original SC and even QSC potentials. It is impossible to definitively state that this is due to the change in the density function since the entire potential has been changed. However, this, combined with the theoretical backing that the charge density in metals should decay faster than a power-law decay, suggests that an exponential function would be more appropriate.

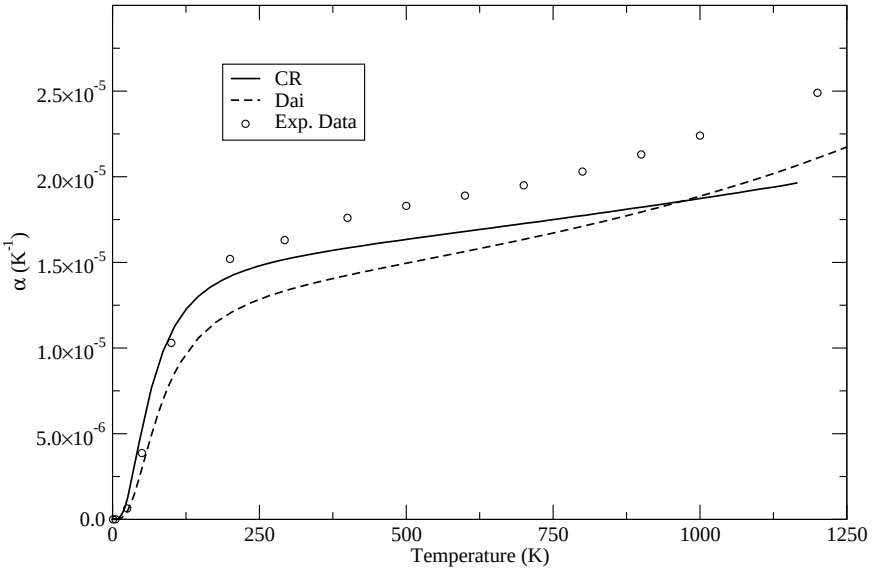

Figure 5.5: Thermal expansion coefficient for Cu as calculated using the Cleri-Rosato and Dai *et al.* potentials. Experimental data taken from [9].

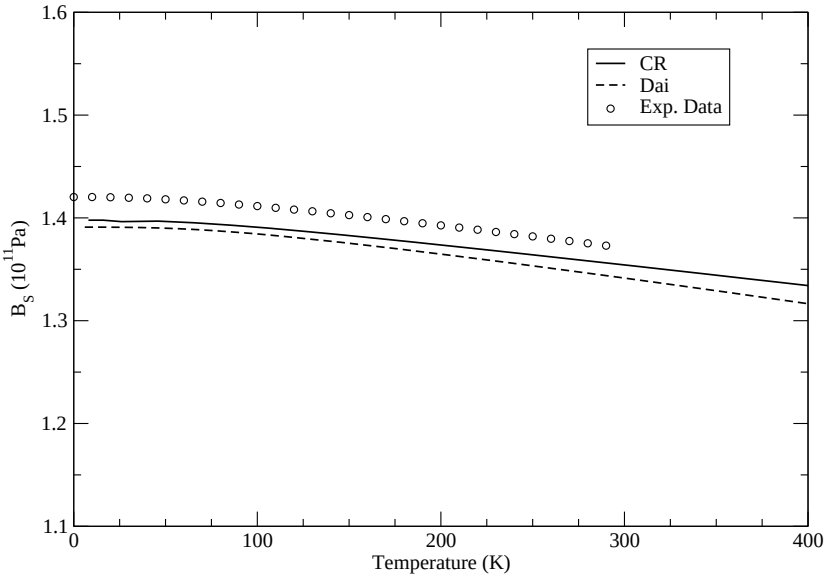

Figure 5.6: Adiabatic bulk modulus for Cu as calculated using the Cleri-Rosato and Dai *et al.* potentials. Experimental data taken from [10].

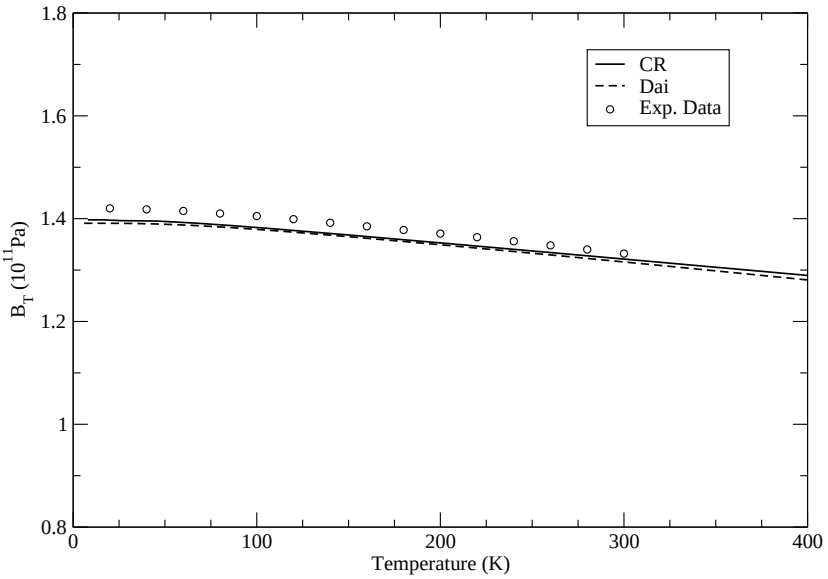

Figure 5.7: Isothermal bulk modulus for Cu as calculated using the Cleri-Rosato and Dai *et al.* potentials. Experimental data taken from [11] and [12].

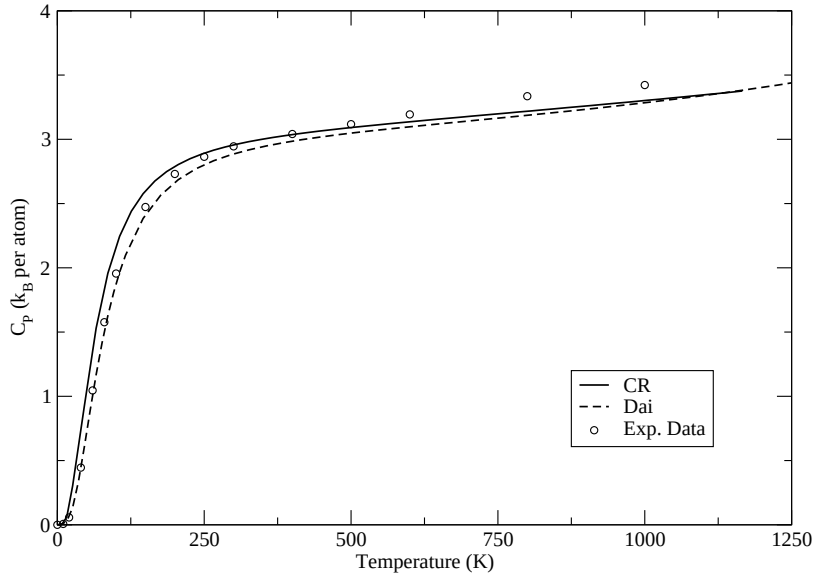

Figure 5.8: Specific heat at constant pressure for Cu as calculated using the Cleri-Rosato and Dai *et al.* potentials. Experimental data taken from [13].

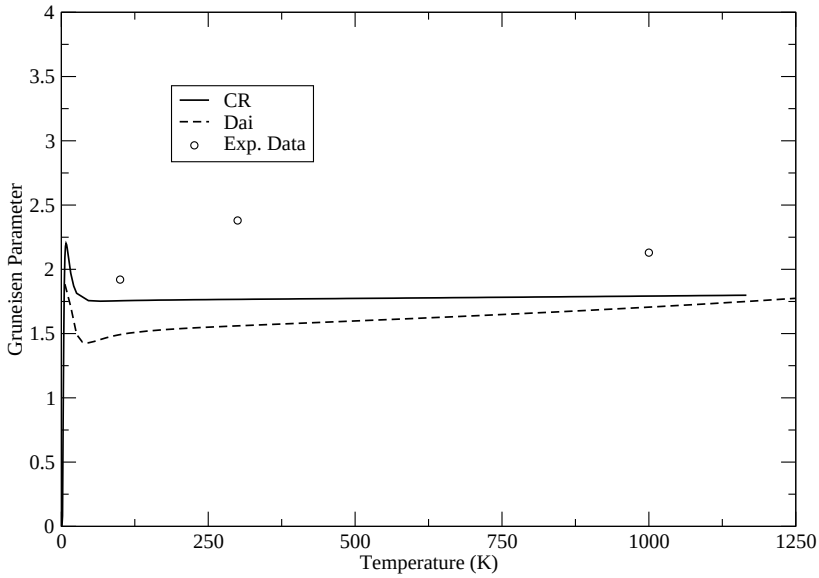

Figure 5.9: Grüneisen parameter for Cu as calculated using the Cleri-Rosato and Dai *et al.* potentials. Experimental data taken from [14].

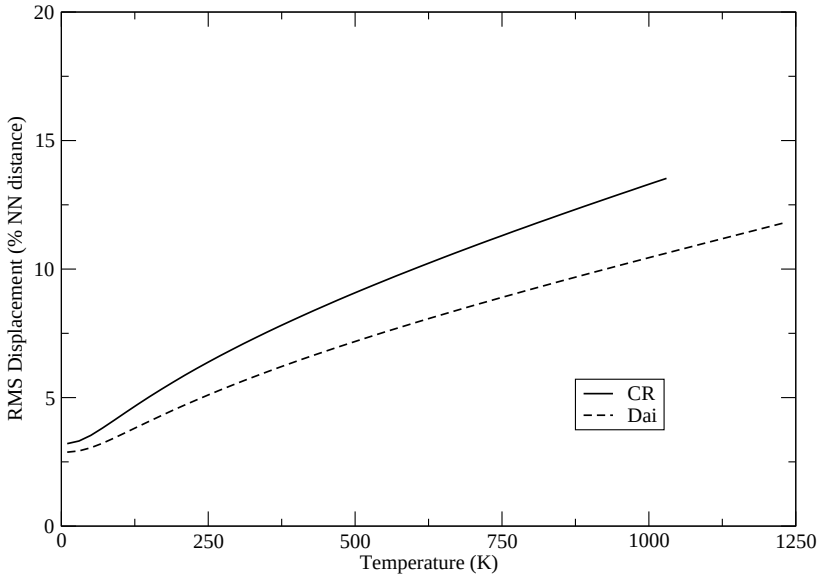

Figure 5.10: Atomic root-mean-square displacement for Cu as calculated using the Cleri-Rosato and Dai *et al.* potentials.

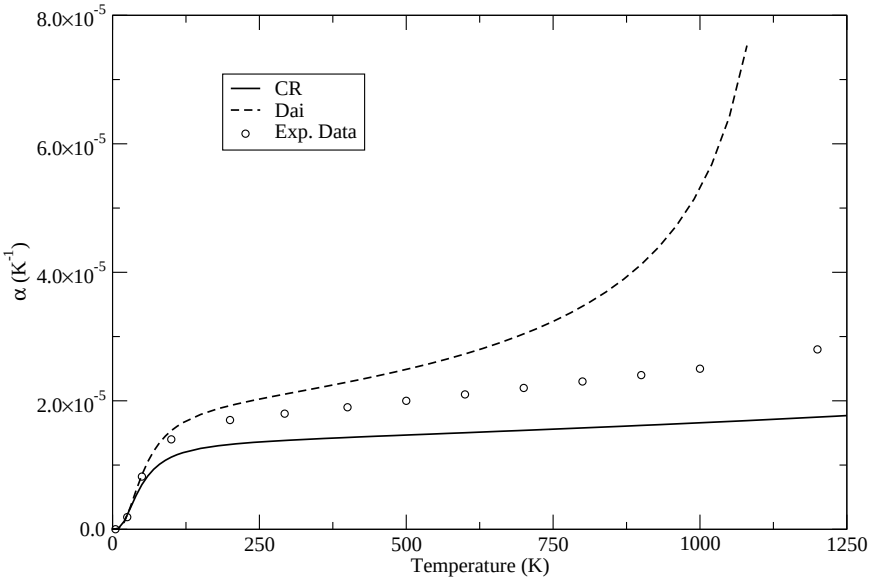

Figure 5.11: Thermal expansion coefficient for Ag as calculated using the Cleri-Rosato and Dai *et al.* potentials. Experimental data taken from [9].

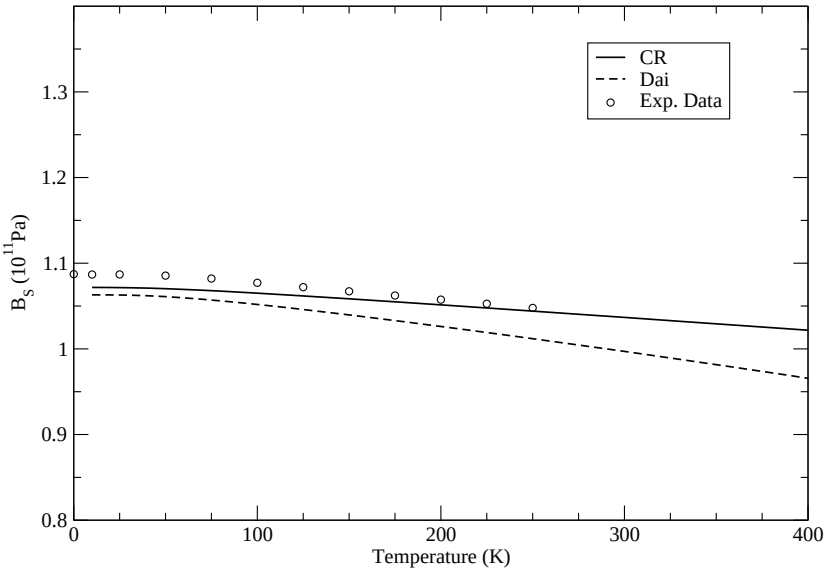

Figure 5.12: Adiabatic bulk modulus for Ag as calculated using the Cleri-Rosato and Dai *et al.* potentials. Experimental data taken from [15].

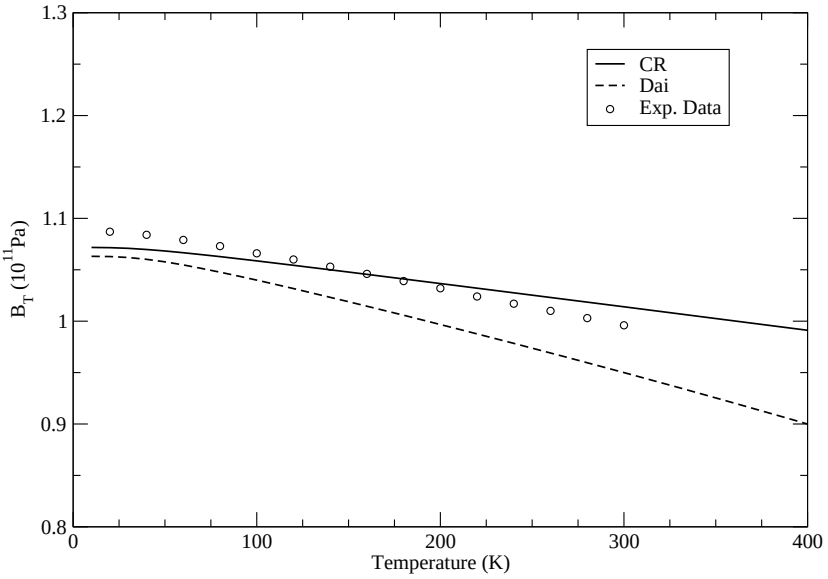

Figure 5.13: Isothermal bulk modulus for Ag as calculated using the Cleri-Rosato and Dai *et al.* potentials. Experimental data taken from [11] and [12].

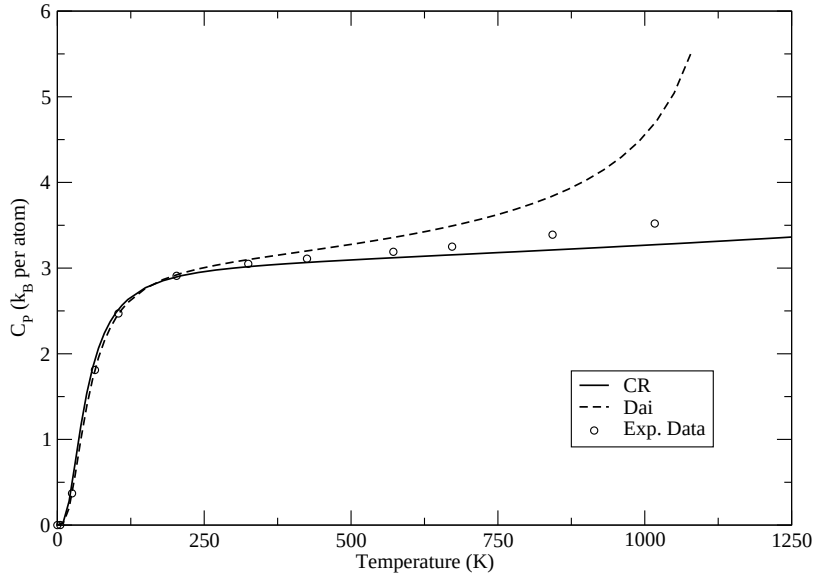

Figure 5.14: Specific heat at constant pressure for Ag as calculated using the Cleri-Rosato and Dai *et al.* potentials. Experimental data taken from [13].

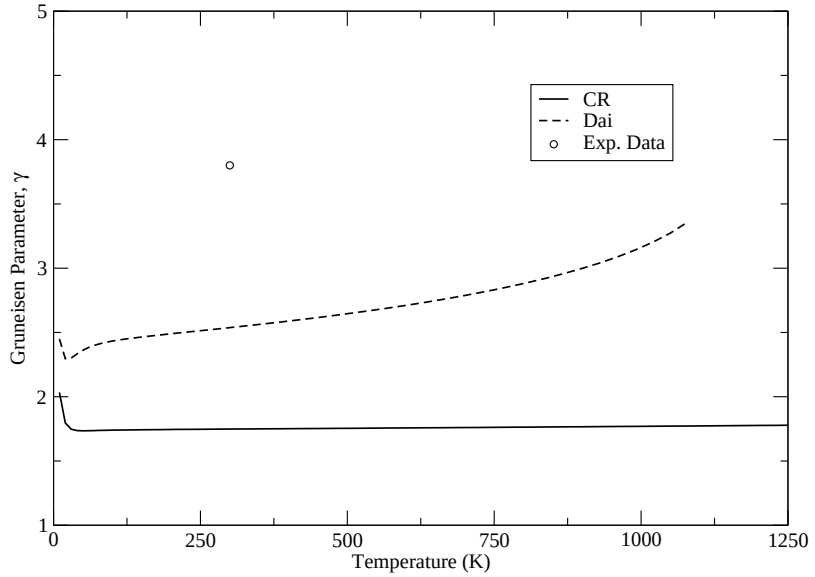

Figure 5.15: Grüneisen parameter for Ag as calculated using the Cleri-Rosato and Dai *et al.* potentials. Experimental data taken from [14].

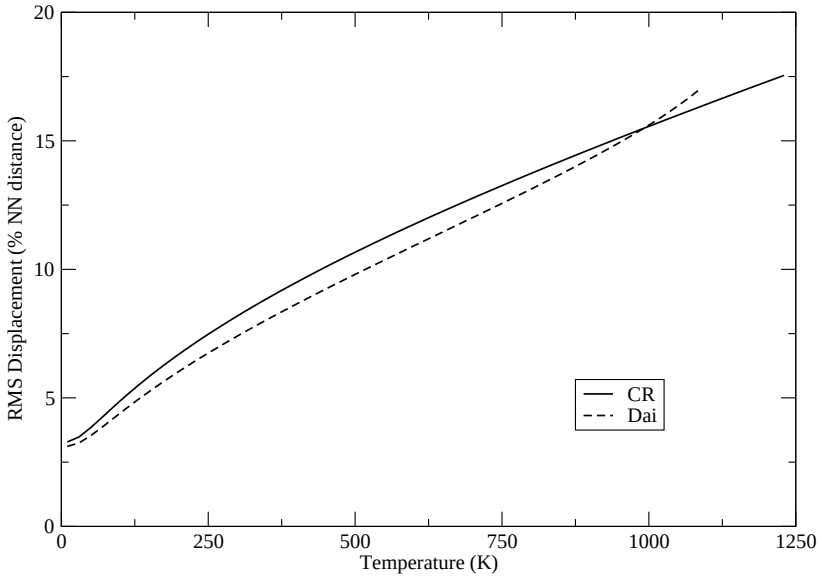

Figure 5.16: Atomic root-mean-square displacement for Ag as calculated using the Cleri-Rosato and Dai *et al.* potentials.

The potential used by Dai *et al.* (Dai) is given by

$$U(r_{ij}) = \sum_j (r_{ij} - r_{c1})^m (x_0 + x_1 r_{ij} + x_2 r_{ij}^2 + x_3 r_{ij}^3 + x_4 r_{ij}^4) - \left[\sum_j \alpha (r - r_{c2})^n e^{-\beta(r_{ij}/r_0 - 1)} \right]^{1/2} \tag{5.0.2}$$

with the conditions that the first term is zero if $r_{ij} > r_{c1}$ and the second term is zero if $r_{ij} > r_{c2}$. The parameters are x_0 through x_4, m, n, α and β. In this case r_0 is also treated as an adjustable parameter. r_{c1} and r_{c2} are clearly cutoff distances which can also be adjusted during the fitting procedure [29]. Since the pairwise repulsive term in 5.0.2 does not decay to zero at long ranges, such a cutoff is required in order to ensure stability of the crystal. For the FCC metals, the chosen cutoff radii were the fourth and seventh nearest-neighbours for the repulsive and cohesive terms, respectively. Fitting was done by matching calculated cohesive energy, lattice parameter and elastic constants to experimental values. Also used were the conditions that, at equilibrium, the first derivative of the potential and the stress of each unit cell is zero:

$$dE(r_{ij})\big|_{r_{ij}=r_0} = 0 \tag{5.0.3}$$

$$\sigma(r_{ij})\big|_{r_{ij}=r_0} = 0 \tag{5.0.4}$$

Values for the parameters are given in Table 5.2

Table 5.2: Parameters for the Dai *et al.* potential. Fitting was done to the experimental cohesive energy, lattice parameter and elastic constants as well as the conditions that the first derivative of the potential and stress of each unit cell be zero at equilibrium. The range of interactions was limited to fourth-neighbours for the repulsive part and seventh-neighbours for the cohesive part.

Parameter	Cu	Ag	Au	Pt
m	4	4	4	4
n	6	6	6	6
r_{c1}(Å)	6.100	6.375	6.400	6.440
r_{c2}(Å)	7.800	7.950	8.500	8.500
x_0(eVÅ^{-m})	0.123554	0.235139	0.346813	0.362085
x_1(eVÅ^{-m-1})	-0.134361	-0.247471	-0.350701	-0.378121
x_2(eVÅ^{-m-2})	0.0543818	0.0983304	0.133662	0.149113
x_3(10^{-2}eVÅ^{-m-3})	-0.981194	-1.748544	-2.273741	-2.610984
x_4(10^{-3}eVÅ^{-m-4})	0.675816	1.174278	1.456262	1.706176
α(10^{-4}eV^{2}Å^{-n})	0.656618	0.805877	1.011750	2.678379
β	1.836569	2.951121	5.580155	4.354578
r_0(Å)	2.552655	2.892067	2.884996	2.771859

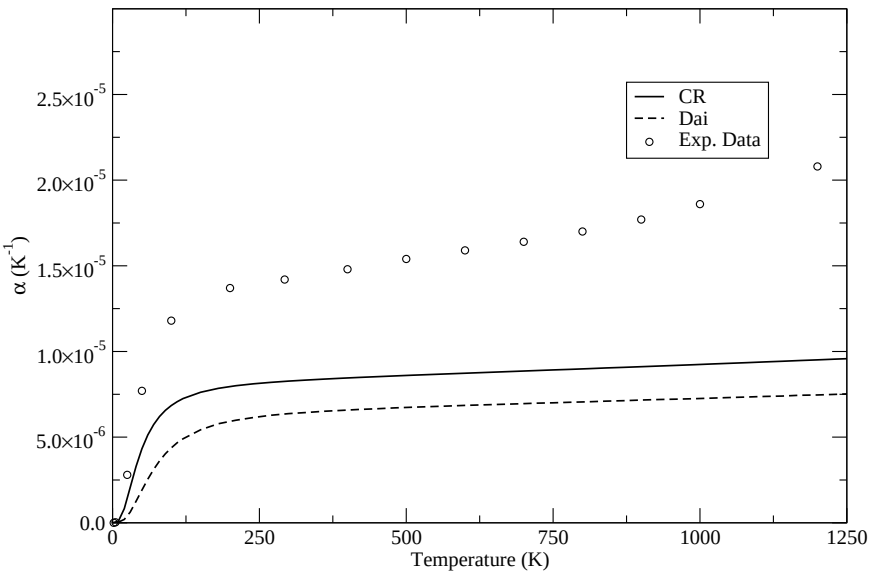

Figure 5.17: Thermal expansion coefficient for Au as calculated using the Cleri-Rosato and Dai *et al.* potentials. Experimental data taken from [9].

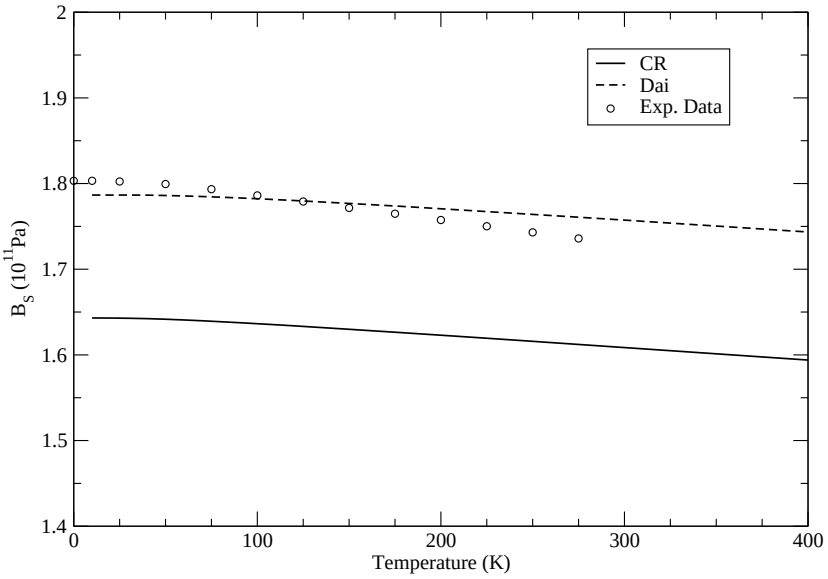

Figure 5.18: Adiabatic bulk modulus for Au as calculated using the Cleri-Rosato and Dai *et al.* potentials. Experimental data taken from [15].

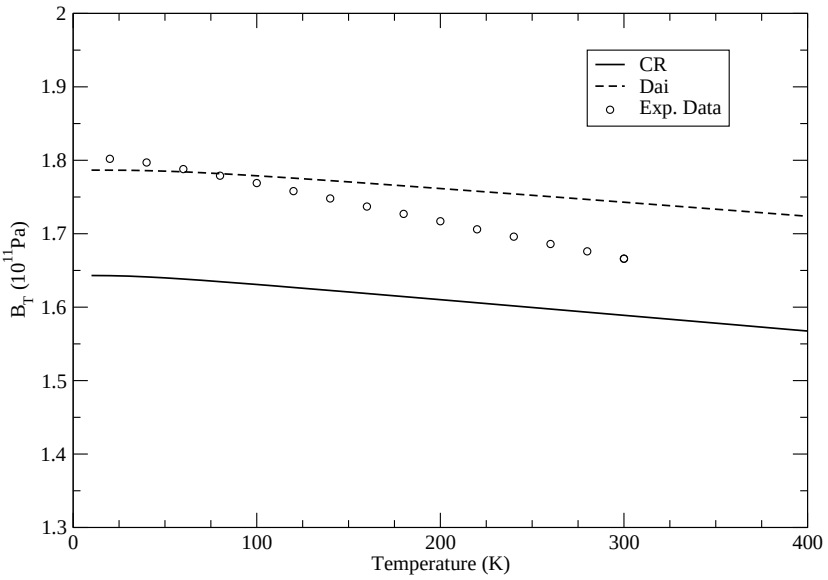

Figure 5.19: Isothermal bulk modulus for Au as calculated using the Cleri-Rosato and Dai *et al.* potentials. Experimental data taken from [11] and [12].

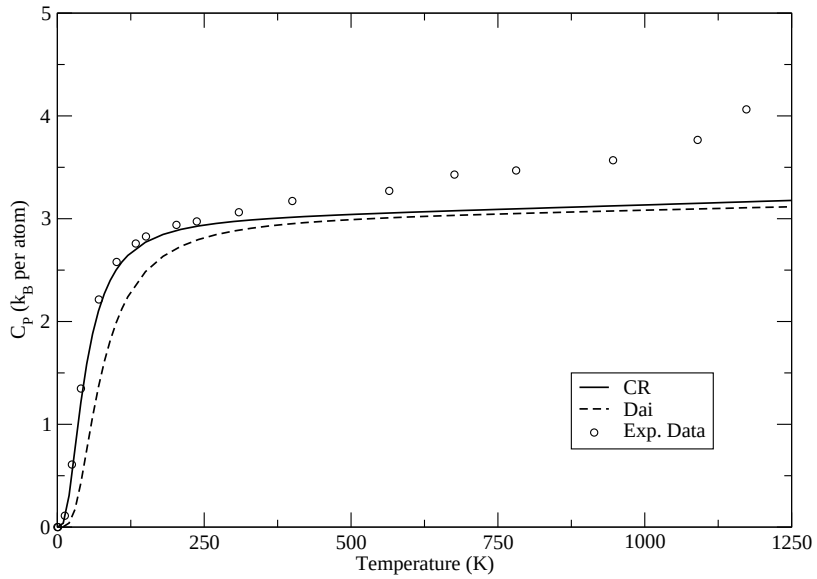

Figure 5.20: Specific heat at constant pressure for Au as calculated using the Cleri-Rosato and Dai *et al.* potentials. Experimental data taken from [13].

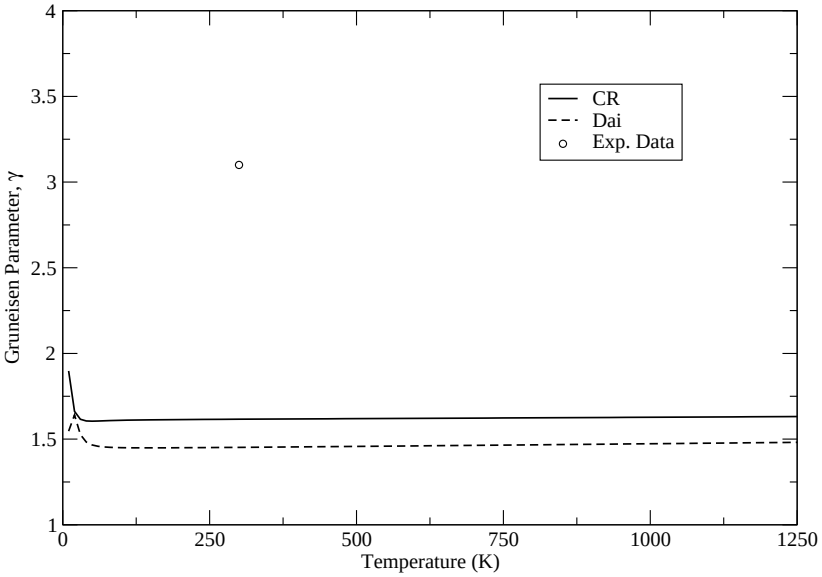

Figure 5.21: Grüneisen parameter for Au as calculated using the Cleri-Rosato and Dai *et al.* potentials. Experimental data taken from [16].

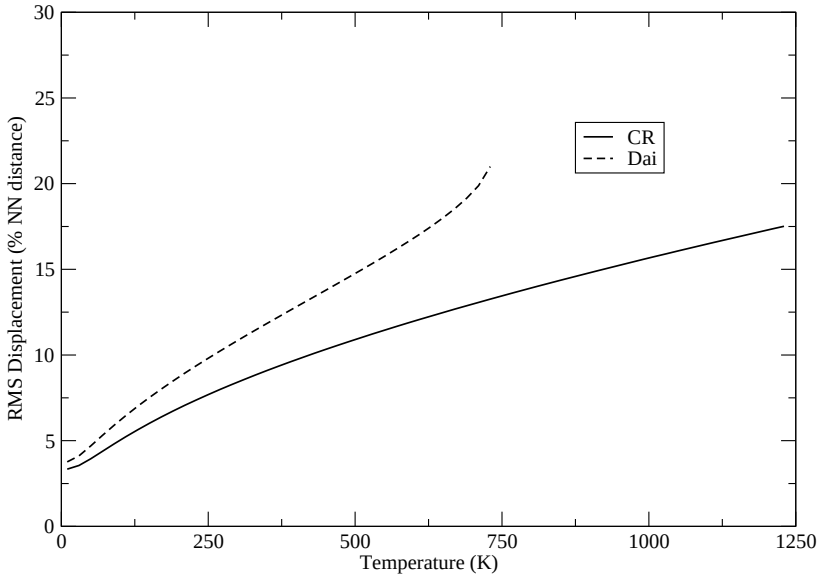

Figure 5.22: Atomic root-mean-square displacement for Au as calculated using the Cleri-Rosato and Dai *et al.* potentials.

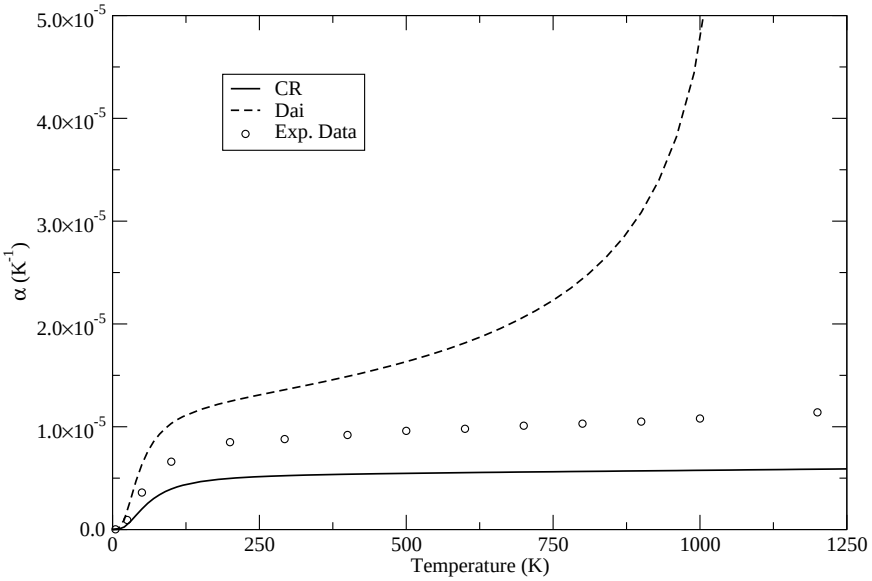

Figure 5.23: Thermal expansion coefficient for Pt as calculated using the Cleri-Rosato and Dai *et al.* potentials. Experimental data taken from [9].

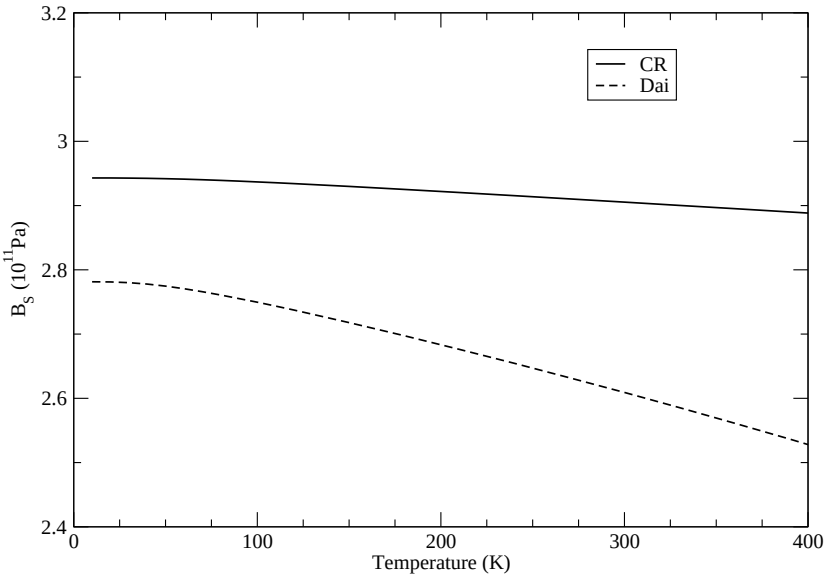

Figure 5.24: Adiabatic bulk modulus for Pt as calculated using the Cleri-Rosato and Dai *et al.* potentials. Experimental data taken from [15].

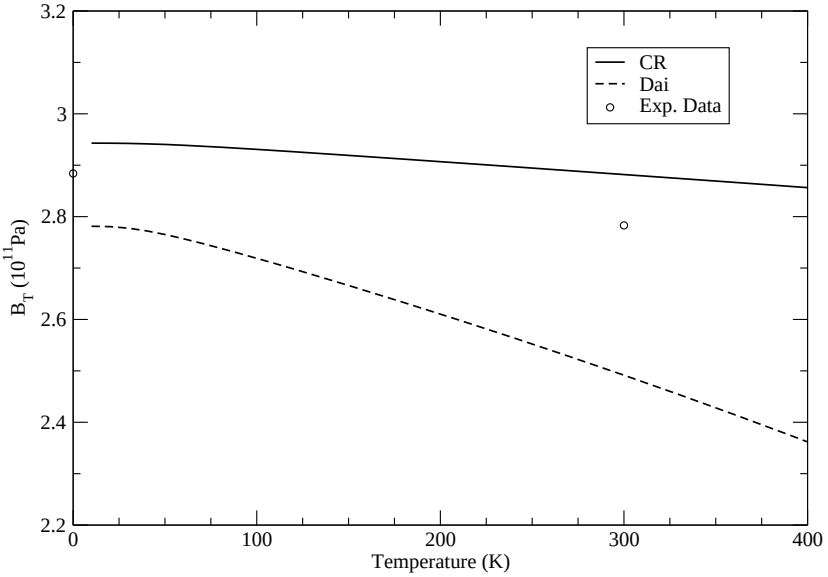

Figure 5.25: Isothermal bulk modulus for Pt as calculated using the Cleri-Rosato and Dai *et al.* potentials. Experimental data taken from [11] and [12].

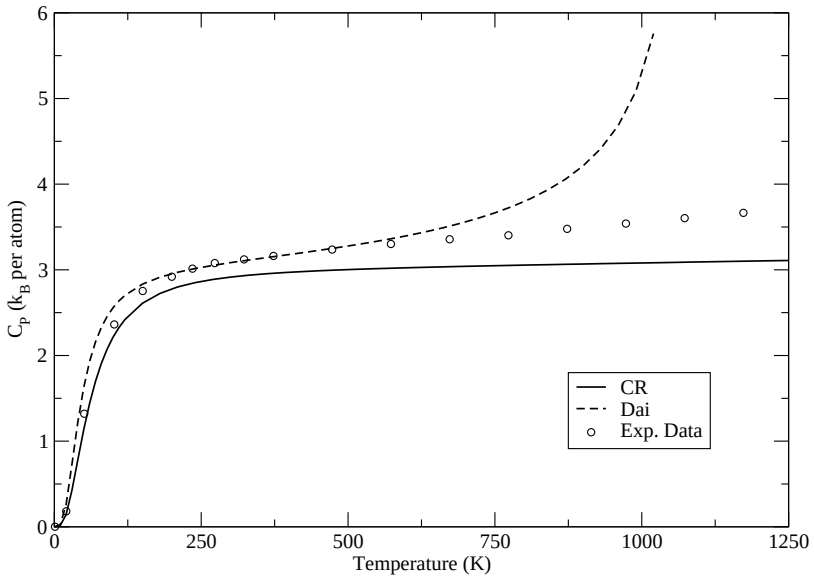

Figure 5.26: Specific heat at constant pressure for Pt as calculated using the Cleri-Rosato and Dai *et al.* potentials. Experimental data taken from [13].

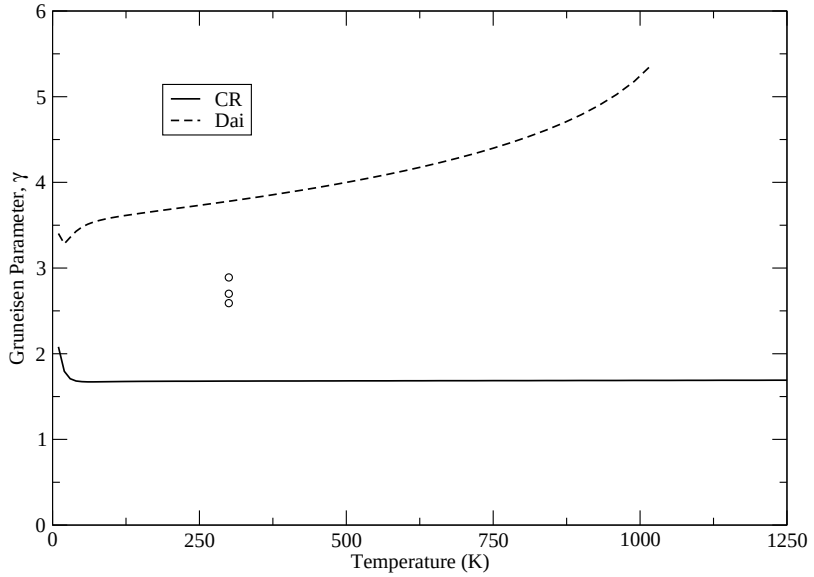

Figure 5.27: Grüneisen parameter for Pt as calculated using the Cleri-Rosato and Dai *et al.* potentials. Experimental data taken from [16].

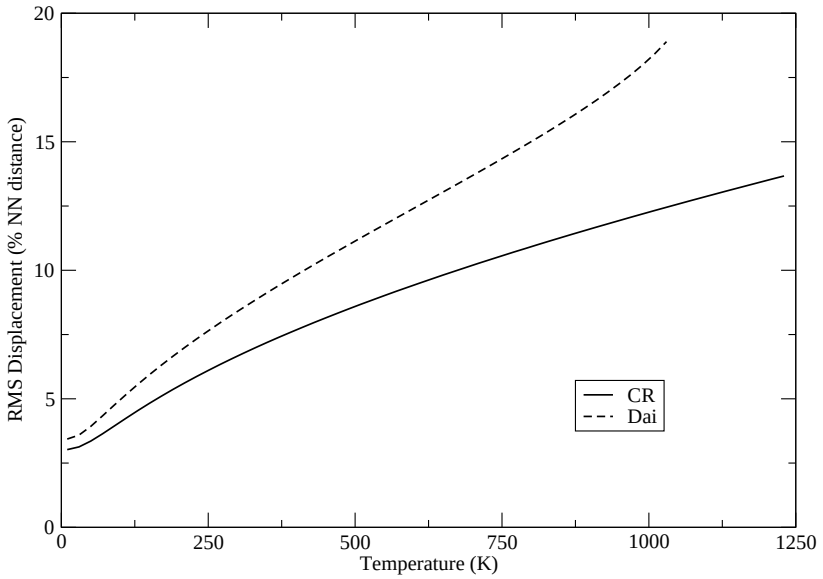

Figure 5.28: Atomic root-mean-square displacement for Pt as calculated using the Cleri-Rosato and Dai *et al.* potentials.

Chapter 6

Discussion and Conclusions

The analytic embedding function of Sutton and Chen [18] and its modified counterpart [5] were applied to to calculate the phonon dispersion curves and other thermodynamic properties of the FCC metals Cu, Ag, Au and Pt. Also studied was a modified version of the potential where the density function was chosen to have an exponential form rather than power-law. Selecting this form of the density was motivated in part by the results of Dai *et al.* [29] and Cleri & Rosato [28] who both used an exponential form for their potentials. Also discussed was the fact that the charge density as a function of distance, as calculated using Density Functional Theory and Hartree-Fock methods, is better described by an exponential decay than a power-law function. As is seen in the results for various thermodynamic properties, this form of potential performs quite well. The repulsive part of the potential was left unchanged (though the exponent was re-fit) in an attempt to show that the instability of the potential at higher temperature is due to this slower decay of the charge density. The modified Sutton-Chen potential was fit to cohesive energy, lattice parameter, bulk modulus and elastic constants at room temperature.

The results for thermal expansion are overestimated for every metal considered here, regardless of which specific Sutton-Chen–type potential was used. Most results

do improve, however, when moving from the original Sutton-Chen form to the quantum corrected one for all metals except Ag. Further improvement is seen with the modified Sutton-Chen potential in nearly all cases. Results for the Cleri-Rosato potential are overall quite good, though for Au the thermal expansion is 41% too low at 300K. Both the adiabatic and isothermal bulk moduli are also underestimated for Au by 5% and 7% at 300K, respectively. The Dai *et al.* potential fares better here, being 2% too large for the adiabatic case and 5% for the isothermal. Results for the thermal expansion coefficient are relatively poor, being underestimated by 60% at 300K. For the remaining elements the results are much improved which once again highlights the difficulty in accurately reproducing the thermodynamic properties of Au. A modified version of the EAM, named the MAEAM (Modified Analytic Embedded Atom Method), shows promising results for Cu, Ag and Au. It was introduced by Xie *et al.* [51] and shows good results for phonon dispersion curves in the symmetry directions for the noble metals. Essentially, this potential includes a term accounting for the non-spherical distribution of electrons and nonlinear superposition of electron charge densities.

Cases where only pure pair-potentials were used offered some insight into the effect of different fitting schemes. The Erkoç potential very accurately predicted the thermal expansion coefficient and isobaric heat capacity of Cu, Ag and Au. Results for bulk properties were quite poor, however. This is likely due to the fact that this potential was not fit to bulk properties at all and was instead first fit to the potential curve of a dimer. After this the two terms of the potential were scaled by coefficients so that the equilibrium lattice parameter and cohesive energy were correctly reproduced. Further testing was done by examining the behavior of this potential with regards to stability in three to seven atom micro-clusters. The Morse potential was fit to bulk properties and thus predicts them quite well. Phonon spectra, heat capacity and thermal expansion were not well predicted, however.

Based on the results in this work, one can conclude that an exponential function better describes the charge density decay in (at least) the metals considered here. The modification to the Sutton-Chen potential yielded consistent improvement over the SC and QSC potentials in nearly every thermodynamic calculation. The only exceptions are the phonon spectra where the MSC was not universally better than the QSC. It is possible that changing the exponent of the repulsive term in the potential may partially account for the improved results. However, the QSC is essentially a re-parametrized version of the SC potential already. This provides insight into the sort of improvement that can be expected simply by changing the parameters. The MSC provides significant improvement over even this re-parametrized potential, suggesting that the improvement is largely due to the change in the density function and not simply due to a change in parameters. A good example of this is Ag where the QSC results were further from experiment than those of the SC. The MSC showed improvement over both of those.

Further improvement is likely to be gained if the repulsive contribution to the potential is also changed to an exponential function. This could be a topic for further study. Another possibility would be to include higher moments than the second in the density of states. This would of course change $F(\rho)$ completely but may yield improved results.

Bibliography

[1] Erkoç, S. *Annual Review of Computational Physics*. World Scientific, Singapore, (2001).

[2] Doyama, M. and Cotterill, R. M. J. *Energies & Atomic Configurations of Line Defects and Plane Defects in FCC Metals*. Gordon and Breach, New York, (1966).

[3] Erkoç, S. *Zeitschrift fr Physik D Atoms, Molecules and Clusters* **32**(3), 257–260 (1994).

[4] Finnis, M. W. and Sinclair, J. E. *Philosophical Magazine A* **50**(1), 45–55 (1984).

[5] Kimura, Y., Qi, Y., Çağin, T., and Goddard III, W. A. Technical report, Caltech ASCI, (1998).

[6] Svensson, E. C., Brockhouse, B. N., and Rowe, J. M. *Phys. Rev.* **155**, 619–632 (1967).

[7] Kamitakahara, W. A. and Brockhouse, B. N. *Physics Letters A* **155**, 639–640 (1969).

[8] Lynn, J. W., Smith, H. G., and Nicklow, R. M. *Phys. Rev. B* **8**, 3493–3499 (1973).

[9] Touloukian, Y. S., Kirby, R. K., Taylor, R. E., and Desai, P. D. *Thermophysical Properties of Matter - The TPRC Data Series. Volume 12. Thermal Expansion Metallic Elements and Alloys.* Plenum Data Company, New York, (1977).

[10] Overton, W. C. and Gaffney, J. *Phys. Rev.* **98**, 969–977 (1955).

[11] Wallace, D. C. *Thermodynamics of Crystals.* John Wiley and Sons, Inc., (1972).

[12] Kittel, C. *Introduction to Solid State Physics.* John Wiley and Sons, Inc., (1996).

[13] Touloukian, Y. S. and Buyco, E. H. *Thermophysical Properties of Matter - The TPRC Data Series. Volume 4. Specific Heat - Metallic Elements and Alloys.* Plenum Data Company, New York, (1970).

[14] MacDonald, R. A. and MacDonald, W. M. *Physical Review B* **15**, 1715–1724 (1981).

[15] Neighbours, J. R. and Alers, G. A. *Phys. Rev.* **111**, 707–712 (1958).

[16] Pandya, C. V., Vyas, P. R., Pandya, T. C., and Gohel, V. B. *Bulletin of Materials Science* **25**, 63–67 (2002).

[17] Savrasov, S. and Andersen, O. From Atomic Charge Density Data Bank, (2000). Max-Planck Institute for Solid State Research, Stuttgart, Germany.

[18] Sutton, A. P. and Chen, J. *Philosophical Magazine Letters* **61**(3), 139–146 (1990).

[19] Liem, S. Y. and Chan, K.-Y. *Surface Science* **328**, 119–128 (1995).

[20] Kimura, Y., Qi, Y., Çağin, T., and Goddard III, W. A. Technical report, Caltech ASCI, (1998).

[21] Kimura, Y., Qi, Y., Çağin, T., and Goddard III, W. A. *Physical Review B* **59**, 3527–3533 (1999).

[22] Caixing, Z., Rangsu, L., Qunyi, Z., Ze'an, T., Xin, W., and Qiang, L. *Ser. G Physics, Mechanics & Astronomy* **48**, 687–694 (2005).

[23] Akbarzadeh, H., Abroshan, H., and Parsafar, G. A. *Solid State Communications* **150**, 254–257 (2010).

[24] Ryu, S., Weinberger, C. R., Baskes, M. I., and Cai, W. *Modelling Simul. Mater. Sci. Eng.* **17**, 075008 (2009).

[25] Jelinek, B., Groh, S., Horstemeyer, M. F., Houze, J., Kim, S. G., Wagner, G. J., Moitra, A., and Baskes, M. I. *Physical Review B* **85**, 245102 (2012).

[26] Lee, B.-J., Ko, W.-S., Kim, H.-K., and Kim, E.-H. *CALPHAD: Computer Coupling of Phase Diagrams and Thermochemistry* **34**, 510–522 (2010).

[27] Clementi, E. and Roetti, C. *Atomic Data and Nuclear Data Tables* **14**, 177 (1974).

[28] Cleri, F. and Rosato, V. *Phys. Rev. B* **48**, 22–33 (1993).

[29] Dai, X. D., Kong, Y., and Li, J. H. *Phys. Rev. B* **75**, 104101 (2007).

[30] Duparc, O. H. *Philosophical Magazine & Philosophical Magazine Letters* **89**, 3117–3131 (2009).

[31] Baskes, M. I. and Melius, C. F. *Physical Review B* **20**, 3197–3204 (1979).

[32] Morse, M. D. *Chemical Reviews* **86**(6), 1049–1109 (1986).

[33] Daw, M. S. and Baskes, M. I. *Phys. Rev. B* **29**, 6443–6453 (1984).

[34] Mei, J., Davenport, J. W., and Fernando, G. W. *Phys. Rev. B* **43**, 4653–4658 (1991).

[35] Sutton, A. P. *Electronic Structure of Materials*. Oxford Science Publications, (1993).

[36] Baskes, M. I. *Phys. Rev. Lett.* **59**, 2666–2669 (1987).

[37] Bullett, D. W., Haydock, R., Heine, V., and Kelly, M. J. *Solid State Physics: Advances in Research and Applications Vol. 35*. Academic Press, (1980).

[38] Pettifor, D. *Bonding and Structure of Molecules and Solids*. Oxford Science Publications, (1995).

[39] Born, M. and Huang, K. *Dynamical Theory of Crystal Lattices*. Oxford University Press, (1968).

[40] Maradudin, A. A., Montroll, E. W., and Weiss, G. H. *Theory of Lattice Dynamics in the Harmonic Approximation. Solid State Physics Supplement 3*. Academic Press, (1963).

[41] Maradudin, A. A. *Theory of Lattice Dynamics in the Harmonic Approximation*. Academic Press, (1971).

[42] Squires, G. L. *Arkiv för Fysik* **25**, 21–32 (1962).

[43] Schwabl, F. *Statistical Mechanics*. Springer-Verlag, (2002).

[44] Bian, Q. Master's thesis, Brock University, (2005).

[45] Lindemann, F. *Physik. Z.* **11**, 609–612 (1910).

[46] Çağin, T., Dereli, G., Uludoğan, M., and Tomak, M. *Phys. Rev. B* **59**, 3468–3473 (1999).

[47] Levenberg, K. *Quarterly of Applied Mathematics* **2**, 164–168 (1944).

[48] Phuong, L. D., Pasturel, A., and Manh, N. *Journal Physics: Condensed Matter* **5**, 1901–1918 (1993).

[49] Barker, J. A., Klein, M. L., and Bobetic, M. V. *Physical Review B* **2**, 4176–4179 (1970).

[50] Sinha, S. K. *Physical Review* **143**, 422–433 (1966).

[51] Xie, Y., Zhang, J.-M., and Ji, V. *Solid State Communications* **145**, 182–185 (2008).